



Petrology, Rock Magnetism and Stratigraphy of Late Quaternary Ice-rafted Detritus at the Southeast Grand Banks Slope of Newfoundland, Atlantic Canada

Dissertation for the Doctoral Degree in Natural Sciences

Dr. rer. nat.

at the Faculty of Geosciences
of the University of Bremen

submitted by

Shettima Bukar

Bremen, May 2024



PRÜFUNGSAUSSCHUSS

First Reviewer: Prof. Dr. Tilo von Dobeneck
Faculty of Geoscience
University of Bremen

Second Reviewer: Prof. Dr. Mark Dekkers
Department of Earth Science
University of Utrecht

**Promotionkolloquium Datum:
11 June 2024**

Declarations

Name / Name: Shettima Bukar Datum / Date: 14.5.2024

Anschrift / Address: [REDACTED]

**Erklärung gem. § 4 Abs. 1 Nr. 3 und 4
der Promotionsordnung vom 18.06.2018**

***Statement according to § 4 (1) no. 3 and 4
of the Doctoral Degree Rules and Regulations of 18.06.2018***

Ich erkläre, dass ich mich weder einem Promotionsverfahren unterzogen noch ein solches beantragt habe.

I affirm that I did not undergo a doctoral degree granting procedure, nor did I apply for the examination procedure elsewhere.

Mit einer Überprüfung der Dissertation mit qualifizierter Software zur Untersuchung von Plagiatsvorwürfen bin ich einverstanden. /

I accept scanning of the doctoral thesis with appropriate software for the detection of plagiarism.



(Unterschrift Doktorand/in / Signature PhD student)

Versicherung an Eides Statt / Affirmation in lieu of an oath

gem. § 5 Abs. 5 der Promotionsordnung vom 28.04.2021 /
according to § 5 (5), Doctoral Degree Rules and Regulations of 28 April, 2021

Ich / I,

Shettima Bukar, Luisental 29D, 28359 Bremen, Student ID: 3217508

Vorname / First Name, Name / Name, Anschrift / Address, Matr.-Nr. / student ID no.

versichere an Eides Statt durch meine Unterschrift, dass ich die vorliegende Dissertation selbständig und ohne fremde Hilfe angefertigt und alle Stellen, die ich wörtlich dem Sinne nach aus Veröffentlichungen entnommen habe, als solche kenntlich gemacht habe, mich auch keiner anderen als der angegebenen Literatur oder sonstiger Hilfsmittel bedient habe und die zu Prüfungszwecken beigelegte elektronische Version (PDF) der Dissertation mit der abgegebenen gedruckten Version identisch ist. / *With my signature I affirm in lieu of an oath that I prepared the submitted dissertation independently and without illicit assistance from third parties, that I appropriately referenced any text or content from other sources, that I used only literature and resources listed in the dissertation, and that the electronic (PDF) and printed versions of the dissertation are identical.*

Ich versichere an Eides Statt, dass ich die vorgenannten Angaben nach bestem Wissen und Gewissen gemacht habe und dass die Angaben der Wahrheit entsprechen und ich nichts verschwiegen habe. / *I affirm in lieu of an oath that the information provided herein to the best of my knowledge is true and complete.*

Die Strafbarkeit einer falschen eidesstattlichen Versicherung ist mir bekannt, namentlich die Strafandrohung gemäß § 156 StGB bis zu drei Jahren Freiheitsstrafe oder Geldstrafe bei vorsätzlicher Begehung der Tat bzw. gemäß § 161 Abs. 1 StGB bis zu einem Jahr Freiheitsstrafe oder Geldstrafe bei fahrlässiger Begehung. / *I am aware that a false affidavit is a criminal offence which is punishable by law in accordance with § 156 of the German Criminal Code (StGB) with up to three years imprisonment or a fine in case of intention, or in accordance with § 161 (1) of the German Criminal Code with up to one year imprisonment or a fine in case of negligence.*

Bremen, 14.5.2024

Ort / Place, Datum / Date



Unterschrift / Signature

Contents

DECLARATIONS	III
CONTENTS	V
SUMMARY	VII
ZUSAMMENFASSUNG	IX
CHAPTER 1: INTRODUCTION	1
1.1 HEINRICH EVENTS AND HEINRICH EVENT LAYERS IN THE NORTH ATLANTIC OCEAN	1
1.2 ICE-RAFTED DETRITUS - GRAIN SIZES, OCCURRENCE, AND DISTRIBUTION AROUND THE EASTERN CANADIAN MARGIN	3
1.3 SCIENTIFIC OBJECTIVES	4
1.4 GEOLOGICAL SETTINGS	4
1.4.1 <i>Tectonics and Geology of the Grand Banks</i>	4
1.4.2 <i>IRD Provenance</i>	5
1.4.3 <i>Dynamics of the Laurentide Ice Sheet</i>	7
1.5 THESIS OUTLINE	7
1.6 REFERENCES	9
CHAPTER 2: ICE-RAFTED DETRITUS (IRD) OF THE SE GRAND BANKS SLOPE, NEWFOUNDLAND, THROUGHOUT HEINRICH LAYERS 1 TO 6 - PART I: PETROLOGY AND ABUNDANCE	13
2.1 INTRODUCTION	14
2.2 GEOLOGICAL SETTING	16
2.2.1 <i>IRD Provenance and Source to Sink Transport</i>	16
2.2.2 <i>South East Grand Banks Slope Settings</i>	16
2.3 MATERIALS AND METHODS	17
2.3.1 <i>Materials</i>	17
2.3.2 <i>Methods</i>	18
2.3.2.1 Shipboard Core Logging	18
2.3.2.2 Sieve Analysis	18
2.3.2.3 Petrological Characterization and Counting of IRD particles	18
2.3.2.4 Digital Microscopy of Selected IRD particles	18
2.3.2.5 Polarized Light Microscopy of IRD Thin Sections	19
2.3.2.6 Oxygen Isotope Stratigraphy	19
2.3.2.7 X-ray Fluorescence Half Core Scanning	19
2.4 LITHO- AND CHRONOSTRATIGRAPHY	20
2.5 IRD PETROLOGY AND ABUNDANCE	21
2.5.1 <i>Igneous Lithologies</i>	23
2.5.1.1 Muscovite-Biotite Granite	23
2.5.1.2 Hornblende Granite	24
2.5.1.3 Biotite Granite	24
2.5.1.4 Garnet Gabbro	24
2.5.1.5 Quartz	26
2.5.1.6 Microcline	26
2.5.1.7 Tonalite	26
2.5.1.8 Dolerite	27
2.5.1.9 Olivine-Basalt	28
2.5.1.10 Scoria	28
2.5.1.11 Obsidian	28
2.5.2 <i>Sedimentary and Metamorphic Lithologies</i>	28
2.5.2.1 Ooid-bearing Dolomite	29
2.5.2.2 Sucrosic Dolomite	30
2.5.2.3 Calcite	30
2.5.2.4 Mudstone	30
2.5.2.5 Quartz Wacke	30

2.5.2.6	Greywacke	31
2.5.2.7	Hematite-coated Quartz	32
2.5.2.8	Shale	32
2.5.2.9	Shocked Quartz	32
2.5.2.10	Biotite Schist	32
2.5.2.11	Amphibolite	32
2.6	STATISTICAL AND STRATIGRAPHIC ANALYSES OF IRD COMPOSITION AND ACCUMULATION	33
2.6.1	<i>Proportions and Accumulation of IRD Lithologies in HL and IL Units</i>	33
2.6.2	<i>Major Factors and Trends of Variance in IRD Lithology</i>	36
2.6.3	<i>Stratigraphic Succession and Deposition Rate of IRD Lithologies</i>	38
2.6.4	<i>Implications for Heinrich Event Chronology</i>	38
2.7	CONCLUSIONS.....	39
2.8	ACKNOWLEDGEMENTS.....	41
2.9	REFERENCES	41
CHAPTER 3: ICE-RAFTED DETRITUS (IRD) OF THE SE GRAND BANKS SLOPE, NEWFOUNDLAND, THROUGHOUT HEINRICH LAYERS 1 TO 6 - PART II: MAGNETIC PROPERTIES		
45		
3.1	INTRODUCTION	46
3.2	MATERIALS AND METHODS	48
3.2.1	<i>Materials</i>	48
3.2.2	<i>Methods</i>	48
3.2.2.1	Magnetic Susceptibility	48
3.2.2.2	Remanent Magnetization	49
3.3	MAGNETIC, GEOCHEMICAL AND SEDIMENTOLOGICAL BULK SEDIMENT PROPERTIES.....	49
3.3.1	<i>Rock Magnetic Bulk Sediment Records</i>	49
3.3.2	<i>Geochemical Bulk Sediment Records</i>	52
3.3.3	<i>Sedimentological Bulk Sediment Records</i>	55
3.4	MAGNETIC PROPERTIES OF CLASSIFIED IRD LITHOLOGIES	57
3.4.1	<i>Magnetic Susceptibility and Remanence-based Rock-Magnetic Properties</i>	58
3.4.2	<i>IRM Acquisition Curve Analyses of Bulk Sediment and Classified IRD</i>	61
3.5	EMPIRICAL AND CONCEPTUAL MS MODELS OF GLACIOMARINE SEDIMENT	65
3.5.1	<i>Grain-Size Dependence of MS and Grain-Size Distribution of IRD</i>	65
3.5.2	<i>Modelling Bulk MS from Sediment Properties and Classified IRD Counts</i>	67
3.6	CONCLUSIONS.....	69
3.7	ACKNOWLEDGEMENTS.....	70
3.8	REFERENCES	71
CHAPTER 4: IMPRINT AND ASSESSMENT OF RANDOM DEPOSITION AND LITHOLOGICAL VARIABILITY OF ICE-RAFTED DEBRIS (IRD) IN MAGNETIC SUSCEPTIBILITY RECORDS.....		
74		
4.1	INTRODUCTION	75
4.2	MATERIALS AND METHODS	76
4.2.1	<i>Materials</i>	76
4.2.2	<i>Methods</i>	77
4.2.2.1	Whole-Core MS Logging	77
4.2.2.2	Split-Core MS Scanning.....	77
4.2.2.3	Discrete Sample MS Measurement	78
4.3	INSTRUMENTAL IMPLICATIONS AND IMPROVEMENTS OF MS DATA ACQUISITION	78
4.3.1	<i>MS Sensor Response Functions</i>	78
4.3.2	<i>Comparison of MS Records by Different Logging Techniques</i>	80
4.3.3	<i>IRD Mapping by Split-Core MS Scanning</i>	82
4.4	CONCLUSIONS.....	85
4.5	ACKNOWLEDGEMENTS.....	85
4.6	REFERENCES	85
CHAPTER 5: SYNTHESIS AND OUTLOOK.....		
87		
ACKNOWLEDGEMENTS		
90		

Summary

The Quaternary sediments of the Atlantic Canada margin usually contain numerous evidences of paleoclimate oscillations. The short-lived, abrupt and episodic surges of sediment-laden armadas of icebergs calved from Laurentide Ice Sheet (LIS) into the North Atlantic Ocean via ice stream conduits has deposited ice-rafted detritus (IRD) all across the northern North Atlantic oceanic basin. Such events have had considerable impact on ocean water circulation system (i.e. Atlantic meridional overturning circulation – AMOC) and deep water formation owing to the huge influx of meltwater delivered by subglacial discharge and iceberg melting. This catastrophic instability of the LIS has resulted in a stratigraphic sequence of detrital-rich Heinrich Layers (HL) during the cold phases of the Late Quaternary period. As IRD fragments are the direct evidence of the interplay between ice sheets and the North Atlantic Ocean, we still lack understanding of their hidden information on ice sheet dynamics, location of ice margins, the provenance and spatial dispersion of distinct terrigenous materials and their petromagnetic properties and contributions of different IRD species to magnetic HL records.

In this PhD thesis, I investigated a sediment core (GeoB 18530-1) acquired at the foot of Southeast Grand Banks Slope of Newfoundland, that represents a continuous Late Pleistocene stratigraphic sequence of Heinrich Event layers 1 - 6 (H1 – H6). Discrete sample sets were taken at a very high resolution of 2 cm for various analyses including digital light microscopy, thin section petrography, X-ray fluorescence, rock magnetics, and grain-size sieving.

In a first step of the thesis project, a total of 8243 coarse-grained (>1 mm) IRD particles were petrologically identified and their lithologies petrographically classified into 22 microscopically distinguishable categories. The abundances of these IRD lithologies were determined by counting individual particles at a high resolution of 2 cm steps throughout the continuous stratigraphic sequence of HLs (H1 – H6). This revealed the temporal and spatial change in the deposition of each IRD lithology. It was found that dolomitic IRD predominates the mid-part of all HLs whilst muscovite-biotite granite was found in greater abundance at the top and bottom of the HLs. Additionally, the statistical investigation of the count records of the 22 IRD lithologies manifested three well-defined groups based on whether their deposition is higher within HLs or interlayers or similar in both. Compositionally, it was found that H1, H2, H4, and H5 are kindred to each other while H3 and H6 are individually distinct.

The second step of the thesis was an advancement of the finding from the initial part where the petrological information that was gleaned is used for magnetic analysis of particularly HLs and individual IRD lithologies. The pronounced magnetic susceptibility signal of HLs is usually intriguing compared to the interlayer units thus, it is momentous to discern the IRD lithology that influences the signal. Though, the >1 mm IRD underrepresents the total amount of IRD where finer grains are much more abundant, a lithology-specific identification can only be conducted using the coarser IRD fractions. From the magnetic properties of the coarse IRD it was found that out of the 22 different lithologies, as many as 16 possess a relatively lower magnetic susceptibility than the background sediment. Only 6 IRD lithologies are typified by a higher susceptibility among which the muscovite-biotite granite is four-fold higher magnetic than the background. With the complementary XRF data it was revealed clearly that the

susceptibility enhancement by the (K/Fe denoted) granite is partly compensated by the (Ca/Sr represented) dolomitic IRD. Therefore, with the muscovite-biotite granite being second in abundance to dolomitic IRD, it mainly controls the pronounced magnetic susceptibility signals of HLs. In modeling magnetic susceptibility based on coarse-grained IRD count data a misfit of the model was observed proposing that IRD sedimentation does not only occur through detritus rain-out from icebergs but rather through other transport processes like advection or gravitational flow, at least for the terminal part of the sediment's trajectory.

Lastly, traditional magnetic susceptibility measurements are obtained in ways, where the inhomogeneity of sediment records is mostly played down. This is because the sensor coils of whole-core magnetic susceptometers average signals over a large volume, thereby integrating the microscale susceptibility distribution over a considerable volume. Split-core susceptibility logs produced with a spot sensor at high resolution average the magnetic signal over a much smaller volume of a material. Using a novel protocol, this spot sensor technique provides the freedom to scan across an entire split core. By logging multiple parallel tracts at a high resolution of 1 cm along and between each tract, the derived contour plot reveals coarse IRD distribution, where the color spectrum denotes lateral variability in magnetic susceptibility.

Zusammenfassung

Die Quartärsedimente vor Kanadas atlantischem Kontinentalrand enthalten zahlreiche Anzeichen für paläoklimatische Schwankungen. Die kurzlebigen, abrupten und episodischen Einträge von sedimentbeladenen Eisberg-Armadas, die vom Laurentide Ice Sheet (LIS) über Eisstromkanäle in den Nordatlantik kalbten, haben im gesamten nördlichen Nordatlantik eistransportierten Detritus (ice rafted detritus - IRD) abgelagert. Solche Ereignisse hatten erhebliche Auswirkungen auf die Ozeanzirkulation, insbesondere die meridionale Umwälzung des Atlantiks (AMOC) und die Tiefenwasserbildung aufgrund des mit ihnen verbundenen enormen Zustroms von Schmelzwasser aus subglazialen Abflüssen und dem Schmelzen von Eisbergen. Die inhärente Instabilität des LIS führte zu einer stratigraphischen Abfolge von detritus-reichen Heinrich-Lagen (HL) während der kalten Phasen des Spätquartärs. Da IRD-Fragmente ein direkter Beweis für das Zusammenspiel zwischen Eisschilden und Nordatlantik sind, fehlt uns noch immer ein Verständnis der in ihnen verborgenen Informationen über die Dynamik der Eisschilde, die Lage der Eisränder, die Herkunft und räumliche Verteilung verschiedener terrigener Materialien und die petromagnetischen Eigenschaften und Beiträge verschiedener IRD-Lithologien zu gesteinsmagnetischen Sedimentkerndaten.

In dieser Dissertation untersuchte ich einen Sedimentkern (GeoB 18530-1) vom Fuße des Südosthangs der Grand Banks von Neufundland, der eine kontinuierliche spätpleistozäne stratigraphische Abfolge der Heinrich-Ereignis-Schichten 1 - 6 (H1 - H6) darstellt. Es wurden Einzelproben in einer sehr hohen Auflösung von 2 cm für verschiedene Analysen entnommen, darunter digitale Lichtmikroskopie, Dünnschliff-Petrographie, Röntgenfluoreszenz, Gesteinsmagnetik und Korngrößensiebung.

In einem ersten Schritt des Promotionsprojekts wurden insgesamt 8243 grobkörnige (>1 mm) IRD-Partikel petrologisch identifiziert und ihre Lithologien petrographisch in 22 mikroskopisch unterscheidbare Kategorien klassifiziert. Die Häufigkeit dieser IRD-Lithologien wurde durch Zählen einzelner Partikel mit der hohen Auflösung von 2 cm-Schritten in der stratigraphischen Abfolge der Heinrichlagen H1 - H6 bestimmt. Dadurch wurden die zeitlichen und räumlichen Veränderungen bei der Ablagerung einzelner IRD-Lithologien sichtbar. Es wurde festgestellt, dass dolomitischer IRD im mittleren Teil aller HL vorherrscht, während Muskovit-Biotit-Granit im oberen und unteren Teil der HL in größerer Menge gefunden wurde. Darüber hinaus ergab die statistische Untersuchung der Zählungen drei klar definierte Gruppen, die darauf beruhen, ob Ablagerung jeder Lithologie innerhalb der HLs oder in den Zwischenschichten höher oder in beiden ähnlich ist. In Bezug auf die Zusammensetzung wurde festgestellt, dass H1, H2, H4 und H5 miteinander verwandt sind, während H3 und H6 individuell verschieden sind.

Der zweite Schritt der Arbeit war eine Weiterentwicklung der Erkenntnisse aus dem ersten Teil, in dem die zuvor gewonnenen petrologischen Informationen für die magnetische Analyse insbesondere von HL und einzelnen IRD-Lithologien verwendet wurden. Das ausgeprägte magnetische Suszeptibilitätssignal von HL im Vergleich zu den dazwischenliegenden Einheiten überrascht, so dass es von Bedeutung ist, die IRD-Lithologien zu erkennen, die dieses Signal vorrangig beeinflussen. Obwohl die IRD >1 mm Fraktion die IRD-Gesamtmenge stark unterrepräsentiert, da feinere Körner viel häufiger vorkommen, kann eine lithologiespezifische

Identifizierung nur anhand der gröberen IRD-Fraktionen erfolgen. Anhand der magnetischen Eigenschaften des groben IRD wurde festgestellt, dass von den 22 verschiedenen Lithologien 16 eine vergleichsweise geringere magnetische Suszeptibilität als das Hintergrundsediment aufweisen. Nur sechs IRD-Lithologien weisen eine höhere Suszeptibilität auf, darunter der Muskovit-Biotit-Granit, der viermal so magnetisch wie der Hintergrund ist. Anhand der ergänzenden XRF-Daten wurde deutlich, dass die Suszeptibilitätserhöhung durch den (durch das K/Fe-Verhältnis quantifizierten) Granit teilweise durch den (mit Ca/Sr quantifizierten) dolomitischen IRD kompensiert wird. Da Muskovit-Biotit-Granit IRD mengenmäßig an zweiter Stelle nach dem dolomitischen IRD steht, scheint er hauptsächlich für das ausgeprägte magnetische Suszeptibilitätssignal der HL verantwortlich zu sein. Bei der Modellierung der magnetischen Suszeptibilität auf Grundlage grobkörniger IRD-Zählraten wurde eine schlechte Anpassung des Modells beobachtet, die darauf hindeutet, dass die IRD-Sedimentation nicht nur durch den Detritus-Regen schmelzender Eisbergen erfolgt, sondern auch durch andere Transportprozesse wie Partikeladvektion oder gravitativen Transport, zumindest auf dem letzten Teil des Sedimenttransportweges.

Herkömmliche magnetische Suszeptibilitätsmessungen werden zumeist auf eine Art und Weise durchgeführt, welche die Inhomogenität der Sedimente heruntergespielt. Das liegt daran, dass die Sensorspulen von Ganzkern-Suszeptometern die Signale über ein großes Kernvolumen integrieren und dabei die mikroskalige Suszeptibilitätsverteilung in beträchtlichem Umfang herausmitteln. Halbkern-Suszeptibilitätsmessungen, die mit einem Punktsensor in hoher Auflösung erstellt werden, mitteln das magnetische Signal über ein viel kleineres Materialvolumen. Mit unserem neuartigen flächenscannenden Messprotokoll bietet diese Punktsensortechnik die Möglichkeit, die gesamte Halbkernoberfläche zu erfassen. Durch die Aufzeichnung mehrerer paralleler Bahnen mit einer hohen Auflösung von 1 cm entlang und zwischen den einzelnen Bahnen zeigt das abgeleitete Konturdiagramm die inhomogene Verteilung grober IRD-Partikel, wobei das Farbspektrum und die daraus abgeleitete horizontale Varianz deutlich die räumliche Streuung der magnetischen Suszeptibilität wiedergeben.

Chapter 1: Introduction

1.1 Heinrich Events and Heinrich Event Layers in the North Atlantic Ocean

The last glacial period (~115 – 11.7 ka) was typified by extreme climatic oscillations that stem from the interplay of various Earth's spheres (e.g. cryosphere, atmosphere, and hydrosphere) under the influence of orbital insolation changes (Ganopolski, 2024). During the last glacial cycle, the mode of climate variability encompasses the development of extensive glacier complexes where the largest of the northern hemisphere was the so-called Laurentide ice sheet (Andrews and Tedesco, 1992; Fulton and Prest, 1987). This ice sheet extended from the eastern margin of the Canadian Cordillera in the west to the Atlantic seafront and continental shelf in the east. Also, it stretched from Queen Elizabeth Island to the mid-western United States at 40°N (Fulton and Prest, 1987). The core of the ice sheet was centered over the oceanic basins of Foxe and Hudson Bay and connected to the North Atlantic Ocean via the geomorphological structural trough of Hudson Strait (Bond et al., 1992).

For reason(s) that are still elusive and debated within the scientific community, the Laurentide ice sheet was periodically unstable and marked by striking phases of short-lived subglacial meltwater discharge and iceberg surges (Bond et al., 1992; Heinrich, 1988; Leng et al., 2019; MacAyeal, 1993; Max et al., 2022). The episodic and abrupt surge of sediment-laden armadas of icebergs from the Laurentide into the North Atlantic Ocean via ice stream conduits is commonly referred to as the Heinrich Event (HE; (Broecker et al., 1992); Bond et al., 1992; Grousset et al., 1993; Heinrich, 1988). The disgorged icebergs were then carried and drifted by ocean currents, eventually thawing in contact with warmer surface water and releasing the entrained sediments (ice-rated detritus – IRD) to the ocean floor (Ruddiman, 1977). These HEs formed sharp and mostly narrow glaciomarine sediment bands, so-called Heinrich Event layers (HLs), which were intercalated by background sedimentation during quiescence phases (Bond et al., 1992; Heinrich, 1988; Meyer et al., 2019). HLs are mainly rich in lithic, predominantly dolomitic IRD fragments, usually have higher magnetic susceptibility values, and are bereft or low in the concentration of planktonic foraminifera with the predominance of the *Neoglobobulimina paucicostata* species (Bond et al., 1992; Grousset et al., 1993; Heinrich, 1988).

As reported by (Ruddiman, 1977), the deposition of IRD in the last glacial-interglacial cycle about 75,000 B.P. shifted significantly because, before the foregoing period, the deposition was mainly near Greenland and Newfoundland, lasting about 50,000 years. The drift in the sedimentation was to the zonal axis along 46° to 50°N where it remained unchanged for about 65,000 yrs reflecting icebergs transecting the region throughout the Wisconsin glaciation. The North Atlantic region where HLs are concentrated is called the “Ruddiman Belt” (Figure 1, Grousset et al., 1993; Ruddiman, 1977). Between the last two major glaciations, i.e. Marine Isotope Stages MIS 4 and MIS 2, six distinct HLs (hereafter denoted as H1 – H6) were deposited across the North Atlantic Ocean (Grousset et al., 1993). Their pattern of deposition differed such that H1, H2, H4, and H5 were distributed along the northern boundary of the Glacial Polar Front between ~46° to 50°N. At the same time, H3 was confined to the central and eastern regions of the North Atlantic (Grousset et al., 1993). The thickness of HLs tapers from 40 – 70 cm in the Labrador Sea over <5 cm in the open central North Atlantic to <1 cm in the east, and

can be traced for more than 3,000 Km in the North Atlantic Ocean (Dowdeswell et al., 1999, 1995). Stratigraphically, HLs proximal to Hudson Strait manifest a more complete and complex history with imprints of other depositional processes besides ice-rafting (Hesse, 2016; Rashid et al., 2012). The complexity of the facies and other related sedimentary features of the HL deposits owes to the subglacial meltwater discharge that triggers the transport of finer materials through nepheloid flows and turbidity currents (Hesse and Khodabakhsh, 2016; Rashid et al., 2012). These depositional processes also deliver detritus into the deep sea, thus forming various types of deposits within the Labrador Sea (Hesse, 2016).

The distal HL deposits in the open North Atlantic Ocean are principally composed of a high ratio of IRD to planktonic foraminifera (Heinrich, 1988). They are considered individual event layers correlating to a sequence that forms the proximal HLs (Rashid et al., 2003). However, some detailed investigations proved it to be otherwise, for instance, the IRD-rich layers found in the Iberian Margin displayed dual distinct peaks denoting IRD abundance within the Heinrich Event 1 (i.e. H1a and H1b) though only the older HL (H1b) is rich in detrital carbonate.

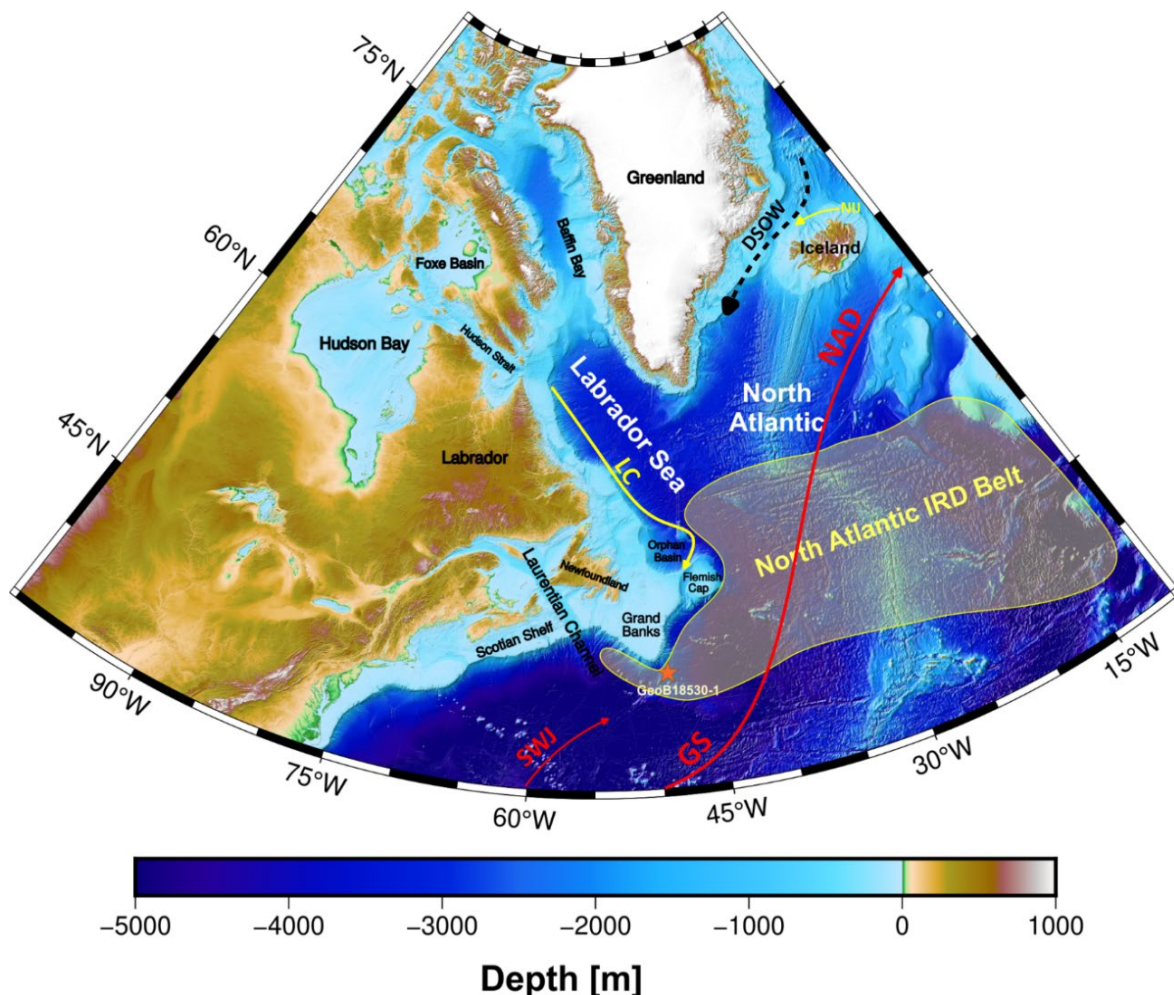


Figure 1: Map of the study area showing the IRD distribution belt and bathymetry alongside the core GeoB18530-1 location (red star). The colored arrows denote ocean currents circulation during Last Glacial Maximum as reported by (Gil and Keigwin, 2018). The dashed black lines represent bottom current due to overflow from Denmark Strait overflow (DSOW), and the yellow lines indicate cold currents that include Labrador (LC) and North Iceland Jet (NIJ). The warmer and temperate currents are indicated with red arrows as Slope Water Jet (SWJ), the Gulf Stream (GS) and North Atlantic Drift (NAD).

Likewise, the work of Hodell et al. (2017) revealed two distinct HLs (H1.1 and H1.2) rich in detrital carbonate and attributed these to separate iceberg discharges from the Laurentide ice sheet. The correlation of detrital carbonate layers found in the northwestern Labrador Sea to HLs obtained in the open North Atlantic showcased that they are both coeval and associated (Andrews and Tedesco, 1992).

In the past few decades, many studies related to the North Atlantic Ocean and its interactivity with circumjacent ice sheet dynamics during the last glacial-deglacial period (Broecker et al., 1992; Heinrich, 1988; Hemming, 2004) have used terms like Heinrich Event (HE), Heinrich Layer (HL) and ice-rafted detritus or ice-rafted debris (IRD) in differently or interchangeably. Here, in this thesis, I embrace strict and consistent usage throughout as proposed by Hodell et al. (2017), and are explained as follows. Heinrich Event (HE) is the episodic massive release of icebergs from the Laurentide ice sheet into the North Atlantic. Heinrich layer (HL) is the sedimentary bed record found in the Quaternary sediment of the North Atlantic. Ice-rafted detritus (IRD) is the entrained sediment in floating icebergs released from ice sheets during Heinrich Events that settled on the ocean floor when the enveloping iceberg thawed.

1.2 Ice-rafted Detritus - Grain Sizes, Occurrence, and Distribution around the Eastern Canadian Margin

Generally, the distribution of IRD in Late Quaternary sediments of the North Atlantic Ocean within the IRD belt was ubiquitous and continuous; it occurred not only during the HLs but also in the interlayers (ILs) of the quiescence regimes between them (Bond and Lotti, 1995a). IRD particles are of varied and discrete grain sizes that range from very fine silt to dropstones (Hemming, 2004), where the finer grain sizes overlap with those of sediments deposited through different processes, e.g. nepheloid deposits. Very coarse IRD from coarse sand to dropstone size is the most appealing and easy to quantify (Andrews, 2000; Cofaigh, 2013). In choosing appropriate IRD grain-size intervals for investigation there exist three complications. Firstly, the well-defined coarse fraction of IRD is relatively small in abundance compared to the finer portions. Secondly, the provenance or parental sources of IRD eroded by glaciers play a major role in grain-size distribution; hence, for the characterization of IRD petrology different grain sizes must be considered. Thirdly, the travel distance of IRD during the sinking processes controls the ultimate grain sizes of IRD (Hemming, 2004).

IRD particles are recognized within three distinct sedimentary facies at the Scotian and Grand Banks margins: (a) detrital carbonate-rich HLs from bedrocks of the Hudson Bay area, which are distributed extensively within the North Atlantic where its thickest beds are found in the Labrador Sea (Andrews and Tedesco, 1992; Bond and Lotti, 1995b; Piper and DeWolfe, 2003; Rashid and Grosjean, 2006), (b) brick-red sandy mud layers deposited by subglacial meltwater discharge from the Gulf of St. Lawrence (Leng et al., 2019, 2018; Piper and Skene, 1998), and (c) Wisconsinan beds punctuated with sparse distribution of IRD particles perhaps owing to their origin to the north of Labrador Sea or from localized ice sheet calving margins (Piper and DeWolfe, 2003). IRD fragments contained in the Late Quaternary sediments of the North Atlantic are generally composed of diverse lithologies that stem from the complex bedrock

geology of the area covered by the ice sheet. The lithologies encompass different rock types and rock-forming minerals that bear imprints of weathering to various degrees.

The pattern and the rate of IRD deposition within a marine setting are contingent on the distribution of the entrained terrigenous materials within the iceberg matrix. Generally, the materials are clumped at the base of the icebergs forming a layer that is about 1 to 3 m thick (Andrews, 2000). Furthermore, the dispersion of IRD particles in ice matrices is greatly governed by the basal thermal condition of the ice sheets (Alley and MacAyeal, 1994). The ultimate deposition of the IRD is inherently random owing to the varying iceberg transport pathways and the differences in the icebergs' sediment load and grain-size distribution (Andrews, 2000). Thus, the choice for specific IRD grain sizes and the stochastic distribution within a stratigraphic column plays a significant role in the quantification of IRD concentration.

1.3 Scientific Objectives

This PhD project investigates the sediment core GeoB18530-1 acquired in 1888 m depth at the southeastern section of Grand Banks Slope, Newfoundland. The area was anomalously unglaciated during the cyclic expansion and contraction of the Laurentide ice sheet. Largely, my investigation will be centered on the lower section of the core that encapsulates all the last glacial Heinrich Event layers (H1 – H6) using techniques that include core logging, wet sediment sieving, digital microscopy, petrography, x-ray fluorescence, and rock magnetics.

Three main chapters, all written as self-supporting journal manuscripts, address the following scientific questions:

- How can the micro-optically highly varied IRD particles be petrologically classified? Does the deposition of different IRD lithologies adapt to a systematic fashion or trend in the HLs? Which of the IRD lithologies show preferred deposition in HLs or in ILs?
- What are the magnetic properties of each IRD lithology? How do these differ and possibly allow distinction? Which IRD lithology has a decisive influence on the magnetic susceptibility? Can the overall magnetic susceptibility of HLs be explained and modeled from bulk sediment properties or IRD counts?
- How does randomness govern the stratigraphic distribution of IRD in sediments and how does it affect different types of magnetic susceptibility records? Does magnetic susceptibility offer technical ways to quantify lateral sediment inhomogeneity?

The specific materials and methods used in addressing the aforesaid questions are described in detail in each of the materials and methods sections of the respective chapters of this thesis.

1.4 Geological Settings

1.4.1 Tectonics and Geology of the Grand Banks

The configuration and inherent geomorphological structures of continental margins are mainly sculpted and transfigured by paleo-tectonic events and deep-sea sedimentary processes in the course of their evolution (Mosher et al., 2017). Before the plate tectonic

disintegration of Pangea, the Grand Banks formed the hub of the supercontinent encircled by the northwest African, Iberian, and European continental plates (Tankard and Welsink, 1988). It was separated from the Iberian margin through non-volcanic asymmetric rifting about ~130 Ma and recorded a distinct history of basin formation that showcased two phases of rift events and post-rift thermal subsidence (Gao et al., 2022; Mosher et al., 2017; Tankard and Welsink, 1988). The episodes of rifting regimes occurred during the Late Triassic to Early Jurassic and during the Late Jurassic to Early Cretaceous where the latter was more intense though it appears to have inherited some older structural trends from the former episode (Tankard and Welsink, 1988). As described by Tankard and Welsink (1988), the broad Grand Banks have a lateral extent of about 450 km seaward of Newfoundland that slopes unevenly into the North Atlantic basin. It is separated from Nova Scotia and Labrador by a narrow margin (southward) and a pronounced transform fault (northward) respectively. Geophysical investigations of the Grand Banks reveal a regional arcuate trend resulting from the collision of magmatic arcs (Haworth and MacIntyre, 1975). The Grand Banks represent the submerged eastern extension of the Newfoundland terrane complex with a bedrock made up of Precambrian to Paleozoic crystalline rocks and meta-sediments (Dalrymple et al., 1992; Jansa et al., 1976; Mosher et al., 2017).

The south-east Grand Banks slope was formed during the Early Cretaceous i.e. in the second phase of the rift event (Tucholke et al., 2006). It has a thinner sedimentary sequence than its southwestern counterpart because of the westward tilting of the rift event (Gao et al., 2022). However, it has a thick upper continental slope consisting of Quaternary sediments rich in IRD particles that were deposited during the Mid-Eocene (Rashid et al., 2019). The periodically submerged and iceberg-eroded southeastern Grand Banks were anomalously unglaciated during the Late Pleistocene expansion and contraction of ice sheets despite most of Newfoundland being covered by glaciers (Dalton et al., 2020).

1.4.2 IRD Provenance

It is well established that IRD fragments found in the Quaternary sediments of the North Atlantic were mainly derived from the hinterland geology of the circum-North Atlantic regions and beyond (Piper and DeWolfe, 2003). However, potential complications exist in performing detailed high-resolution exclusive IRD provenance studies (Hemming, 2004). First, the area coverage of the glacier complexes is huge and the underlying bedrock geology is so diverse producing detritus of various grain sizes. Secondly, the coarse-grained IRD, which provides realistic petrographic and geochemical records of individual IRD lithology, only represents a small fraction of the total IRD contained in the Quaternary sediments. The finer IRD grain sizes that constitute a significant portion are mainly monocrystalline and appear homogeneous in composition, making precise IRD provenance investigations difficult and uncertain (Hemming, 2004).

The gigantic ice mass of the North American ice-sheet complex (NAISC) has been overlaying the Canadian Shield and the Hudson and Foxe basins, which are comprised of diverse crystalline basement rocks of the Precambrian age. These crystalline rocks include both igneous and metamorphic lithologies where the metamorphism is mainly dominated by low-grade varieties. There are also significant formations of sedimentary and volcanic lithologies spread across the entire region (Fulton and Prest, 1987). The petrographic study of IRD

granules by Piper and DeWolfe (2003) proposed several probable sources of lithology-specific IRD particles by grouping the IRD fragments based on acquired sediment sample locations.

Physiographically, the studied sediments were obtained from continental margins down to the deep ocean, and the individual IRD provenances were classified into terrains and geologic ages. The investigated sediments retrieved at the Scotian margin revealed various IRD lithologies that include pink granite, black and white granite, rhyolite, black slate, etc. The respective provenances of these lithologies were inferred to be the Newfoundland Avalon Terrane (Paleozoic in age), Meguma group, Appalachian terranes, and Meguma Terrane. Grey carbonates, obtained from sediments of Laurentian Fan, have their sources traced to the Windsor group, while the white and tan (brown) dolostones of the Newfoundland margin are believed to be sourced from Paleozoic carbonates of the Hudson Strait.

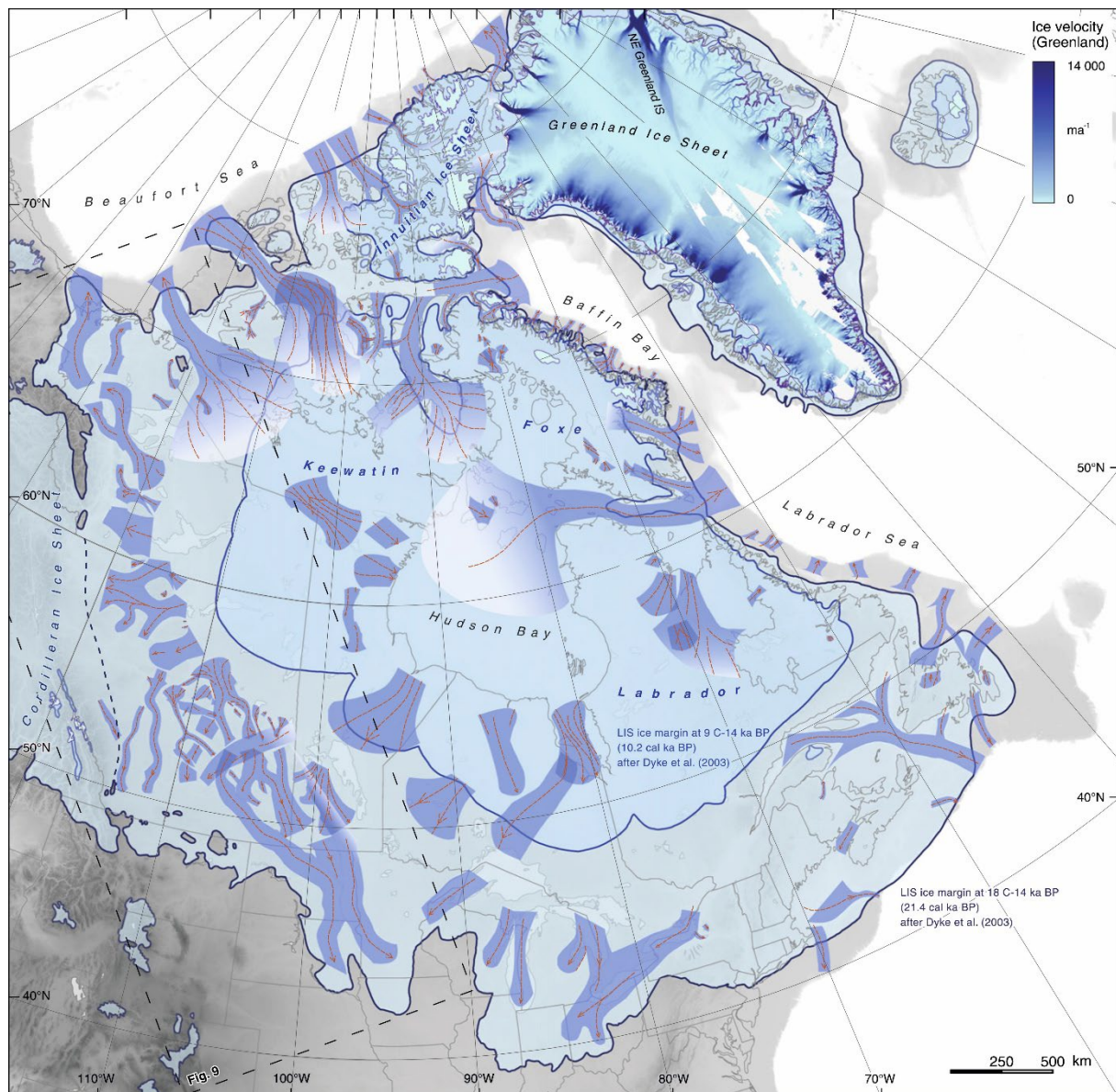


Figure 2: Glacial map of North American ice-sheet complex, the Laurentide ice sheet sub-sector, and Greenland. The ice margins are shown in thick blue lines with ice streams represented in thicker blue bands that mostly terminate in the Labrador Sea and the North Atlantic (Margold et al., 2015).

1.4.3 Dynamics of the Laurentide Ice Sheet

Though the continuous stratigraphic record of core GeoB18530-1 investigated in this PhD project covers up to the Marine Isotope Stage 3 (MIS3) period, the deglaciation and ice dynamics of sub-section of the North American ice-sheet complex (NAISC) that would be presented (Figure 2) here on the basis of available records in literature extends only to the Late Wisconsinan period (Dalton et al., 2020; Dyke, 2004). As reported in many studies, the enormous ice mass of NAISC consisted of the Laurentide, Cordilleran, Innuitian, and Greenland ice sheets that expanded and shrank systematically during the Quaternary period. The Laurentide ice sheet (LIS) which is usually considered the major source of IRD is also subdivided into three domes, namely, Labrador, Keewatin, and Baffin sectors where each of the names was derived from the area of initial ice inception (Bond et al., 1992; Fulton and Prest, 1987; Margold et al., 2015).

The reduction in ice sheet mass requires thawing and/or ice calving that are eventually discharged into structural conduits referred to as ice streams. For many years, discharges from ice sheets were conceived as drains via a few number of fast-moving ice streams however, the study of balance velocities by Bamber et al. (2000) revealed a more complex system. In that, individual drainage basins are fed by several systems of tributaries that are extensive stretching up to 1000 km into ice sheets. This highlights the complexity and significance of ice streams that account for major mass losses in ice sheets (Margold et al., 2015).

During the Late Wisconsinan period, northern hemisphere ice sheets attained their maximum extent stretching into shelf edges (Piper and DeWolfe, 2003; Piper and Skene, 1998). This phase of global ice sheet volume increase is referred to as the Last Glacial Maximum (LGM) or Last Glaciation in literature (Mix, 2001; Shaw et al., 2006). The precise time frame at which the integral growth in glacier volume occurred is under contention as the evidence that constraint the age is somewhat a mixed bag (Shaw et al., 2006). The Labrador sector of the Laurentide ice sheet widens up to the continental margin of eastern Canada (Figure 2) during the LGM period. The ice mass was divided into two ridges with relatively high relief and dissected by low altitude re-entrant of the Gulf of St. Lawrence (Shaw et al., 2006).

1.5 Thesis Outline

This cumulative PhD thesis is structured based on three manuscripts, of which the first manuscript is submission-ready, but waiting for the second companion manuscript to have the consent of the coauthors before double submission to G3. The third manuscript is likewise completed and will be submitted after the editorial decision on the previous manuscripts. The individual manuscripts are referred to as chapters 2, 3, and 4.

Chapter 2: Ice-Rafted Detritus (IRD) of the SE Grand Banks Slope, Newfoundland, Throughout Heinrich Layers 1 to 6 - Part I: Petrology and Abundance (*ready for submission to Journal of Geochemistry, Geophysics, Geosystem – G3*)

Author and Co-Authors: *Shettima Bukar, Frank Lisker, Tilo von Dobeneck, Lars Max, Yiyung Wang, Marlene Baumer, Stefan Mulitza, Guillaume St-Onge and David Piper*

In Part I of the study, coarse ice-rafted detritus (IRD) was investigated from a glaciomarine sediment core obtained at South-east Grand Bank Slope, Newfoundland. IRD petrology

identification, determination of abundances, classification, and preferential deposition within stratigraphic layers were resolved by employing techniques that include petrography (thin section analysis), binocular and high-resolution digital microscopy, X-ray Fluorescence and statistical analysis of IRD of data. The age model of the whole core was established using published radiocarbon dates (^{14}C -AMS) and North Greenland Ice Core Project (NGRIP) $\delta^{18}\text{O}$ data.

The research concept was jointly developed by SB and TvD. SB performed all microscopic studies (identification and counts) and developed the petrological IRD classification scheme. FL advised the thin section analysis and revised the petrography chapters. LM provided XRF data. YW prepared the sieved XRD samples during her former MSc study. MB provided oxygen isotope data for chronostratigraphy. SM collected the studied core on the MSM39 cruise and advised on age modeling. GSO acted as the external ArcTrain PhD thesis supervisor and revised the manuscript. DP, a leading Canadian expert on IRD petrology and distribution, revised and commented on the manuscript. The draft version of the manuscript was written by SB except for statistics Chapter 6, which was written by TvD.

Chapter 3: Ice-Rafted Detritus (IRD) of the SE Grand Banks Slope, Newfoundland, Throughout Heinrich Layers 1 to 6 - Part II: Magnetic Properties Abundance (*in preparation for submission to Journal of Geochemistry, Geophysics, Geosystem – G3*)

Author and Co-Authors: *Shettima Bukar, Tilo von Dobeneck, Yiyung Wang, Lars Max, Thomas Frederichs, Edoardo Dallanave, Guillaume St-Onge.*

Part II of the investigation was built upon finding the link between petrological variability, i.e. the varied magnetic mineral composition of IRD particles and their respective influences on the emblematic magnetic susceptibility characteristics of Heinrich event layers. To achieve this, various rock magnetic parameters of bulk samples and extracted classified IRD lithologies were investigated. We also included existing X-ray fluorescence data and performed a magnetic analysis of sieve fractions. Based on various magnetic susceptibility models, an inference could be drawn on the interplay of low-magnetic dolomitic IRD and high-magnetic granitic IRD. It could also be shown, that alternative (nepheloid, gravitational, hyperpycnal, etc.) modes of glaciomarine sedimentation transport beyond ice-rafting must have been active and massively contributed to sediment composition and hence also magnetic susceptibility.

SB realized all rock magnetic investigations of classified IRD and performed the wet sieve analysis and its magnetic investigation. YW provided bulk rock magnetic data and the non-classified IRD counts of her MSc study. LM measured the XRF data. TF advised and enabled special rock magnetic laboratory work. The draft was written jointly by SB (Chapters 1, 2, and 4) and TvD (Chapters 3 and 5) partly based on a reanalysis of the MSc thesis data by YW. ED and GSO will revise the entire manuscript in short.

Chapter 4: Imprint and Assessment of Random Deposition and Lithological Variability of Ice-rafted Debris (IRD) in Magnetic Susceptibility Records (*in preparation for journal submission*)

Author and Co-Authors: *Shettima Bukar, Tilo von Dobeneck, Thomas Frederichs, Yiyung Wang, Guillaume St-Onge*

This study examines the impact of the stochastic spatial distribution and lithological diversity of coarser IRD particles on magnetic susceptibility records by various logging techniques.

Different sample sets were used to observe the significance of magnetic susceptibility sensor designs on generated signals. With certain limitations regarding the depth of magnetic field penetration in a split core sample, multiple line scanning of a split sediment core presents the fastest and most precise signal that resolves the internal spread of IRD in a core and also allows us to determine an estimate of lateral sediment inhomogeneity.

SB performed the multiple-track susceptibility scans. TvD developed the idea of parallel spot sensor measurements, for which TF built and programmed the required technical extensions of the split-core logger. YW first measured and statistically interpreted such data. SB prepared all figures and wrote the manuscript, which will be revised by TvD and GSO, respectively.

1.6 References

- Alley, R.B., MacAyeal, D.R., 1994. Ice-rafted debris associated with binge/purge oscillations of the Laurentide Ice Sheet. *Paleoceanography* 9, 503–511. <https://doi.org/10.1029/94PA01008>
- Andrews, J.T., 2000. Icebergs and iceberg rafted detritus (IRD) in the North Atlantic: facts and assumptions. *Oceanography* 13, 100–108.
- Andrews, J.T., Tedesco, K., 1992. Detrital carbonate-rich sediments, northwestern Labrador Sea: Implications for ice-sheet dynamics and iceberg rafting (Heinrich) events in the North Atlantic. *Geol* 20, 1087. [https://doi.org/10.1130/0091-7613\(1992\)020<1087:DCRSNL>2.3.CO;2](https://doi.org/10.1130/0091-7613(1992)020<1087:DCRSNL>2.3.CO;2)
- Bamber, J.L., Vaughan, D.G., Joughin, I., 2000. Widespread complex flow in the interior of the antarctic ice sheet. *Science* 287, 1248–1250.
- Bond, G., Heinrich, H., Broecker, W., Labeyrie, L., McManus, J., Andrews, J., Huon, S., Jantschik, R., Clasen, S., Simet, C., Tedesco, K., Klas, M., Bonani, G., Ivy, S., 1992. Evidence for massive discharges of icebergs into the North Atlantic ocean during the last glacial period. *Nature* 360, 245–249. <https://doi.org/10.1038/360245a0>
- Bond, G.C., Lotti, R., 1995a. Iceberg Discharges into the North Atlantic on Millennial Time Scales During the Last Glaciation. *Science* 267, 1005–1010. <https://doi.org/10.1126/science.267.5200.1005>
- Bond, G.C., Lotti, R., 1995b. Iceberg Discharges into the North Atlantic on Millennial Time Scales During the Last Glaciation. *Science* 267, 1005–1010. <https://doi.org/10.1126/science.267.5200.1005>
- Broecker, W., Bond, G., Klas, M., Clark, E., McManus, J., 1992. Origin of the northern Atlantic's Heinrich events. *Climate Dynamics* 6, 265–273. <https://doi.org/10.1007/BF00193540>
- Dalrymple, R.W., LeGresley, E.M., Fader, G.B.J., Petrie, B.D., 1992. The western Grand Banks of Newfoundland: Transgressive Holocene sedimentation under the combined influence of waves and currents. *Marine Geology* 105, 95–118. [https://doi.org/10.1016/0025-3227\(92\)90184-J](https://doi.org/10.1016/0025-3227(92)90184-J)
- Dalton, A.S., Margold, M., Stokes, C.R., Tarasov, L., Dyke, A.S., Adams, R.S., Allard, S., Arends, H.E., Atkinson, N., Attig, J.W., Barnett, P.J., Barnett, R.L., Batterson, M., Bernatchez, P., Borns, H.W., Breckenridge, A., Briner, J.P., Brouard, E., Campbell, J.E., Carlson, A.E.,

- Clague, J.J., Curry, B.B., Daigneault, R.-A., Dubé-Loubert, H., Easterbrook, D.J., Franzi, D.A., Friedrich, H.G., Funder, S., Gauthier, M.S., Gowan, A.S., Harris, K.L., Hétu, B., Hooyer, T.S., Jennings, C.E., Johnson, M.D., Kehew, A.E., Kelley, S.E., Kerr, D., King, E.L., Kjeldsen, K.K., Knaeble, A.R., Lajeunesse, P., Lakeman, T.R., Lamothe, M., Larson, P., Lavoie, M., Loope, H.M., Lowell, T.V., Lusardi, B.A., Manz, L., McMartin, I., Nixon, F.C., Occhietti, S., Parkhill, M.A., Piper, D.J.W., Pronk, A.G., Richard, P.J.H., Ridge, J.C., Ross, M., Roy, M., Seaman, A., Shaw, J., Stea, R.R., Teller, J.T., Thompson, W.B., Thorleifson, L.H., Utting, D.J., Veillette, J.J., Ward, B.C., Weddle, T.K., Wright, H.E., 2020. An updated radiocarbon-based ice margin chronology for the last deglaciation of the North American Ice Sheet Complex. *Quaternary Science Reviews* 234, 106223. <https://doi.org/10.1016/j.quascirev.2020.106223>
- Dowdeswell, J.A., Elverhøi, A., Andrews, J.T., Hebbeln, D., 1999. Asynchronous deposition of ice-rafted layers in the Nordic seas and North Atlantic Ocean. *Nature* 400, 348–351. <https://doi.org/10.1038/22510>
- Dowdeswell, J.A., Maslin, M.A., Andrews, J.T., McCave, I.N., 1995. Iceberg production, debris rafting, and the extent and thickness of Heinrich layers (H-1, H-2) in North Atlantic sediments. *Geology* 23, 301–304. [https://doi.org/10.1130/0091-7613\(1995\)023<0297:IPDRAT>2.3.CO;2](https://doi.org/10.1130/0091-7613(1995)023<0297:IPDRAT>2.3.CO;2)
- Dyke, A.S., 2004. An outline of North American deglaciation with emphasis on central and northern Canada, in: Ehlers, J., Gibbard, P.L. (Eds.), *Developments in Quaternary Sciences, Quaternary Glaciations-Extent and Chronology*. Elsevier, pp. 373–424. [https://doi.org/10.1016/S1571-0866\(04\)80209-4](https://doi.org/10.1016/S1571-0866(04)80209-4)
- Fulton, R.J., Prest, V.K., 1987. Introduction: The Laurentide Ice Sheet and its Significance. *Géographie physique et Quaternaire* 41, 181. <https://doi.org/10.7202/032676ar>
- Ganopolski, A., 2024. Toward generalized Milankovitch theory (GMT). *Clim. Past* 20, 151–185. <https://doi.org/10.5194/cp-20-151-2024>
- Gao, Y., Piper, D.J.W., Normandeau, A., Xie, X., 2022. Late Pleistocene- Holocene architecture and sedimentary processes on the glacially influenced SW Grand Banks Slope off Newfoundland. *Marine Geology* 451, 106883. <https://doi.org/10.1016/j.margeo.2022.106883>
- Gil, I.M., Keigwin, L.D., 2018. Last Glacial Maximum surface water properties and circulation over Laurentian Fan, western North Atlantic. *Earth and Planetary Science Letters* 500, 47–55. <https://doi.org/10.1016/j.epsl.2018.07.038>
- Grousset, F.E., Labeyrie, L., Sinko, J.A., Cremer, M., Bond, G., Duprat, J., Cortijo, E., Huon, S., 1993a. Patterns of Ice-Rafted Detritus in the Glacial North Atlantic (40–55°N). *Paleoceanography* 8, 175–192. <https://doi.org/10.1029/92PA02923>
- Grousset, F.E., Labeyrie, L., Sinko, J.A., Cremer, M., Bond, G., Duprat, J., Cortijo, E., Huon, S., 1993b. Patterns of Ice-Rafted Detritus in the Glacial North Atlantic (40–55°N). *Paleoceanography* 8, 175–192. <https://doi.org/10.1029/92PA02923>
- Haworth, A.G.S.R.T., Macintyre, J.B., 1975. The gravity and magnetic fields of Atlantic offshore Canada, *Geological Magazine* 114(1):75-75. <https://doi.org/10.1017/S0016756800043533>
- Heinrich, H., 1988. Origin and Consequences of Cyclic Ice Rafting in the Northeast Atlantic Ocean During the Past 130,000 Years. *Quat. res.* 29, 142–152. [https://doi.org/10.1016/0033-5894\(88\)90057-9](https://doi.org/10.1016/0033-5894(88)90057-9)

- Hemming, S.R., 2004a. Heinrich events: Massive late Pleistocene detritus layers of the North Atlantic and their global climate imprint. *Reviews of Geophysics* 42, 2003RG000128. <https://doi.org/10.1029/2003RG000128>
- Hemming, S.R., 2004b. Heinrich events: Massive late Pleistocene detritus layers of the North Atlantic and their global climate imprint: HEINRICH EVENTS. *Rev. Geophys.* 42. <https://doi.org/10.1029/2003RG000128>
- Hesse, R., 2016. Ice-proximal Labrador Sea Heinrich layers: a sedimentological approach. *Can. J. Earth Sci.* 53, 71–100. <https://doi.org/10.1139/cjes-2015-0033>
- Hesse, R., Khodabakhsh, S., 2016. Anatomy of Labrador Sea Heinrich layers. *Marine Geology* 380, 44–66. <https://doi.org/10.1016/j.margeo.2016.05.019>
- Hodell, D.A., Nicholl, J.A., Bontognali, T.R.R., Danino, S., Dorador, J., Dowdeswell, J.A., Einsle, J., Kuhlmann, H., Martrat, B., Mlenek-Vautravers, M.J., Rodríguez-Tovar, F.J., Röhl, U., 2017. Anatomy of Heinrich Layer 1 and its role in the last deglaciation: HEINRICH EVENT 1. *Paleoceanography* 32, 284–303. <https://doi.org/10.1002/2016PA003028>
- JANSA, L., FM, G., IM, H., WAM, J., GL, W., 1976. STRATIGRAPHY OF THE AMOCO-IOE MURRE G-67 WELL, GRAND BANKS OF NEWFOUNDLAND. STRATIGRAPHY OF THE AMOCO-IOE MURRE G-67 WELL, GRAND BANKS OF NEWFOUNDLAND.
- Leng, W., Von Dobeneck, T., Bergmann, F., Just, J., Mulitza, S., Chiessi, C.M., St-Onge, G., Piper, D.J.W., 2018. Sedimentary and rock magnetic signatures and event scenarios of deglacial outburst floods from the Laurentian Channel Ice Stream. *Quaternary Science Reviews* 186, 27–46. <https://doi.org/10.1016/j.quascirev.2018.01.016>
- Leng, W., von Dobeneck, T., Just, J., Govin, A., St-Onge, G., Piper, D.J.W., 2019. Compositional changes in deglacial red mud event beds off the Laurentian Channel reveal source mixing, grain-size partitioning and ice retreat. *Quaternary Science Reviews* 215, 98–115. <https://doi.org/10.1016/j.quascirev.2019.04.031>
- MacAyeal, D.R., 1993. Binge/purge oscillations of the Laurentide Ice Sheet as a cause of the North Atlantic's Heinrich events. *Paleoceanography* 8, 775–784. <https://doi.org/10.1029/93PA02200>
- Margold, M., Stokes, C.R., Clark, C.D., 2015. Ice streams in the Laurentide Ice Sheet: Identification, characteristics and comparison to modern ice sheets. *Earth-Science Reviews* 143, 117–146. <https://doi.org/10.1016/j.earscirev.2015.01.011>
- Max, L., Nürnberg, D., Chiessi, C.M., Lenz, M.M., Mulitza, S., 2022. Subsurface ocean warming preceded Heinrich Events. *Nat Commun* 13, 4217. <https://doi.org/10.1038/s41467-022-31754-x>
- Meyer, C.R., Robel, A.A., Rempel, A.W., 2019. Frozen fringe explains sediment freeze-on during Heinrich events. *Earth and Planetary Science Letters* 524, 115725. <https://doi.org/10.1016/j.epsl.2019.115725>
- Mix, A., 2001. Environmental processes of the ice age: land, oceans, glaciers (EPILOG). *Quaternary Science Reviews* 20, 627–657. [https://doi.org/10.1016/S0277-3791\(00\)00145-1](https://doi.org/10.1016/S0277-3791(00)00145-1)
- Mosher, D.C., Campbell, D.C., Gardner, J.V., Piper, D.J.W., Chaytor, J.D., Rebesco, M., 2017. The role of deep-water sedimentary processes in shaping a continental margin: The

- Northwest Atlantic. *Marine Geology, Advancements in Understanding Deep-Sea Clastic Sedimentation Processes* 393, 245–259. <https://doi.org/10.1016/j.margeo.2017.08.018>
- Ó Cofaigh, C., 2013. GLACIAL LANDFORMS, SEDIMENTS | Glaciomarine Sediments and Ice-Rafted Debris, in: *Encyclopedia of Quaternary Science*. Elsevier, pp. 30–42. <https://doi.org/10.1016/B978-0-444-53643-3.00085-6>
- Piper, D.J.W., DeWolfe, M., 2003. Petrographic evidence from the eastern Canadian margin of shelf-crossing glaciations. *Quaternary International* 99–100, 99–113. [https://doi.org/10.1016/S1040-6182\(02\)00115-5](https://doi.org/10.1016/S1040-6182(02)00115-5)
- Piper, D.J.W., Skene, K.I., 1998. Latest Pleistocene ice-rafting events on the Scotian Margin (eastern Canada) and their relationship to Heinrich events. *Paleoceanography* 13, 205–214. <https://doi.org/10.1029/97PA03641>
- Rashid, H., Grosjean, E., 2006. Detecting the source of Heinrich layers: An organic geochemical study: DETECTING THE SOURCE OF HEINRICH LAYERS. *Paleoceanography* 21. <https://doi.org/10.1029/2005PA001240>
- Rashid, H., Hesse, R., Piper, D.J.W., 2003. Evidence for an additional Heinrich event between H5 and H6 in the Labrador Sea: HEINRICH EVENT 5A IN THE LABRADOR SEA. *Paleoceanography* 18, n/a-n/a. <https://doi.org/10.1029/2003PA000913>
- Rashid, H., Piper, D.J.W., MacKillop, K., Ouellette, D., Vermooten, M., Muñoz, A., Jiménez, P., 2019. Dynamics of sediments on a glacially influenced, sediment starved, current-swept continental margin: The SE Grand Banks Slope off Newfoundland. *Marine Geology* 408, 67–86. <https://doi.org/10.1016/j.margeo.2018.11.012>
- Rashid, H., Saint-Ange, F., Barber, D.C., Smith, M.E., Devalia, N., 2012. Fine scale sediment structure and geochemical signature between eastern and western North Atlantic during Heinrich events 1 and 2. *Quaternary Science Reviews* 46, 136–150. <https://doi.org/10.1016/j.quascirev.2012.04.026>
- Ruddiman, W.F., 1977. Late Quaternary deposition of ice-rafted sand in the subpolar North Atlantic (lat 40° to 65°N). *GSA Bulletin* 88, 1813–1827. [https://doi.org/10.1130/0016-7606\(1977\)88<1813:LQDOIS>2.0.CO;2](https://doi.org/10.1130/0016-7606(1977)88<1813:LQDOIS>2.0.CO;2)
- Shaw, J., Piper, D.J.W., Fader, G.B.J., King, E.L., Todd, B.J., Bell, T., Batterson, M.J., Liverman, D.G.E., 2006. A conceptual model of the deglaciation of Atlantic Canada. *Quaternary Science Reviews* 25, 2059–2081. <https://doi.org/10.1016/j.quascirev.2006.03.002>
- Tankard, A.J., Welsink, H.J., 1988. Extensional tectonics, structural styles and stratigraphy of the Mesozoic Grand Banks of Newfoundland, in: *Developments in Geotectonics*. Elsevier, pp. 129–165. <https://doi.org/10.1016/B978-0-444-42903-2.50011-7>
- Tucholke, B.E., Sibuet, J.-C., Klaus, A. (Eds.), 2006. *Proceedings of the Ocean Drilling Program, 210 Scientific Results, Proceedings of the Ocean Drilling Program*. Ocean Drilling Program. <https://doi.org/10.2973/odp.proc.sr.210.2007>

Chapter 2: Ice-Rafted Detritus (IRD) of the SE Grand Banks Slope, Newfoundland, Throughout Heinrich Layers 1 to 6 - Part I: Petrology and Abundance

S. Bukar^{1*}, F. Lisker¹, T. von Dobeneck^{1,2}, L. Max², Y. Wang¹, M. Baumer¹, S. Mulitza^{1,2}, G. St-Onge³, D. Piper⁴

¹ Faculty of Geosciences, University of Bremen, Bremen, Germany

² MARUM-Center for Marine Environmental Sciences

³ Institut Sciences de la mer de Rimouski ISMER, Canada Research Chair in Marine Geology, Université du Québec à Rimouski and GEOTOP, Canada

⁴ Natural Resources Canada, Geological Survey of Canada, Bedford Institute of Oceanography, Dartmouth, NS, Canada

Abstract

Throughout the continuous late Pleistocene stratigraphic sequence of Heinrich Event layers 1 - 6 in sediments of Newfoundland Southeast Grand Banks Slope, coarse grained (> 1 mm) ice rafted detritus (IRD) is ubiquitous, diverse in petrology and variable in abundance. Using digital light microscopy and thin section analysis, the individual compositional mineralogy of IRD particles was photographically reproduced, petrographically examined, accurately described, and named. From 8243 identified particles, we establish a new IRD classification scheme of 22 prevalent and optically discernable rock types and rock-forming minerals. The abundance of each IRD species was counted at 2 cm resolution over the 500 cm long section of gravity core GeoB 18530-1. The resulting time series provide a complex integral geological record of the Laurentide Ice Sheet calving and episodic collapse during MIS 3 and MIS 2. The count statistics also permit the division the 22 IRD classes into three separate groups by using a proportional or disproportional deposition within Heinrich layers and interlayers as criterion. Heinrich Layers 1, 2, 4 and 5 were found to be compositionally similar, while Heinrich Layers 3 and 6 have some deviating IRD components. IRD of ooid-bearing dolomite clearly dominates the mid-parts of all Heinrich Layers, whereas muscovite-biotite granite is enhanced at their tops and bottoms. Sediment interlayers contain numerous characteristic and distinct 'background' IRD lithologies, whose relative contributions gradually change over the late Wisconsinan stage (60 – 15 ka).

Key Points

- Twenty-two distinct lithologies of ice rafted detritus were microscopically identified and counted throughout Heinrich Layers 1 to 6.
- These lithologies can be divided into three groups on the basis of their preferential or non-preferential deposition within Heinrich layers and interlayers.
- Heinrich layers 1-5 have twin peaks of IRD content relating to two phases of iceberg surges during each ice-sheet collapse

2.1 Introduction

The dynamics and interaction of the glacial North Atlantic Ocean and its circumjacent continental ice sheets are an eminent research issue of Late Pleistocene paleoclimatology because of their strikingly dynamic nature (Bond & Lotti, 1995; Max et al., 2022). The possibly most emblematic expressions of this interactivity are episodic massive discharges of sediment-carrying icebergs primarily from the Laurentide Ice Sheet (LIS) into the North Atlantic. These are termed Heinrich events (HEs; Broecker et al., 1992) and resulted in the formation of glaciomarine Heinrich layers (HLs; Bond et al., 1992; Heinrich, 1988).

In the open North Atlantic Ocean, HLs are mainly confined to a region from 46° to 50°N, commonly referred to as the 'Ruddiman Belt' (Ruddiman, 1977), where the thickness of the HL beds tapers from several meters to decimeters in the northwest to a few centimeters in the east (Dowdeswell et al., 1999). In Marine Isotope Stages (MIS) 3 and 2, i.e. from 57 – 14 ka, six ocean-wide HL units (here abbreviated as H1-H6), some with subdivisions, have been identified (Hodell et al., 2017; Rashid et al., 2003). HLs are usually recognized by their lithological distinctiveness, given by an enhanced content in lithic, mostly carbonate ice-rafted detritus (IRD) and the predominance of the Arctic foraminifera species *Neogloboquadrina pachyderma* (Bond et al., 1992; Grousset et al., 2000; Heinrich, 1988; Naafs et al., 2013; Piper et al., 2012).

Compositionally, the IRD fractions contained within HLs and their interlayers (ILs) are of diverse petrology owing to the complex bedrock geology of the parental sources enveloped by the LIS. IRD fragments representing a range of common rocks and rock-forming minerals are ubiquitous throughout the stratigraphic sequences of northern North Atlantic Late Pleistocene sediments. This hints at the presence of melting icebergs also during post and pre-Heinrich-Event phases (Bond & Lotti, 1995; Piper & DeWolfe, 2003). While the abundance of certain lithic fractions is high and systematic in all HLs, a permanent and increasing 'background' IRD deposition from MIS 3 to MIS 2 can be observed in some North Atlantic records (Bond & Lotti, 1995).

At the Atlantic Canadian Scotian and Grand Banks margins, Late Pleistocene IRD occurs in three distinct sediment types: 1) Detrital carbonate-rich HLs from sources of the greater Hudson Bay region are extensively found in the North Atlantic and thickest in the Labrador Sea (Andrews & Tedesco, 1992; Piper & DeWolfe, 2003; Harunur Rashid & Grosjean, 2006; Stoner et al., 1996), 2) Brick-red sandy mud strata with some IRD were deposited by subglacial outburst floods from the Gulf of St. Lawrence (Leng et al., 2018, 2019; Piper & DeWolfe, 2003; Piper & Skene, 1998). 3) Wisconsinan layers with sparsely distributed IRD fractions possibly originated from the north of the Labrador Sea or localized ice calving margins (Piper & DeWolfe, 2003).

A considerable amount of information has been gleaned from lithological studies of glaciomarine deposits. Petrographic classifications of IRD materials (usually of particles >125µm) have been conducted to delineate the locations of ice calving margins, the periodic intervals of icebergs surges and the chronological sequence of icebergs discharges into the North Atlantic from different adjacent ice sheets (Bond & Lotti, 1995; Grousset et al., 2001; Piper & DeWolfe, 2003). Most of these IRD investigations refer to the two late HLs 1 and 2 with less or no emphasis on the remaining four well-established HLs 3 to 6.

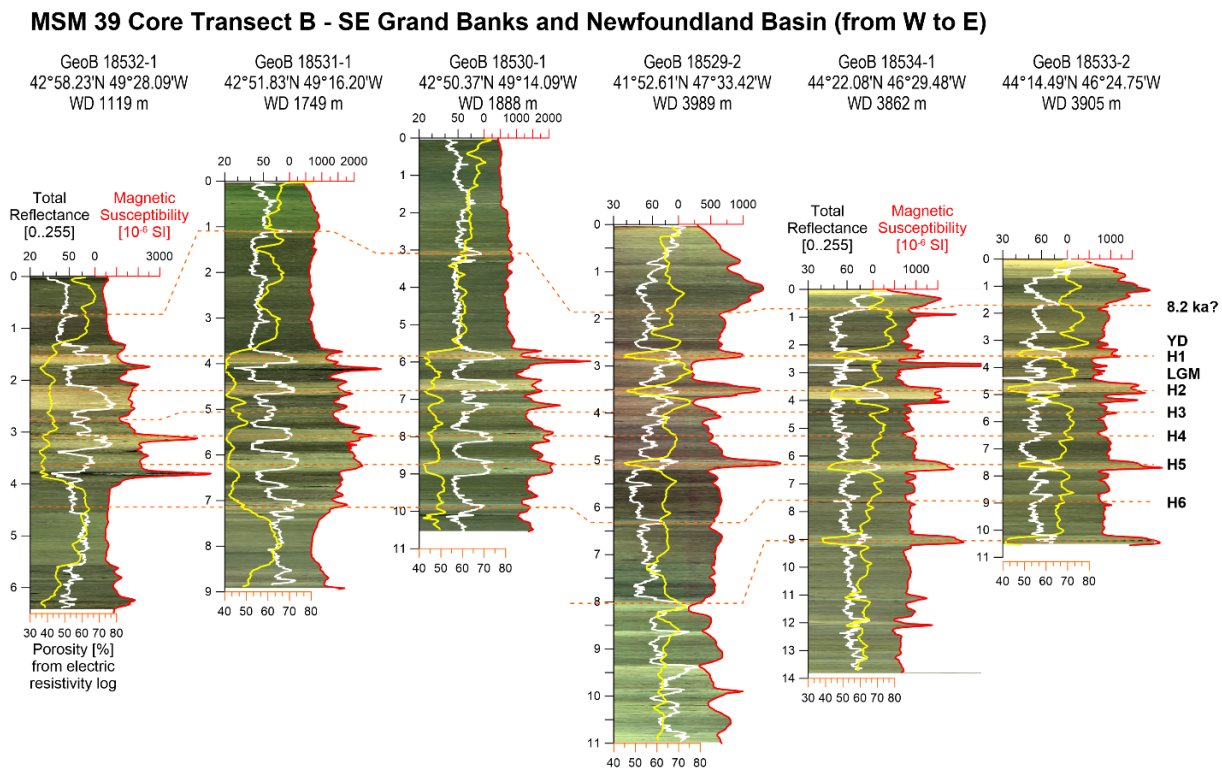


Figure 1: Shipboard physical property logs and core stratigraphy of six gravity cores (study core highlighted in red rectangle) acquired during the RV Maria S. Merian cruise MSM 39 (2014) at the lower SE Grand Banks slope of Newfoundland (Mulltza et al., 2015). All core logs show contrast-enhanced line scan images, total light reflectance (white line), magnetic susceptibility (red line) and porosity (white line) derived from electrical resistivity plotted against depth. Common peaks in magnetic susceptibilities and light reflectance associated with porosity lows were tentatively correlated with dashed red lines and inferred as HLs H1–H6, the Younger Dryas (YD) and/or the 8.2 ka event (Lajeunesse & St-Onge, 2008).

Non-destructive and rapid rock magnetic methods have been instrumental in the investigation of IRD-rich sediment records from early on (Robinson, 1986, 1993; Robinson et al., 1995). The most widely used IRD logging parameter is magnetic susceptibility (MS; Bond & Lotti, 1995; Robinson et al., 1995; Stoner et al., 1994), while the equally non-destructive color-scanning method primarily identifies IRD layers that are enriched in light carbonate/dolomite IRD. In contrast, the MS records of HLs are mainly related to IRD fractions originating from magmatic source rocks, which have far higher ferrimagnetic mineral contents than sedimentary source rocks (Bond & Lotti, 1995; Channell & Hodell, 2013; Stoner et al., 1996).

The six gravity cores (GeoB18529-2, 18530-1, 18531-1, 18532-1 and 18533-2) depicted by the core log correlation in Figure 1 were retrieved at the confluence zone of Labrador Current and Gulf Stream off the Southeast Grand Banks Slope during the German-Canadian RV Maria S. Merian cruise 39 in 2014 (Figure 2). In this northwestern North Atlantic region, sediment-laden icebergs transported south by the Labrador current are expected to intensify their thawing processes as they come in contact with warmer Gulf Stream waters, releasing IRD to the ocean floor. All cores share similarities in physical properties such as peaks in magnetic susceptibility, light bands in light reflectance and troughs in porosity that lend themselves for litho- and chronostratigraphic purposes (Figure 1). For this study, we opted for core Geo18530-1 as its six HLs H1-H6 appeared to be the most distinct and of considerable respective thickness (~40 cm).

By analyzing these sediments and their IRD fractions with petrological methods, we attempt to answer the some fundamental research questions for IRD provenance reconstructions:

- 1) Which petrologically distinct IRD granules (>1mm) were deposited throughout the Late Pleistocene sedimentary sequence of HEs H1-H6 and in what abundance?
- 2) Does the overall petrology of IRD follow certain systematic changes, trends and patterns during and between sediment units H1-H6?
- 3) Which IRD lithologies are specific for HEs, which are related to continuous glaciomarine background sedimentation, and which are associated to both of these processes?

This first part of our study has its focus on the detailed petrographic analysis of all observed IRD particles and their stratigraphic abundance, appearance and association, while the second part (Bukar et al., companion manuscript in preparation) regards the rock magnetic properties of the involved IRD lithologies, their specific impact on the bulk sediment properties and the clues that can be drawn from setting IRD counts and bulk data into relation. Put together, petrological IRD particle analyses and petromagnetic bulk and sieve fraction measurements create an eminent potential to elucidate Late Pleistocene glaciomarine sedimentation in the NW North Atlantic.

2.2 Geological setting

2.2.1 IRD Provenance and Source to Sink Transport

With the extension of the North American ice-sheet complexes during the Late Wisconsinan stage (~50 – 11 ka), most of Canada was enveloped by ice (Dalton et al., 2020; Dyke, 2004; Fulton & Prest, 1987). These ice sheets overlaid the Canadian shield, the Hudson and the Foxe basin regions where the bedrock geology is diverse with an age range of Precambrian to Paleozoic (Figure 2a). Broadly, some of the Precambrian lithologies include gabbro, anorthosite, granite, granodiorite, granite-gneiss, siliciclastic and volcanic rocks. Cambrian to Ordovician sedimentary rocks comprise limestone, dolomite and some siliciclastic rocks. Silurian to Carboniferous rocks encompass sandstone, shale, limestone and dolomite alongside some volcanics and Paleozoic felsic and mafic rocks. Younger preserved lithologies from the Late Cretaceous to Paleocene are mainly of basaltic nature (Fulton & Prest, 1987; Piper & DeWolfe, 2003; Simon et al., 2014).

The southeastward-oriented ice streams, i.e. Hudson Strait and Laurentian Channel, are the major conduit systems that delivered the icebergs and the subglacial meltwater into the adjacent North Atlantic Ocean (Piper et al., 2012; Rashid & Piper, 2007). Substantial amount of sediments transferred into the ocean basin are ultimately reworked and were transported to depositional areas by the Labrador current (Hesse & Khodabakhsh, 2016; Piper et al., 2012; Rashid et al., 2019).

2.2.2 South East Grand Banks Slope Settings

The Grand Banks of Newfoundland is an undersea appendage of the Avalon and Maguma terrane complex, that was separated by non-volcanic rifting of Newfoundland and Iberia at ~130 Ma (Mosher et al., 2017; Tucholke & Sibuet, 2006). It consists of chains of shallow banks that extend from Burgeo Bank in the west to Grand Banks and Flemish cap in the east which are set apart by deeper channels or enclosed basins (Figure 2b; Dalrymple et al., 1992). While

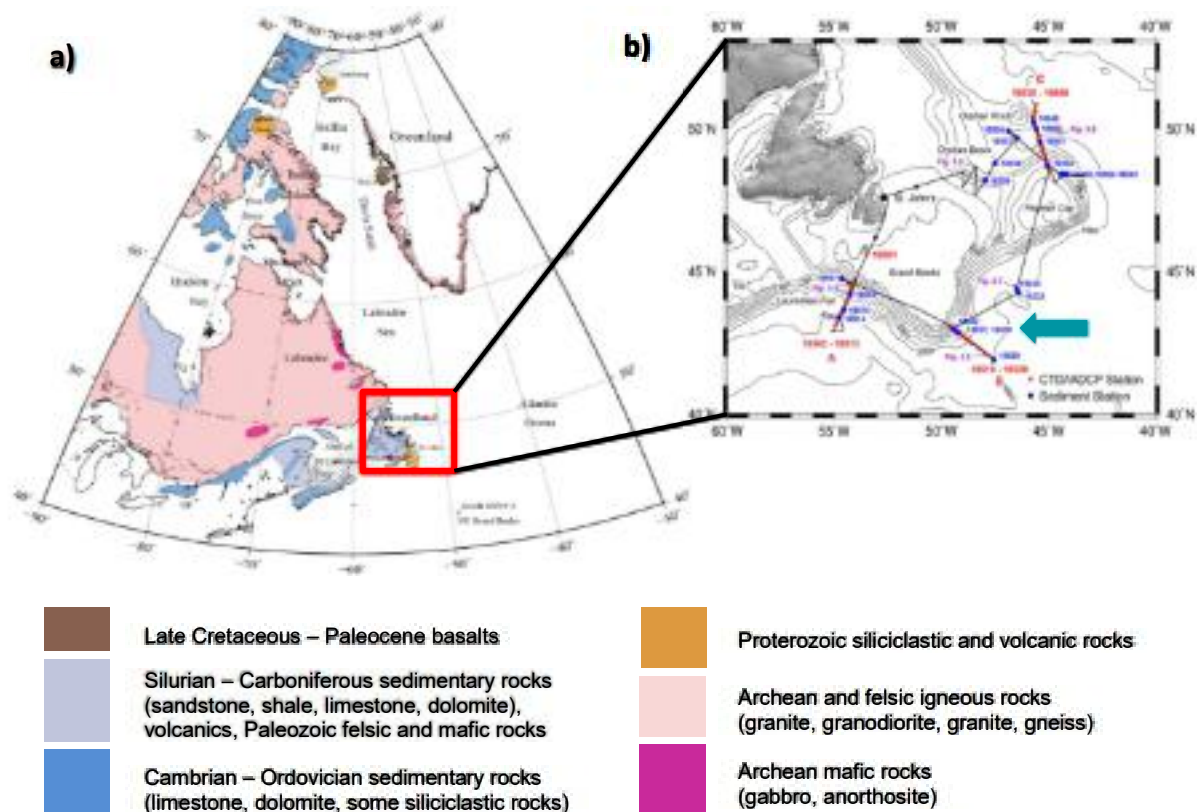


Figure 2: **a)** Simplified bedrock map of eastern Canada and western Greenland (from www.geogratis.gc.ca and modified after Bond & Lotti (1995), Piper & DeWolfe (2003) and Simon et al. (2014)). **b)** Map extract of the Newfoundland and Grand Banks coring and study area. Black lines represent MSM 39 cruise tracks, blue dots symbolize gravity coring sites and red dots CTD/IADCP stations (Mulitza et al., 2015).

glacial erosion was the usual process that sculpted most of the eastern Canadian margins, it is thought that the SE Grand Banks were anomalously unglaciated during the Late Pleistocene (Dalton et al., 2020). Although a glacial shield covered most of Newfoundland (Shaw et al., 2006), no ice streams have been recognized between Trinity Trough and Haddock Channel. Only comparably small-scaled ice-streams have been discerned in Labrador, NE Newfoundland, and the Scotian margin (Rashid et al., 2019). The SE Grand Banks slope has a characteristic feature of a deep shelf-break with an upper continental slope that consists mainly of thick sediments (including IRD) that started to form in mid-Eocene (Rashid et al., 2019).

2.3 Materials and Methods

2.3.1 Materials

Gravity core GeoB 18530-1 (42° 50.37' N, 49° 14.09' W, 1888 m water depth) was acquired at the foot of the southeastern Grand Banks slope of the Newfoundland margin during the RV Maria S. Merian cruise MSM39 (Mulitza et al., 2015). The 10.7 m long sediment core record provides an apparently continuous and complete record of all HLs (H1 to H6) and the deglacial and Holocene periods (Figure 1). Full core logging of magnetic susceptibility and electric conductivity at 2 cm resolution, physical lithological description and color line scanning were all performed aboard (Mulitza et al., 2015). The onshore sediment sampling for this study was done in two distinct sets, each consisting of 216 samples, at MARUM, University of Bremen.

Syringe samples of 10 cm³ were collected for sieving foraminifera (125 µm) and IRD (1 mm) fractions, while oriented paleomagnetic plastic cubes of 6.2cm³ for paleo- and rock magnetic purposes were subsampled at identical positions in steps of 2.3 cm from the lower half of the core (550-1054cm).

2.3.2 Methods

2.3.2.1 Shipboard Core Logging

Shipboard core logging was performed with a *GEOTEK Multi-Sensor Core Logger* (MSCL) equipped with a *Bartington* C-type magnetic susceptibility loop sensor and *GEOTEK Non-Contact Resistivity* (NCR) sensor. Line scan images were taken using a *GEOTEK GEOSCAN 2* color line scan camera and later enhanced by digital image processing. From these RGB images, averaged color reflectance values were retrieved from digital image sections of 10 cm x 1 cm (width x length), calibrated against color charts, and converted into lightness and red/blue ratios.

2.3.2.2 Sieve Analysis

The freeze-dried syringe samples were weighed to obtain dry bulk mass and subsequently diluted with 200 ml of demineralized water using manganese sulfate as anticoagulant to form a slurry. The mixture was then ultrasonically dispersed using a *BRANSON Sonifier 450* homogenizer for 3 – 5 minutes. A *FRITSCH Analysette 3* sifting machine with ISO-3310 sieves was used for wet sieving with a 125 µm mesh. This fractions was picked for foraminifera and other microfossil tests, leaving only sand-size lithic IRD particles behind. These were subsequently weighed and dry-sieved with a 1 mm mesh to collect the larger, petrologically identifiable IRD fragments. The intercepted granules (> 1mm) were thoroughly washed, oven-dried at 40°C and once more weighed so that IRD weight percentage of particles > 125 µm and >1 mm could be established.

2.3.2.3 Petrological Characterization and Counting of IRD particles

The initial examination of the IRD >1 mm was performed with a *Zeiss Stemi 2000* binocular microscope using white LED light to maintain pristine particle colors. A total of 8243 IRD clasts (>1 mm) from the 216 samples of the lower core section (550 – 1050 cm) were counted and characterized considering physical properties including color, hardness, cleavage, grain size, and texture. Based on these microscopic observations every IRD particle was classified in an evolving scheme of rocks and rock-forming minerals that was later validated and refined by SEM and thin section analysis.

2.3.2.4 Digital Microscopy of Selected IRD particles

Larger representative samples of each identified IRD lithology were imaged by high-resolution digital microscopy using a *Keyence VHX 6000* digital reflected light microscope at the MARUM micropaleontology lab. Digital microscopy provides an unlimited depth of field by stitching together sharp image sections obtained from a sweep of focal plane settings. The IRD particles were placed on a sticky white surface to prevent mechanical movement and color interference respectively. Image capturing settings of the digital microscope such as brightness, stitching number and sample elevation were adjusted accordingly. The images produced were subsequently processed and scaled using the *ImageJ* software.

2.3.2.5 Polarized Light Microscopy of IRD Thin Sections

Using the largest available IRD specimens of each classified lithology, 22 thin section slides of 30 μm thickness were prepared at the Geodynamics research lab of the University of Bremen. The IRD samples were fixed on a glass slide with double-sided adhesive tape (*Aslan* foil) and a Teflon ring of \varnothing 25 mm was placed around them. An epoxy resin (*Araldite 2020*) was applied to the sample and allowed to harden for 24 hrs. Some larger drop-stones had to be previously cut and roughly ground with silicon carbide, while most of the IRD particles were small enough to permit their complete epoxy embedding. Subsequently, the sample thickness was reduced to \sim 1000 μm with the aid of a diamond banded blade and ground down to \sim 150 μm thickness with an *MPS 120* machine and 64 μm diamond wheel. The final grinding to a thickness of 30 μm was obtained with an *MPS R300* machine with a 15 μm diamond wheel. The final slide polishing was done manually with a diamond solution (3 μm) and a silk plate. The observation of rock mineral properties under plane and cross-polarized light was done with *Leica EC3* (10x/0.25 objective lens) polarized light microscope. Image capturing and processing was performed with *LAS EZ* software, while image calibration and quality control were executed manually.

2.3.2.6 Oxygen Isotope Stratigraphy

For oxygen isotope stratigraphy of core GeoB18530-1, a high-resolution stable oxygen isotope ($\delta^{18}\text{O}$) record of *Neogloboquarina pachyderma sinistral* from the work of Max et al. (2022) was used for the upper core section (1 – 709 cm). An additional 32 samples covering the lower section of the core (721 – 1039.9 cm) were measured at MARUM, University of Bremen, using a *Finnigan MAT 251* gas isotope ratio mass spectrometer furnished with an automated *Kiel I* Carbonate Preparation Device. The entire $\delta^{18}\text{O}$ data were calibrated against a Bremen working standard (Solnhofen limestone) and the NBS19 (National Bureau of Standard) carbonate standards and converted to the VPDB (Vienna Pee Dee Belemnite) scale. The MARUM isotope lab's long-term analytical precision for $\delta^{18}\text{O}$ is 0.06‰.

2.3.2.7 X-ray Fluorescence Half Core Scanning

X-ray fluorescence (XRF) scanning of the archive halves was carried out using an *Avaatech* XRF Core Scanner at MARUM, University of Bremen at a resolution of 1 cm over an area of 1.2 cm^2 and under three different acceleration voltage settings for light (10 kV, 20 s, 150 Ma, for Ca), medium (30 kV, 20 s, 150 Ma, for Sr), and heavy (50 kV, 20 s, 800 Ma, for Sr) elements. To deter the effect of sensor contamination in the course of the XRF measurement, the split core section surfaces were covered with a 4 μm thin *SPEXCertiPrep Ultralene foil*. The main operating units of the core scanner encompass a *Canberra X-PIPS* Silicon Drift Detector (SDD; model SXD 15C-150-500) with 150 eV X-ray resolution, a *Canberra DAS 1000* Digital Spectrum Analyzer and an *Oxford Instruments 100 W Neptune* X-ray tube with rhodium (Rh) target material. The freshly acquired spectra were processed using the Iterative Least square software (WIN AXIL).

2.4 Litho- and Chronostratigraphy

The color line-scan image of Figure 3a shows six distinct HL units H1-H6 that appear in the lower part as alternating light bands of detrital carbonate-rich sediment with partly sharp and partly gradual contacts to the intermediary, more clayey dark-olive-grey ambient sediment units I1-I5 with abridged I6. A briefer light band within the Holocene unit of the upper core denotes the Younger Dryas (YD) which terminated the massive fluxes of IRD in the Quaternary period. To facilitate stratigraphic comparison, all further shown core data will be calibrated to the same lithological scaling based on the high-resolution XRF record of the Ca/Sr ratio. This widely used marker for HLs registers an amplitude increment at each of the detrital carbonate-rich layers, which are thought to originate from the Paleozoic limestone and dolostone of Hudson Bay and Hudson Strait (Broecker et al., 1992).

The $\delta^{18}\text{O}$ data (Figure 3a) show a continuous record with low amplitude at each of all HLs except H3, where the drawdown in $\delta^{18}\text{O}$ is less pronounced. The decline of $\delta^{18}\text{O}$ values at HLs is a well-known effect caused by massive meltwater incursion as well as the melt produced by icebergs during the HEs (Hesse & Khodabakhsh, 2016; Rashid et al., 2003).

The olive-grey uppermost 560 cm deglacial to Holocene section (including the YD unit) consists of non-reworked muddy to sandy foraminifer-bearing siliciclastic sediment. Patches of black,

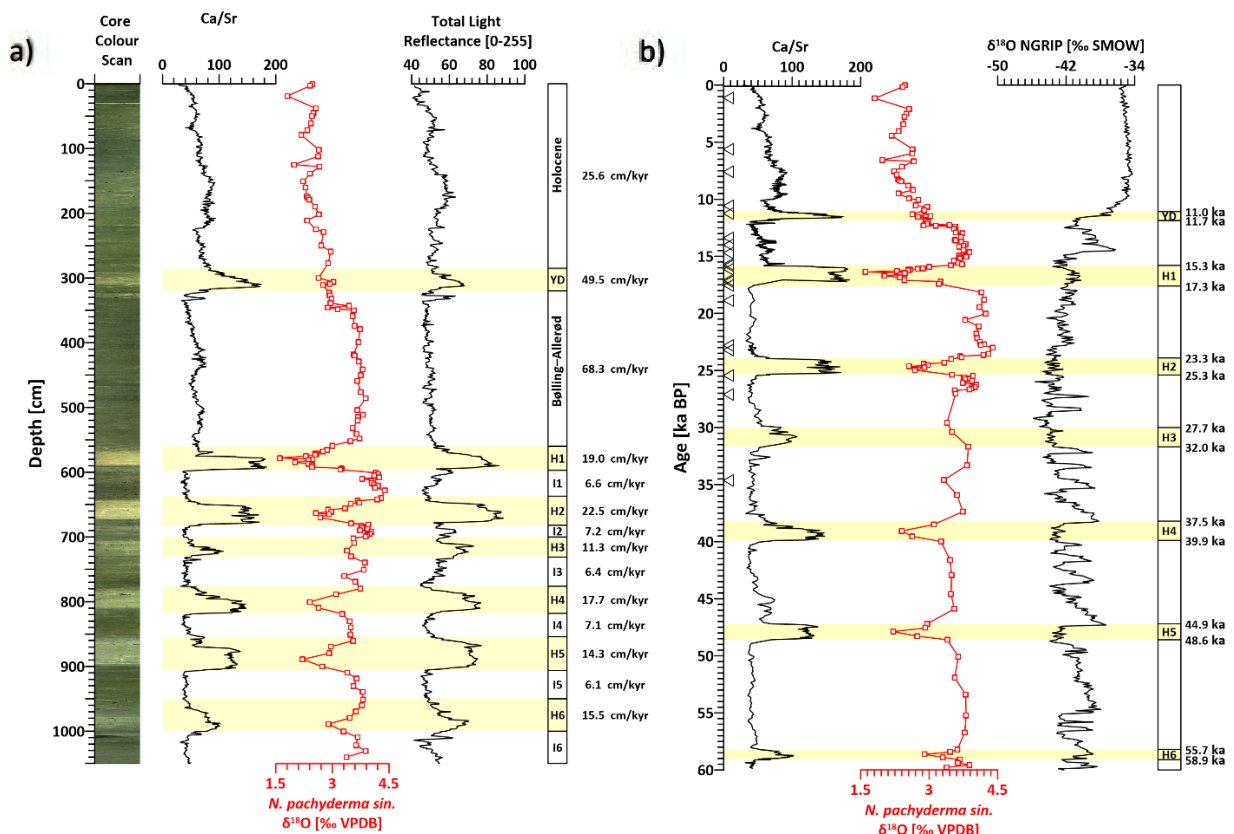


Figure 3: (a) Lithostratigraphy of gravity core GeoB18530-1 displaying contrast enhanced line scan image, an XRF-based Ca/Sr ratio record, a planktonic $\delta^{18}\text{O}$ record of *N. pachyderma sinistral* and a total light reflectance log. HLs identified by these proxies are highlighted with yellow horizontal bars. (b) Depth-to-age-conversion of the Ca/Sr and $\delta^{18}\text{O}$ records by using ^{14}C -AMS dates (empty triangles) from Max et al. (2022) and by tying HL units to corresponding sections of the NGRIP $\delta^{18}\text{O}$ chronology (Andersen et al., 2006). HL boundary depths and ages (right column) were converted into interval sedimentation rates (left stratigraphic column).

millimeter-thick manganese oxide nodules are ubiquitous alongside sparsely distributed dropstones and shell fragments. The Holocene layer overlies the light grey YD (Figure 3a) showcasing a lower $\delta^{18}\text{O}$, higher Ca/Sr ratio, and larger light reflectance. Underlying the YD layer is a sedimentologically similar section representing the early deglacial phase with slightly darker colors, lower Ca/Sr ratios (Figure 3a) and lower porosities (Figure 1), suggesting a wider grain-size range. Its lower boundary at 560 cm is in sharp contact to the lighter-colored H1 layer.

Compositionally, layers H1 – H6 feature higher lithic and carbonate contents that result in a lighter pigmentation of the beds. The poorly sorted, ~40 cm thick layer H1 is foraminifera-bearing and muddy to very coarse textured with dropstones of up to 5 cm size. The H2 layer has an identical thickness of ~40 cm; like H1, it is also foraminifer-bearing, muddy to sandy textured and poorly sorted with a scanty distribution of mud lenses. Units H3 (~25 cm) and H6 (~50 cm) exhibit a fainter color suggesting lower IRD content than units H1, H2, H4 (~30 cm) and H5 (~50 cm) and show no traces of manganese oxide lenses in contrast to the latter. The intercalated hemipelagic layers I1 – I6 share the sediment characteristics of the deglacial and Holocene facies (Figure 3a). Upper boundaries of HLs with ILs are often more gradual, e.g. I2/H3, I3/H4, I4/H5 and I5/H6.

A previously published ^{14}C -based age model (Max et al., 2022), that dated core GeoB18530-1 down to the lower boundary of H2 (25.4 ka) was extended back to 34.6 ka using two further ^{14}C -AMS dates (Figure 3b). This radiocarbon chronology now covers H1 – H3 within inferred age brackets of 15.3 to 17.3 ka (H1), 23.3 to 25.3 ka (H2) and 27.7 to 32.0 ka (H3) respectively. Ages for the older HLs H4 – H6 were obtained by correlating the Ca/Sr and $\delta^{18}\text{O}$ records to the well-established NGRIP chronology, obtaining age brackets of 37.5 to 39.9 ka (H4), 44.9 to 48.6 ka (H5) and 55.7 to 58.9 ka (H6).

It is well established that HEs had relatively short durations of 1-2 kyr (Bond et al., 1992; Heinrich, 1988) and that their respective sedimentation rates had to be higher than ambient sedimentation to accumulate such expanded HLs as in our core GeoB18530-1. According to our age model, cumulative sedimentation rates were 11- 25 cm/kyr during HEs and just 6 – 8 cm/kyr in between. In the deglacial (post-H1) period, the retreat of the LIS resulted in an intense export of terrestrial sediment and increase in marine productivity. According to our age model of GeoB18530-1, sedimentation rates of the deglacial period averaged to 68.3 cm/kyr before, 49.5 cm/kyr during, and 25.6 cm/kyr after the YD.

2.5 IRD Petrology and Abundance

The central theme of this work is to provide a robust ground on which later provenance studies of IRD can be built on as the bedrock geology of the concerned region is complex and extensive. Our IRD counts and identifications include all obtained IRD particles >1 mm, while the detailed petrographic characterization of the IRD was conducted on coarser IRD particles of 5-20 mm diameter (hereafter referred to as granules). Initially, the petrographic classification scheme of Piper & DeWolfe (2003) was adopted as a guide to identify and sort the various IRD lithologies into groups under a binocular microscope. Physical rock properties like color, hardness, texture etc. were used as the main discerning and classification attributes.

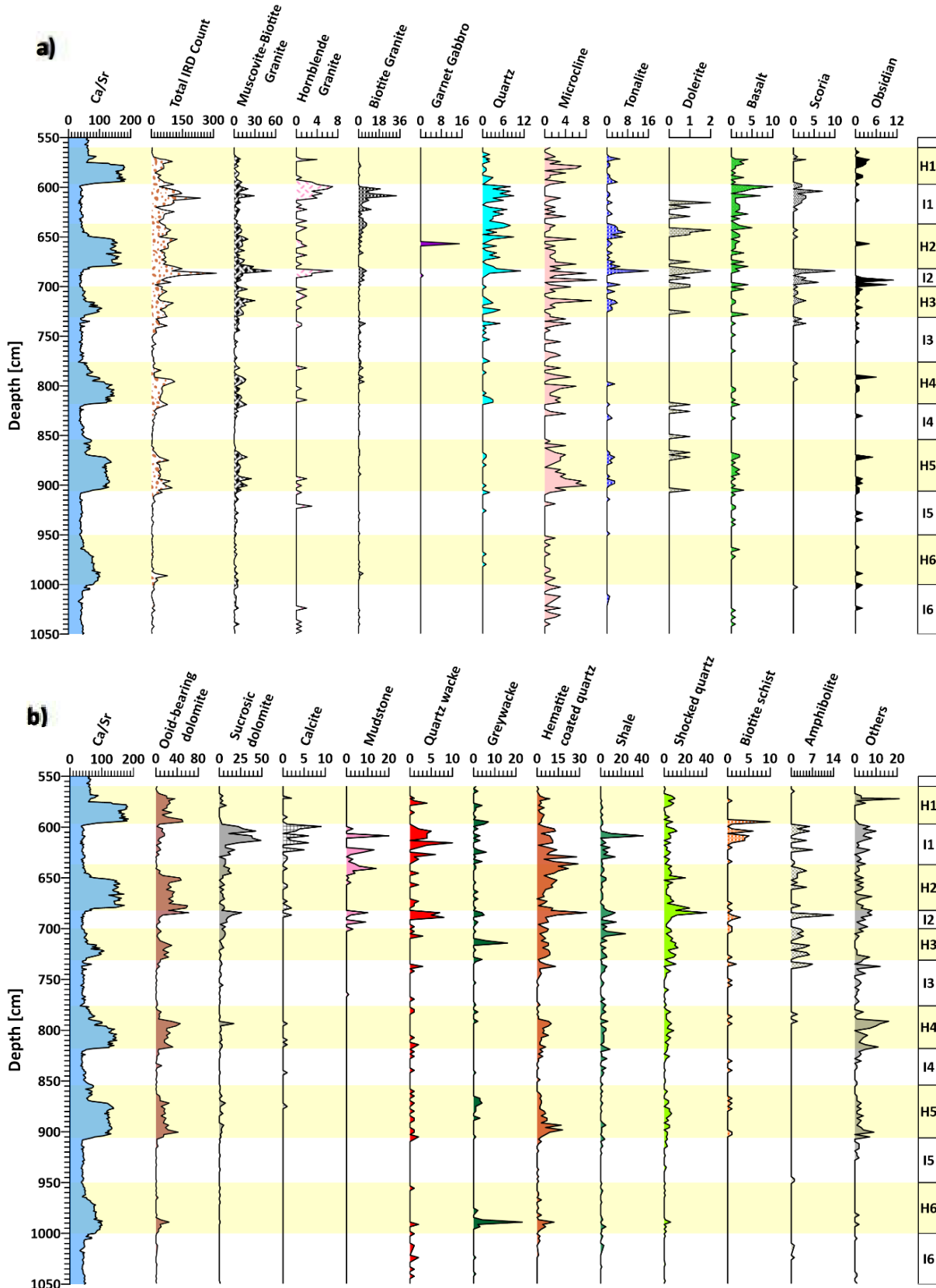


Figure 4: IRD >1 mm particle count records of (a) igneous and (b) sedimentary and metamorphic IRD lithologies showcasing the abundance of individual IRD petrology in the lower (550 -1050cm) stratigraphic sequence of core GeoB18530-1. The yellow horizontal bars highlight the HLs H1 – H6, in between which are the ILs I1 – I5. The Ca/Sr record at left was used as marker of HEs, but does not fully conform to the corresponding ooid-bearing dolomite IRD counts, suggesting that part of the dolomite layers has been current-sorted after ice-rafting.

At first, commonly used descriptive names (tanned dolomite, pink, black and white granites etc.) were assigned to each IRD lithology. These were later replaced by more specific conventional name assignment using mineralogical composition as prefix (minerals 5% and more) in the cases of igneous and metamorphic lithologies. Siliciclastic and carbonate IRD lithologies were named on the basis of classification schemes by Dott (1964), Dunham (1962) and Folk (1959, 1962), respectively. The count record of each identified lithology was registered throughout the lower section of the core (550 – 1050 cm).

IRD particles can be broadly classified into igneous (plutonic and extrusive), sedimentary (siliciclastic and calcareous) and metamorphic rocks, alongside with some individual rock-forming mineral species. These general petrological classes define the framework of the following two subchapters where the specific petrological and stratigraphic characteristics of each IRD lithology are presented. IRD particles are usually intensely weathered, giving the compositional mineral crystals anomalous optic properties in the thin sections. Each IRD lithology classified here has been constituted by several granules of the same characteristic features, while only a few of such representative granules were used in making the petrographic thin section.

The abundance and distribution of each classified IRD particles down the lower section of the core are presented in Figure 4 where each plot axes were scaled to represent the lithological counts befittingly. About 5% of the gleaned IRD particles (415 IRD) were considered as others in that the lithic fragments exhibit no easily identifiable petrologic features.

2.5.1 *Igneous Lithologies*

In the igneous rock category, thin section examination distinguishes several plutonic and volcanic rock types, namely muscovite-biotite granite, hornblende granite, biotite granite, garnet gabbro, quartz, microcline, tonalite, dolerite, basalt, scoria and obsidian, alongside isolated rock-forming minerals. The depositional abundances of these lithologies are given in Figure 4a.

2.5.1.1 *Muscovite-Biotite Granite*

The IRD lithology is typified by coarse-grained holocrystalline lithic fragments of angular to subangular shape commonly referred to as 'black and white granites' in literature (Piper & DeWolfe, 2003). The thin section (Figure 5a) evinces irregularly oriented interlocking crystals (>0.4 mm) of quartz (15 - 35%), plagioclase (15 - 25%), microcline (5 - 15%), biotite (10 – 15%) and muscovite (5 - 10%) as primary minerals and zircon as accessory minerals. Quartz crystals are anhedral with a mottled appearance and display undulose extinction. The albite-twinned euhedral to subhedral plagioclase crystals usually depict evidence of partial or complete sericitisation/saussuritisation. Biotites are euhedral to subhedral in shape with a hue of light to dark brown. They are generally inter-fingering with some crystals revealing minor chloritization (green arrow Figure 5a). Cleavage in biotites is well-defined and included zircons are surrounded by pleochroic halos. Muscovite crystals express a speckled appearance and exhibit second to third-order interference colors. The tiny zircon crystals are found as inclusions in biotites and exhibit a high interference color with some defacements to the biotites. The IRD classified under this grouping constitutes the second most copious out of the 22 different IRD lithologies analyzed in this study. The muscovite-biotite granite count record shows a systematic pattern of deposition where an increased deposition is observed at the

bottom and top (Figure 4a) of each HL except H6. Its abundance is generally lower in the ILs, but it is found throughout the stratigraphic sequence of the core.

2.5.1.2 *Hornblende Granite*

Holocrystalline hornblende granite IRD particles are coarse-grained, angularly shaped lithic fragments referred to as 'pink granites' in literature (Piper & DeWolfe, 2003). IRD petrography (Figure 5b) reveals highly altered, randomly oriented turbid crystals (>0.5 mm) with primary minerals of quartz (20 – 28%), partially to completely altered plagioclase (30 – 35%), hornblende (10 – 15%), and microcline (5 – 12%). Biotite (2 - 5%) and calcite (2 – 5%) make up minor minerals and zircon is an accessory minerals. The anhedral quartz evinces undulose extinction and some show embayed grain boundaries. A few plagioclase show partial sericitisation/ saussuritisation that zones the crystals (original mineral properties are retained in the crystal core, but most of the crystals are completely altered). The microclines limn a tartan twinning with a cross-hatching pattern of 90° angles and some slight alteration marks in some crystals. The pale green to green biotites show perfect cleavage and evidence of intense radioactive damage as highlighted by dark blobs. Veins are filled with crystals of calcite and hornblende consisting of intermittently distributed lenticular crystals of plagioclase as inclusions. The calcites have lenticular shape and display pastel shades of interference colors with rhombohedral cleavage. The dark-rimmed hornblende crystals are pleochroic between pale green and dark green with subtle cleavage and some opaque inclusions. Tiny elongated crystals of zircon show a high interference color with blunt ends. Abundance and distribution of the hornblende granite IRDs are limited and irregular throughout the stratigraphic sequence of the investigated core (GeoB18530-1). However, a significant accumulation was recorded in ILs I1 and I2 (Figure 4a).

2.5.1.3 *Biotite Granite*

This group of lithic IRD fragments comprises downright crystalline grains that are medium to coarse textured with an angular to subangular shape. The few crystals in the thin section slide are murky in appearance and display no preferred orientation (Figure 5c). Primary minerals include quartz (20 - 28%), microcline (30 – 35%), plagioclase (10 – 15%), and biotite (15 – 20%) with an average size of microcline grains being >0.8 mm. 1-2% of the crystals are myrmekitized. Zircon and magnetite are accessory constituents. The anhedral quartz crystals reveal undulose extinction and casually display an embayment. Tartan twinning of the microclines is commonly cross-hatched at an angle of 90°, in a few isolated cases also with oblique angles. Evidence of partial alteration and intergrowth in the microclines is highlighted by multiple tiny striations and wavy-like twinning patterns respectively. Isolated plagioclase crystals manifest evidence of sericitisation/saussuritisation whereas some crystals also show no signs of alteration. The pale green subhedral biotites with perfect cleavage have inclusions of magnetite and zircon. The wart-like exsolved myrmekites are mainly embedded within microcline crystals. Lenticular zircon crystals display large dark rims with high interference colors. Occurrences of IRD of this class are mostly limited to MIS 2 (Figure 4a); comparatively, counts in ILs are higher than in HLs.

2.5.1.4 *Garnet Gabbro*

IRD particles of garnet gabbro are coarse-grained, holocrystalline lithic fragments of subrounded to rounded shape. Crystals are generally massively interlocked and reveal no preferred orientation direction (Figure 5d). Primary minerals are plagioclase (45 – 50%),

clinopyroxene (20 – 25%), garnet (10 – 15%) and biotite (6 – 7%), while quartz (2 – 3%) is just a minor mineral. Most of the plagioclase crystals are traversed by cracks and smeared with tiny blobs as well as striations marking the onset of alteration processes. Clinopyroxenes with

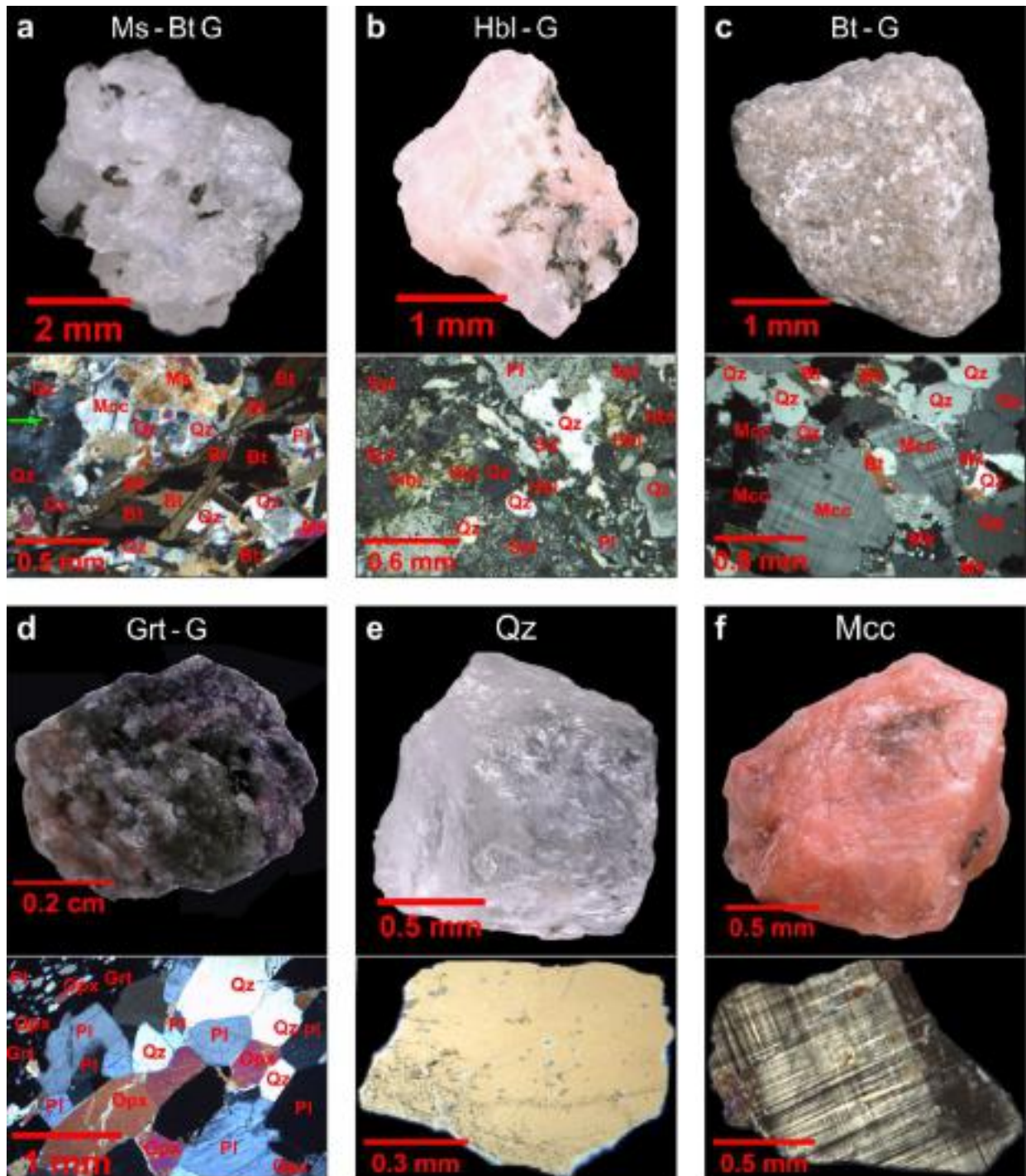


Figure 5: Typical micrograph of IRD >1 mm - representative of igneous lithology showing pristine digital image and thin section of (a) muscovite-biotite granite (Ms-Bt G), (b) hornblende-granite (Hbl-G), (c) biotite-granite (Bt-G), (d) garnet-gabbro (Grt-G), (e) quartz (Qz) and (f) microcline (Mcc). The given mineral acronyms are all in accordance to International Mineralogical Association (IMA) approved format of abbreviation for minerals (Warr, 2021) except myrmekite which is an alteration. The abbreviations are given as follows Qz = quartz, Mcc = microcline, Ms = muscovite, Bt = biotite, Pl = plagioclase, Spl = sericitisation/saussuritisation plagioclase, Hbl = hornblende, Mk = myrmekite, Grt = garnet and Cpx = clino-pyroxene.

orange to purple-like first-order interference colors occur as large isolated crystals as well as tiny lenticular inclusions in garnet. The relatively large garnets (>1 mm) appear as murky crystals with significant fractures and incorporated tiny crystals of clinopyroxene and quartz. The pale brown to brown biotites exhibit perfect cleavage without radioactive burns. Anhedral quartz shows undulose extinction with some speckles that are sparsely distributed in some crystals. In all the recorded IRD counts of different types, garnet-gabbro is the least common component as it is found (Figure 4a) just within H2 and, with a minute occurrence, in the preceding IL I2.

2.5.1.5 Quartz

Individual quartz fragments >1 mm manifest vitreous luster and a subrounded shape (Figure 5e). A section of the crystal appears turbid with some grey blobs distributed across the surface and shows first-order yellow interference color due to improper preparation of the thin section revealed an undulose extinction. The occurrence of the IRD under this classification is rather irregular with a considerable amount recorded within H2 and the IL I1 between H1 and H2 (Figure 4a).

2.5.1.6 Microcline

Individual IRD particles of microcline (Figure 5f) are angularly shaped and display a brick-red hue. Tiny and large cracks traverse across the murky surfaces of the crystals. The tartan twinning cross-hatches at a 90° angle. The record of the commonly occurring microcline IRD is limning a pattern of subtly increasing and decreasing relatively low count frequencies within HLs and ILs except in H5 where it is more pronounced (Figure 4a).

2.5.1.7 Tonalite

Tonalite IRD (Figure 6a) consists of medium-grained, completely crystalline, subangular to subrounded lithic fragments. Most crystals >0.6 mm are randomly aligned except the lenticular biotites that show preferred orientations. The thin section slide reveals primary minerals of quartz (20 – 25%), plagioclase (45 – 50%), orthopyroxene (10 – 12%) and biotite (10 – 13%). Most of the anhedral quartz crystals show no signs of embayment or exsolution and a few isolated crystals appear turbid. Some plagioclases appear murky with multiple broad and well-developed twinning patterns. Some of the twin lamellae are bent due to plastic deformation and a few of the crystals also exhibit zoning as the extinction angle is less for the rim than the core. The slightly pleochroic greenish orthopyroxenes manifest subtle cleavages traversed by several cracks and express purple to sky-blue second-order interference colors. Many of the biotites are aligned depicting a perfect cleavage and pale green to olive green interference colors. Signs of alterations (perhaps to chlorite) are noticeable and a few biotite crystals embed opaque minerals as inclusions. The IRD counts of Tonalite are somewhat intermittent between H1 and H5 limning an increased deposition at the top and bottom of the layers and low to non-deposition in the ILs (Figure 4a).

2.5.1.8 Dolerite

The intensely weathered dolerite IRD is hypocrySTALLINE in texture with angular to subangular shapes. In the thin section (Figure 6b), slabs of crystals (>0.4 mm) are surrounded by a lath of irregularly oriented crystals. Primary minerals are plagioclase (30 – 35%) and large calcite (25 – 30%) veins. Pyroxenes (1 – 2%) represent minor minerals; the remaining minerals (40 – 48%)

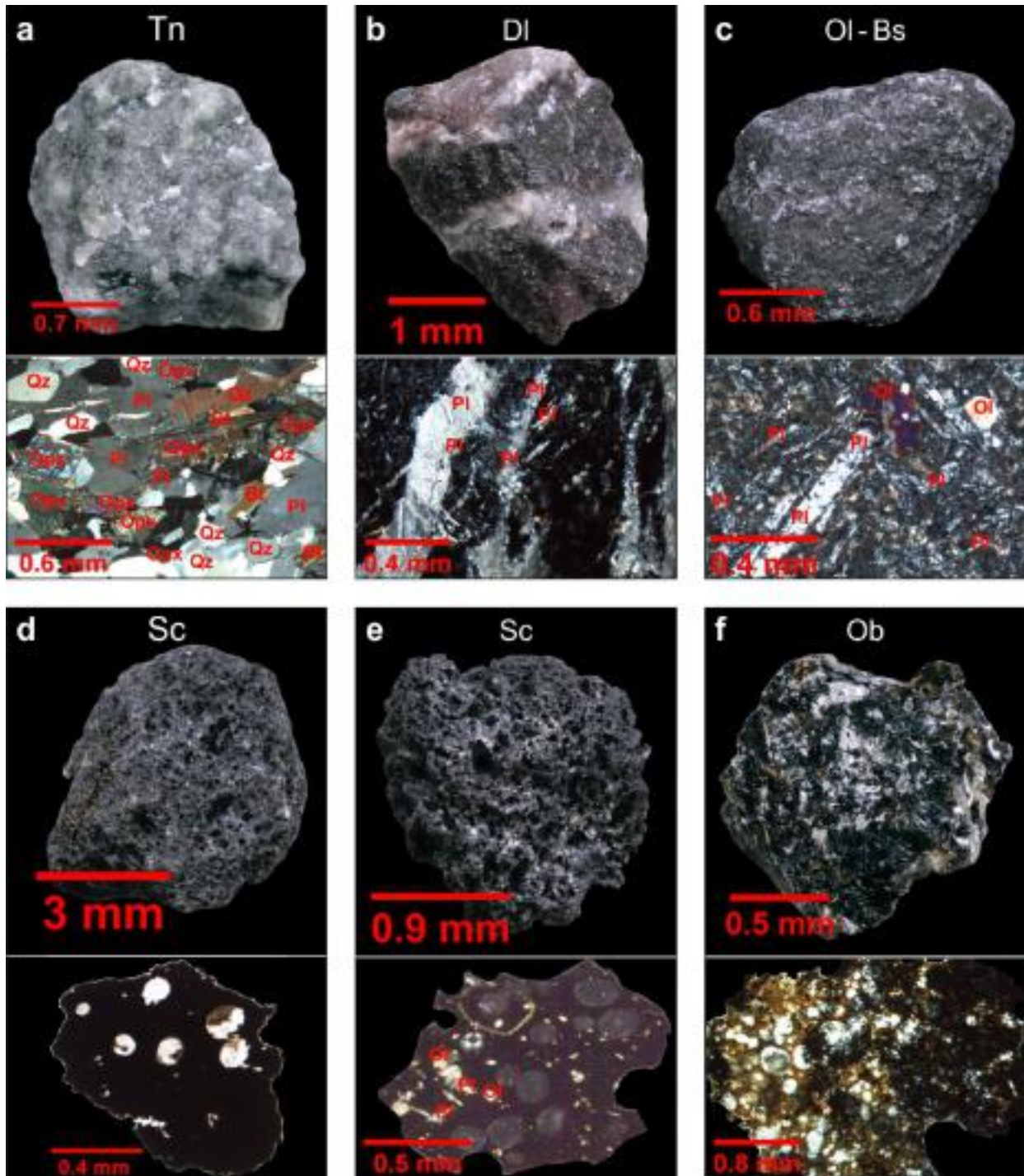


Figure 6: Further IRD >1 mm representatives of igneous lithologies displaying digitized pristine IRD images and thin section. Here the lithologies include (a) Tonalite (Tn), (b) dolerite (DI), (c) olivine-basalt (OI-Bs), (d and e) scoria (Sc), and (f) obsidian (Ob). The constituent mineralogical acronyms are in accordance to IMA (Warr, 2021) Qz = quartz, Opx = orthopyroxene, Pl = plagioclase and Ol = olivine.

are opaque. The plagioclases appear as a lath as well as larger crystals that are sericitized/saussuritized. Calcite crystals occur in veins depicting pastel shades of interference colors and lamellae twinning with no cleavage. The pale green pyroxenes are strongly altered and show no clear zoning or cleavages; they possess a pale yellow low interference color. The deposition of dolerite IRD shows no consistent patterns, but is similar to that of tonalite (Figure 4a).

2.5.1.9 *Olivine-Basalt*

IRD particles of highly altered aphanitic basalts are mainly subangular in shape. The petrographic slide (Figure 6c), depicts a considerable number of dark blobs and randomly oriented slabs (>0.4 mm) of crystals swimming in a microlithic matrix. The IRD consist of plagioclase (45 – 50%) and olivine (15 – 20%) as primary minerals alongside of 25 – 30% opaque minerals. A significant proportion of the plagioclases are laths which surrounds the elongated slabs of plagioclase and olivine crystals. Evidence of sericitisation/saussuritisation in the plagioclase crystals is ubiquitous. The olivine phenocrysts (0.4 – 2 mm) are greatly fractured, partly serpentinized and manifest third-order purple to pale red interference colors. Basaltic IRD counts are inconsistent (Figure 4a) and show no systematic depositional pattern; this lithic fraction is encountered in all the beds.

2.5.1.10 *Scoria*

The dark and highly vesicular IRD clasts of scoria are aphanitic in texture with subrounded to rounded shapes. The thin sections depict sparsely distributed, randomly oriented microlites and vesicles (Figure 6d and e). Due to fast magma cooling in the formation of scoria, about 90 – 95% of the IRD constituents are composed of dark undiscernible material with ~3 – 4% feldspar and ~1% olivine. Plagioclase appears as elongated slabs with a Carlsbad twinning pattern while the olivine crystals of are traversed by cracks and show light blue interference colors. Scoria IRD occurs unsystematically throughout the stratigraphic sequence (Figure 4a).

2.5.1.11 *Obsidian*

The glassy textured obsidians are jet-black in color with subrounded to rounded forms. The thin section slide evinces elongated phenocryst of sanidine (<0.3 mm) embedded within an opaque groundmass (Figure 6f). Well-developed sanidine crystals (~50 – 55%) show Carlsbad twinning and a few cracks in some crystals. Interestingly, the obsidian count record limned a very subtle fashion of distribution in the HLs (Figure 4a), i.e. relatively increased IRD deposition at the bottom and top of each bed. In IL I2, the occurrences of obsidian is significant.

2.5.2 *Sedimentary and Metamorphic Lithologies*

The investigation of the IRD thin section revealed both siliciclastic and carbonate sedimentary rocks besides altered quartz and metamorphic lithologies. The identified rock types include ooid-bearing and sucrosic dolomites, calcite, mudstone, quartz wacke, lithic wacke, hematite-coated quartz, shale, shocked quartz, biotite quartz and amphibolite. The depositional abundances of these lithologies are given in Figure 4b.

2.5.2.1 Ooid-bearing Dolomite

IRD particles of ooid-bearing dolomite are subangular to angular in shape with a conchoidal-like texture; they are usually reported as ‘tan dolostone’ in literature (Piper & DeWolfe, 2003). The thin section slide reveals crystals (<0.6 mm) of dolomite (75 – 80%) and calcite (3 – 5%) as the primary minerals with some ooids (2 – 3%) and a very fine-grained matrix (10 – 12%)

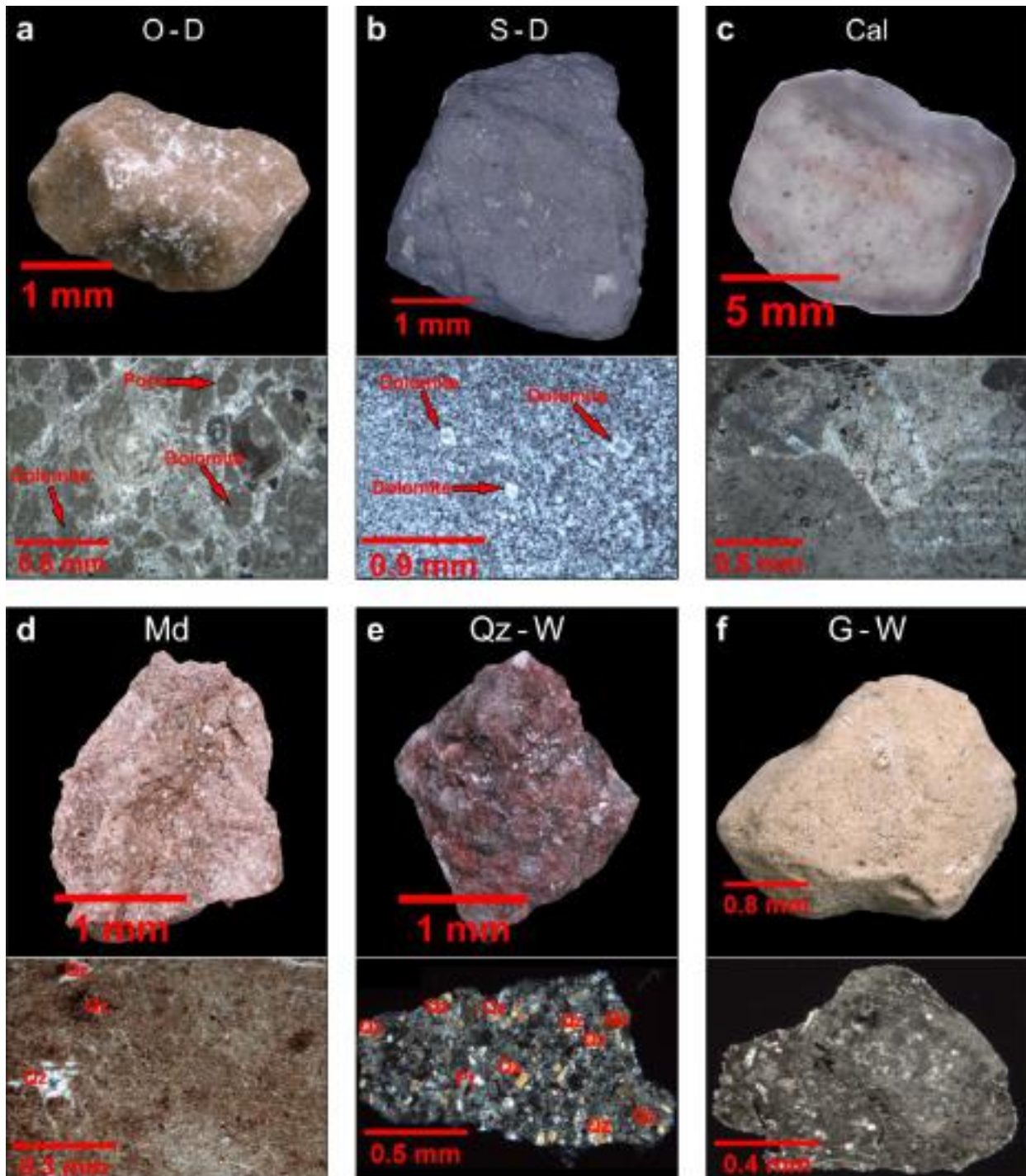


Figure 7: IRD >1 mm micrograph of sedimentary lithologies displaying raw IRD digital images and thin section. **(a)** Ooid-bearing dolomite (O-D), **(b)** sucrosic dolomite (S-D), **(c)** calcite (Cl), **(d)** mudstone (Md), **(e)** quartz wacke (Qw), and **(f)** greywacke (Gw). The mineralogical acronyms are Qz = quartz and Pl = plagioclase adopted in line with IMA (Warr, 2021).

(Figure 7a). The dolomites are ellipsoidal, manifesting zebra-like patterns surrounded by pores filled with clayey-like materials. Evidence of dedolomitization is showcased by calcites which are sparsely distributed in the sample slide. Most of the calcites show pastel shades of interference colors except in some cases where a tinge of grey is observed on stage rotation. The count of ooid-bearing dolomite is the most copious out of all the IRD classes (Figure 4b). It shows a remarkably systematic depositional pattern in all the HLs with higher counts toward their bottom and top, and a very limited abundance in the ILs.

2.5.2.2 *Sucrosic Dolomite*

The greyish medium-grained sucrosic textured IRD is mainly subangular to angular in shape. The petrographic slide shows somewhat parallelogram-shaped crystals (~0.1 mm) in a tiny, clay-like matrix (Figure 7b). Primary minerals are dolomite (75 – 80%), calcite (5 – 10%) and about 5 – 10% of a clayey matrix. The tinged greyish dolomites are subhedral in outline with a mottled appearance. The calcites are presented as micrites with no discernable cleavages and depict dark grey to pastel shades of interference colors. The logged count data document a significant deposition of sucrosic dolomite IRD mainly in ILs (Figure 4b).

2.5.2.3 *Calcite*

IRD made of light-colored crystalline calcite is texturally coarse-grained and has subrounded to bladed shapes. The thin section shows large interlocking crystals of calcite (>0.5 mm) that are commonly referred to as sparry calcite, (90 – 98%) in a dark fluidal groundmass (1 – 2%) (Figure 7c and 8a). The calcite crystals appear mottled with perfect rhombohedral cleavage intersecting each other (Figure 8a). Changes in relief in the crystals during stage rotation indicate high birefringence. Bright pastel shades of interference colors are exhibited in most of the grains. This calcite IRD has a count record somewhat similar to that of sucrosic dolomite (Figure 4b).

2.5.2.4 *Mudstone*

Pinkish fine-grained mudstone clasts are mostly angular in form. The thin section shows pockets of relatively large crystals (<0.3 mm) surrounded by a massive proportion of matrix (Figure 7d). As this IRD consists to more than 75% of matrix and a few quartz fragments, it should be considered as a mudstone based on the classification scheme by Dott (1964). The anhedral quartz grains are cracked and show no evidence of embayment or any form of exsolution. The recorded counts falling into this lithology class (Figure 4b) are rather concentrated in the two late ILs and are not present within HLs.

2.5.2.5 *Quartz Wacke*

Poorly sorted coarse-grained quartz wacke IRD, commonly called 'red sandstone' in literature (Piper and Dewolfe, 2003), is angular to subangular. Chiefly, the petrographic slide (Figure 7e) evinces quartz granules of about 20 – 25% with a supporting matrix (70 – 75%). Some of the quartz crystals express undulose extinction while others show none. Some pale-yellow interference colors are perhaps due to the thickness of the thin section slide. The count record shows irregular occurrences peaking in ILs 1 and 2 (Figure 4b).

2.5.2.6 Greywacke

The beige, poorly sorted, and friable greywacke IRD is subrounded to rounded in shape. The thin section displays a matrix of about 70 – 75% and framework grains of about 20 – 25% (Figure 7f). It is quite subtle to determine the properties of the framework grains; perhaps the brighter fragments might be quartz and/or feldspar. The distribution of greywacke within the stratigraphic sequence is rather irregular (Figure 4b), but falls mainly into HLs.

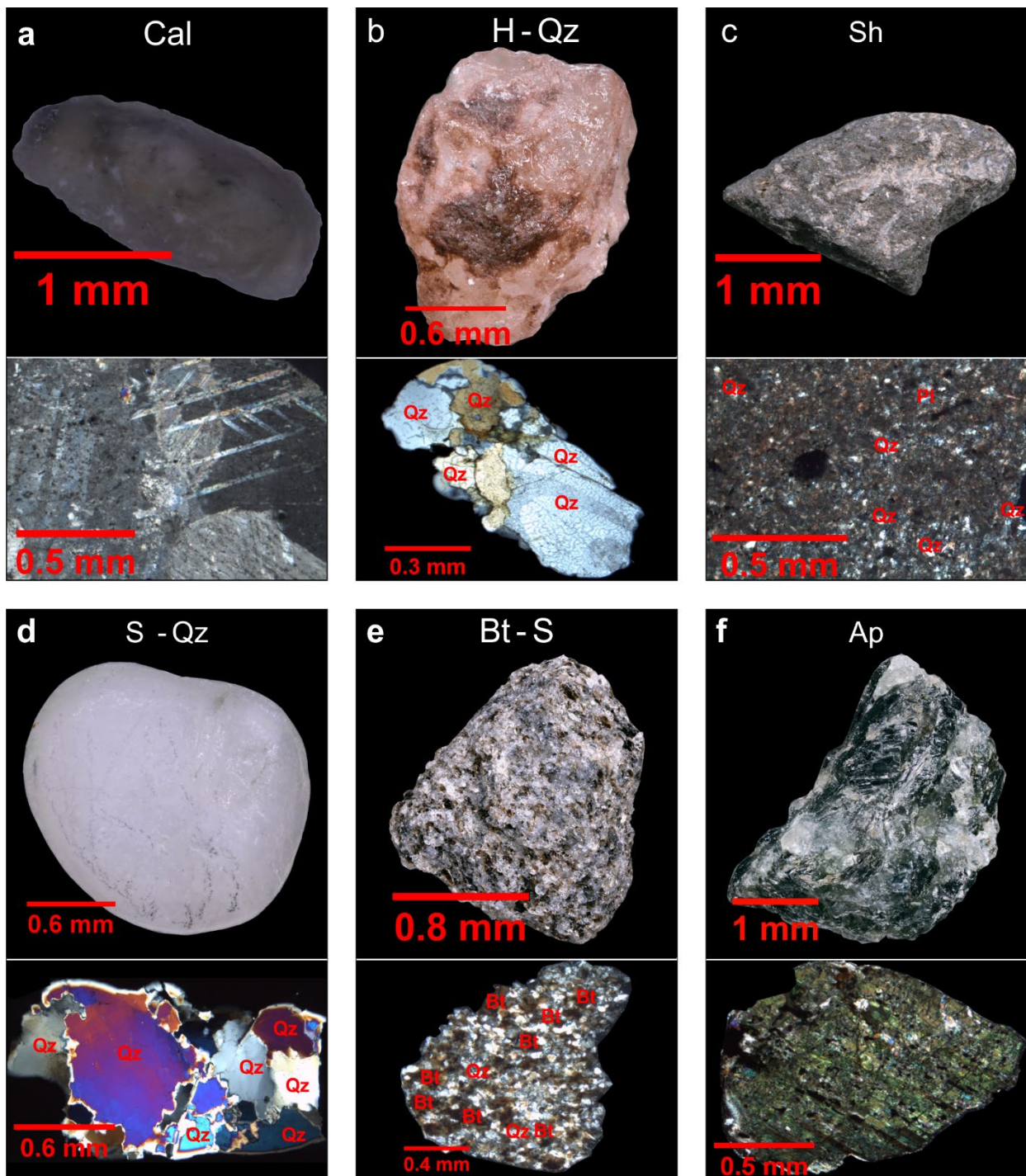


Figure 8: Micrograph of IRD >1 mm – typical representative of sedimentary and metamorphic IRD lithologies. (a) Calcite (Cl), (b) hematite-coated quartz (H-Qz), (c) shale (Sh), (d) shocked quartz (S-Qz), (e) biotite schist (Bt-S), (f) amphibolite (Ap). The respective mineral acronyms are Qz = quartz and Bt = biotite in line with IMA (Warr, 2021).

2.5.2.7 *Hematite-coated Quartz*

Hematite-coated quartz IRD is generally bladed to subrounded in shape. The thin section shows intergrowths of quartz crystals of different sizes with the larger ones being >0.2 mm (Figure 8b). All quartz grains show undulose extinction. Some isolated grains show an interference color of pale yellow perhaps because of a slightly thicker thin section slide. Hematite-coated quartz IRD is regularly distributed in all HLs and also appears in ILs I1 and I2 (Figure 4b).

2.5.2.8 *Shale*

Dark argillaceous shale IRD is chiefly angular in shape. Examination of the thin section slide revealed a gradation of the IRD distribution (Figure 8c) where the relatively larger grains under- or overlie finer ones. The IRD consists of a significant percentage of matrix, some organic matter and quartz. Some sections of the observed samples depict thin laminae consisting of very fine material. The distribution of shale clasts does not follow a particular pattern, but counts in LGM ILs I1 and I2 are higher than in HLs (Figure 4b).

2.5.2.9 *Shocked Quartz*

Frosted-like shocked quartz IRD is overall rounded in shape. In the thin section (Figure 8d), a planar lamellae microstructure highlighting deformation by high-pressure impact is evident. The sample consists of many sub-crystals with purple, blue, pale-yellow and light grey interference colors; all crystals display undulose extinction. The distribution patterns are relatively systematic in that all HLs as well as ILs I1 and I2 reveal an enhanced accumulation (Figure 4b).

2.5.2.10 *Biotite Schist*

The shiny and flaky biotite schist IRD particles are medium-grained textured fragments with subangular shapes. Examination of the thin section (Figure 8e) limned a dark brown banded crystal intercalated by white grains. Biotite (80 – 85%) and quartz (8 – 12%) constitute the primary minerals, sericitized/saussuritized feldspar (2 – 3%) the minor constituent and <1% of the minerals are opaque. The subhedral biotites are well-foliated and possess a brownish hue with no easily distinguishable cleavage; quartz grains are anhedral in shape. Feldspars have undergone sericitisation/saussuritisation as many crystals show intense alteration though some retain puny tartan twinning patterns. The count record of biotite schist IRD (Figure 4b) shows an irregular distribution throughout the core.

2.5.2.11 *Amphibolite*

IRD particles made of crystalline amphibolite are generally angular in shape. The petrographic slide shows foliated and isolated crystals with no discernable outlines (Figure 8f). Amphiboles make the primary mineral (90 – 96%) and quartz (1 - 2%) represents the minor minerals while the remaining constituents (<2%) are opaque. Amphiboles are well-foliated mostly displaying third-order green and purple interference colors. The quartz pockets are intensely altered and show tiny striations and cracks. Amphibolite IRD occurs mainly in HLs and ILs around the LGM (Figure 4b).

2.6 Statistical and Stratigraphic Analyses of IRD Composition and Accumulation

2.6.1 Proportions and Accumulation of IRD Lithologies in HL and IL Units

As Figures 4 and 9a,b evidence, the absolute and relative abundances of the 22 distinguishable IRD lithologies introduced in the previous chapter vary greatly through time, include common as well as rare IRD species, and, for some lithologies, a systematic or preferred affiliation to all or specific HLs or ILs. Some subordinate IRD lithologies (e.g. mudstone, hornblende granite) are entirely absent in certain HLs and ILs, while others (e.g. basalt, shale) are present throughout the entire record, but never in high concentrations. Some IRD species (e.g. ooid-bearing dolomite and muscovite-biotite granite) show systematic variations like a saw-tooth-like pattern at the bottom and top of each HL suggesting a more copious deposition relative to other IRD classes (Figure 4). Such patterns implicate a lithological sequence within HLs, i.e. icebergs laden with detritus from a particular region surge and melt preferentially in particular HE phases.

The unavoidable randomness in spatial distribution and the resulting uncertainty of especially low-numbered IRD species counts makes it hard to see and generalize the “bigger picture” from the stratigraphic record, e.g. from Figure 4. The significance and interpretability of count statistics can be improved by enlarging the bin size, i.e. by cumulating the ~2 cm step IRD counts over larger depth intervals. As HLs and ILs occupy similarly large core depth segments (Figure 3a), these stratigraphic units can serve as larger and meaningful bins for comparison of relative and absolute particle abundance (Figure 9a and b). With ~10 - 20 investigated samples of 10 cm³ volume within each HL and IL unit, every value in Figures 9a,b represents the integral count and analysis of all IRD >1 mm particles in 100-200 cm³ of sediment. The oldest interlayer I6 below H6 has been omitted from the following statistical analyses, as it bears less than 100 particles in total; besides, the absence of a lower age limit prohibits the calculation of particle accumulation rates for I6. With these measures, IRD and iceberg provenance are reflected by the relative proportions of the various IRD lithologies to total IRD (Figure 9a), while the past rate of regional IRD and ice export should scale with the respective IRD accumulation rates (Figure 9b).

The cumulative number of classified and counted IRD particles per unit sample varies from 245 (H6) to 1305 (H2) for HLs and from 123 (I5) to 1591 (I1) for ILs, a sufficiently large classified particle number to pinpoint first-order implications. By averaging the relative contributions (not the count numbers!) to all HLs and to all ILs, we get an impression of the long-term relevance of IRD rock and mineral species (Figure 9c). The ten most common IRD lithologies of HLs are, in falling order of occurrence, ooid-bearing dolomite (37%), muscovite-biotite granite (17%), hematite-coated quartz (10.5%), shocked quartz (8.3%), microcline (4.1%), greywacke (4.0%), shale (3.8%), sucrosic dolomite (3.8%), quartz (1.8%) and basalt (1.6%). These ten lithologies represent 91.6% of the IRD >1 mm particles, while the other twelve less common lithologies compose the residual 8.4%. The ten most abundant IRD lithologies of the ILs (Figure 9c) are muscovite-biotite granite (19%), ooid-bearing dolomite (14%), hematite-coated quartz (10.5%), shale (9.6%), shocked quartz (9.5%), sucrosic dolomite (9.1%), biotite granite (5.1%), microcline (4.2%), amphibolite (2.2%) and quartz (2.2%), totaling to 85.4% of the interlayer IRD particles.

The most striking result of the count statistics (Figure 9c) is the dominant and more than double proportion of ooid-bearing dolomite in HLs compared to ILs (37% vs.14%). This large and well-established increase in dolomitic IRD in the Ruddiman Belt justifiably served as stratigraphic criterion for our initial identification of HLs. Greywacke IRD is much less abundant, but also shows a strong affiliation to HLs (4.0% vs. 1.2%), likewise the rare garnet-gabbro (0.19% vs. 0.02%) that occurs only in layers H2 and I2. These three IRD lithologies are clearly enhanced in HLs and form the “blue HL% > IL% group” in Figure 9c.

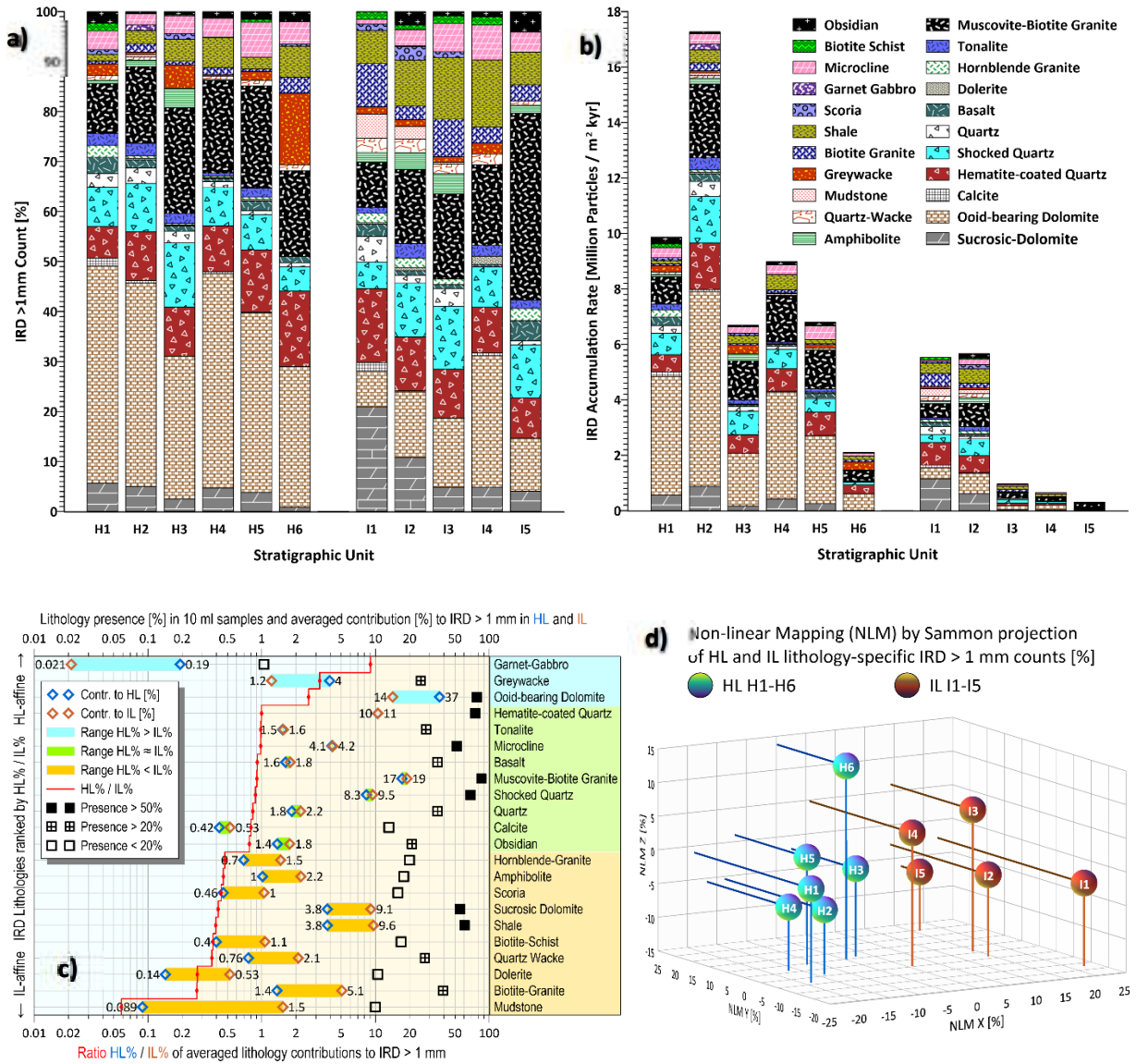


Figure 9: Total lithology-specific IRD > 1 mm particle counts within stratigraphic units H1-H6 and I1-I5, presented as (a) relative percentages of IRD lithologies, and (b) as accumulated IRD particles per area and time. (c) Comparison of averaged HL and IL IRD% counts (blue and brown diamonds) ranked by the magnitude of the HL% / IL% ratio (red line and symbol). Color bars group lithologies that are primarily affiliated to HLs (blue) or ILs (orange), or similarly associated to both (green). Black open, crossed and filled squares denote the observed presence [%] of this IRD lithology within all investigated 10 ml count samples. (d) Non-linear 3D map of the spatial distribution of all HLs and ILs in the 22-dimensional parameter space spanned by the relative proportions of IRD lithologies. The multidimensional downscaling was achieved by Sammon projection (Sammon, 1969) with an appreciably low Sammon stress factor of $\epsilon = 0.0041$.

The second “green HL% \approx IL% group” of IRD lithologies (Figure 9c) contributes almost equally to ILs as to Ls. As their specific accumulation rates scale with the bulk sedimentation rates, their relative proportions to total IRD remain relatively stable throughout all stratigraphic units. Leading among these omnipresent IRD lithologies is muscovite-biotite granite (19% vs. 17%), followed by hematite-coated quartz (10.52% vs. 10.45%), shocked quartz (9.5 vs. 8.3%) and microcline (4.2% vs. 4.1%). Minor IRD lithologies of this group are diorite, basalt, quartz, calcite and obsidian. These lithologies seem to be ice-rafted to the core site equally during as well as between HEs and must be directly affected by the episodic Laurentide ice sheet collapses.

A third “orange HL% < IL% group” of IRD lithologies (Figure 9c) contributes significantly less to HLs than to ILs. The concentration reduction from ILs into HLs is usually by a factor of 2-3. As sedimentation rates typically double during HEs (Chapter 4.1) this reduction factor can be explained by the dilution of background IRD sedimentation by HE-associated sediments. These IRD lithologies are therefore seen as being a part of an ‘ambient glaciomarine sedimentation’ in the study area. Major members of this lithological group are sucrosic dolomite (3.8% vs. 9.1%), shale (3.8% vs. 9.6%) and biotite-granite (1.4% vs. 5.1%). Other such minor constituents are hornblende-granite, amphibolite, scoria, biotite schist, quartz wacke, dolerite, and mudstone.

By multiplying layer-averaged IRD count numbers and sedimentation rates, we obtain lithology-specific IRD particle accumulation rates or ‘IRD rain rates’ (Figure 9b). The strong contrast in IRD particle deposition rates from low values in interim periods to much higher values in HE periods is very apparent in the MIS 3 period (60 – 28 ka), i.e. from H6 until H3. Under the conditions of a less extensive Laurentide ice sheet (Hemming, 2004; Gowan et al., 2021), the glaciomarine sedimentation reaching our core site appears to have been almost exclusively related to HEs, where it attained, most prominently in H5 and H4, IRD accumulation rates almost as high as later during H1. Between these earlier ice shield collapses, IRD accumulation remained rather low. However, we can observe a large increase of interlayer IRD accumulation from I3 to I2, so that onward from I2, at the beginning of the MIS 2 (Hemming, 2004), the IRD deposition remained permanently at a high level to only increase further during H2 (Figure 9b).

With exception of ooid-bearing dolomite and greywacke, the relative proportions of most IRD lithologies (Figure 9a) are largely unaffected by the ups and downs of their accumulation rates (Figure 9b), during MIS 3 as well as during MIS 2. This suggests, that marine calving and iceberg IRD transport from the Northern Canadian ice streams and respective IRD source regions to the Labrador Sea has been continuously active and was only greatly accelerated during HEs. The ratio of continuous (in ILs) over discontinuous (in HLs) IRD export and deposition systematically increased over the observed period from 60 to 15 ka, probably in function of the continent-wide growth and resulting instability of the Laurentide ice sheet from early MIS 3 to MIS 2.

In Figure 9d, the 11 unit-averaged proportions of the 22 IRD lithologies have been used to create a parameter space, in which the relative Euclidean distances of the stratigraphic units depict their petrological similarity or dissimilarity. This spatial configuration has been downscaled into the perceivable third dimension by help of non-linear mapping (Sammon Projection, Sammon 1969). Beyond the good separation of HLs and ILs, one can also observe, that the IRD assemblages of the HLs cluster more densely (i.e. are more geologically constrained) than those of the ILs, which scatter over a wider space. It is also well noticeable that the more productive HEs H5, H4, H2 and H1 are rather similar in composition, while H3 and, even more so, H6 plot

further apart. As Figure 9a documents, unit H6 has an unusually high content of greywacke (14.4%) and unit H3 has uncommonly high amphibolite (3.9%) and shocked quartz (12.8%) contributions. Unit I1 has the most distal and hence dissimilar IRD characteristics because of its very high content of sucrosic dolomite (20.9%), biotite granite (8.6%) and mudstone (4.8%).

2.6.2 Major Factors and Trends of Variance in IRD Lithology

Another diagnostically valuable perspective of count statistics has been obtained by performing a principal component analysis (PCA) of all counted samples (excluding again I6 count records). Prior to PCA, we normalized the (sample) rows of the count matrix to 100% to give equal weight to all IRD assemblages independently of total IRD abundance. Without this measure, the ILs and the earlier HLs with their far lower IRD concentrations would be largely underrepresented in the analysis. Contrary to some PCA practice in geochemistry and petrology (e.g. Miesch, 1976), the (lithology) columns were not (previously) normalized in order to limit the influence of rare and therefore statistically less relevant IRD components. These 'rare lithologies' are typically present in less than 20% of the analyzed samples (Figure 9c). Giving these lithologies ample weight by column normalization introduces non-interpretable random noise to the PCA results and draws attention away from the more relevant IRD lithologies. Following this strategy, the five major of all 22 PC axes, i.e. PC1 - PC5, explain as much as 75.8% of the total data variance, to which they contribute with 27.3%, 20.8%, 11.7%, 8.8% and 7.2%, respectively.

Figure 10a depicts the two most relevant processes that together account for nearly 50% of the lithological variability. The dilution of all other IRD lithologies by the episodically dominant ooid-bearing dolomite fraction at the height of every HE (Figure 4) is represented by the PC1 axis. Assisted by the almost equally dominant muscovite-biotite granite IRD fraction, that stands out in particular at the beginning and end of each HE (Figure 4), but is also common in ILs, both lead IRD lithologies jointly reduce the relative proportions of all those IRD sources that nourish the background IRD deposition. These three non-synchronous IRD fractions span a first-order ternary mixing system, in which the ooid-bearing dolomite and the joint background lithologies clearly separate blue HL and red IL data points, while muscovite-biotite granite admixes in dynamically changing proportions to HLs as well as to ILs and is therefore no useful discriminant.

The replacement of axis PC1 by axis PC3 (Figure 10b) and of axis PC2 by axis PC4 (Figure 10c) changes the perspective at the data variance such that all HL data now cluster at the origin of both axis, while the IL data spread out into triangular, or, taken together, into a tetrahedral distribution. Endmembers of this 'background mixing space' are muscovite-biotite granite, shale, hematite-coated quartz and sucrosic dolomite. Axes PC2 – PC4 delineate temporal changes in background IRD composition that accounts for ~40% of the lithology variance and is therefore even larger than the variance imparted by axis PC1, the 'Heinrich-specific' ooid-bearing dolomite. Figures 4 and 9a clearly show that the contributions of muscovite-biotite granite to ILs decrease through time (maximum in I5), that shale reaches has its peak impact in mid-MIS3 (I4 and I3), and that hematite-coated quartz contributes in a rather constant manner (similar in I5 to I2, more in I1), while sucrosic dolomite experiences an almost exponential increase in the late phase (I2 and I1). These long-term provenance shifts in background IRD sedimentation exceed the compositional changes within the HL units, suggesting that the permanent IRD source provinces have a wider geological and geographical distribution and are

more sensitive to the largescale dimensions and dynamics of the Laurentide ice sheet. This result explains the wider scatter of ILs in Figure 9d.

Figure 10d depicts an episodically higher admixture of microcline (mostly in units H5 and I4) that is largely uncorrelated to the flux changes of other major IRD lithologies (Figure 4). This 'individualistic' behavior of microcline is also shared by other, more spurious, volcanic and metamorphic IRD lithologies (basalt, dolerite, obsidian, scoria, amphibolite, biotite schist, quartz wacke) that are occasionally present (Figure 9c) and appear and disappear in an uncoordinated

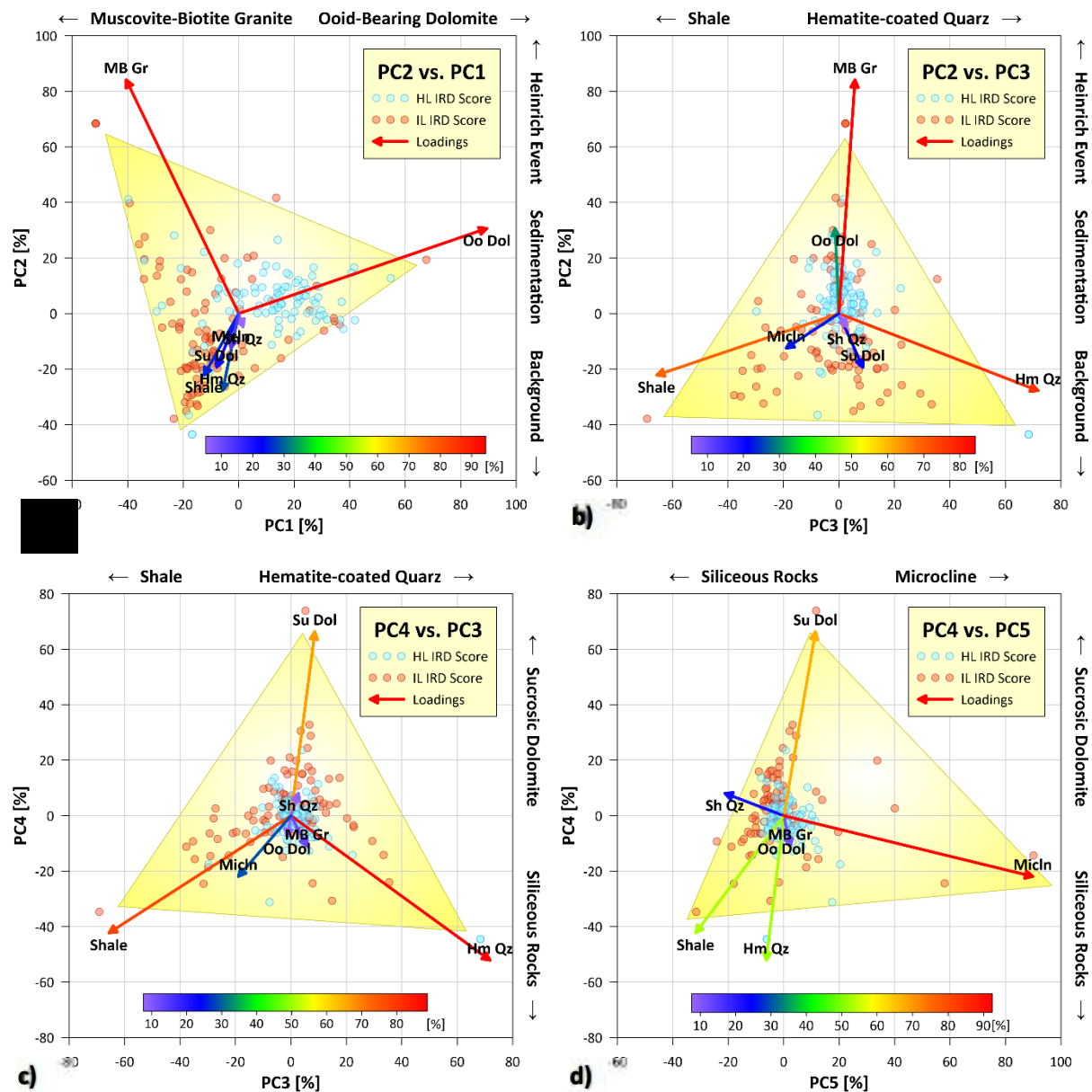


Figure 10: Projection of 192 IRD counts sample from the 22-dimensional row-normalized parameter space onto four indicative planes spanned by the five major principal component axes PC1 to PC5. HL and IL PCA scores are marked in blue and red, while the projections of the count axes (in percentage) of the seven most common IRD lithologies, muscovite-biotite granite (MB Gr), ooid-bearing dolomite (Oo Dol), hematite-coated quartz (He Qz), shocked quartz (Sh Qz), shale (Shale), sucrosic dolomite (Su Dol) and Microcline (Micln), are rainbow-colored according to their projection length in the specific PCA plane (total axis length = 100%). The yellow triangles mark the ternary mixing spaces spanned by the major lithological end-members in each projection plane. All PCA axes have been scaled alike (each axis range equals 160%) for better comparability of the data scatter in each figure.

manner. These largely independent minor IRD lithologies induce ~25% of total variance and dominate the data scatter in the here not depicted projections of higher-order PC axes. These IRD lithologies seem to originate from separate marine calving glaciers draining geological provinces with these more particular and localized rock types. These iceberg and IRD source areas could be distal (Greenland, Canadian Arctic Archipelago), as well as proximal (Labrador, Newfoundland) and would have to be identified by further larger-scale IRD studies.

2.6.3 Stratigraphic Succession and Deposition Rate of IRD Lithologies

As defined by their strong or near-equal affinity to the stratigraphic units of HLs and/or ILs, the three main IRD groups (chapter 6.1) vary considerably in relative abundance (Figure 11a) down the lower section of the sediment core (550 – 1050 cm). The initial group of IRD highlighted in orange-color has a strong presence in all IL units except for the fairly abridged I5. The IRD species of the orange group contribute at least equivalently to the green group within the IL units and exceed it at the top and bottom of I2 and I1 (Figure 11c). The IRD abundance of the second lithology group highlighted in green is virtually proportionate within both HLs and ILs. It can be implied that nearly equal amounts of IRD from these lithologies were deposited during the shorter HE periods and longer periods of IL formation. The third lithology group marked in blue, mainly ooid-bearing dolomite, is prevailing in all HLs, but also forms an ancillary IRD component of all ILs, most prominently of IL4 (Figures 11a-d).

The relative abundance of shale throughout the IL units remains high and fairly systematic with high amplitude variations in a saw-tooth-like pattern except I5, where the record is discontinuous (Figure 11b). Sucrosic dolomite is also similarly concentrated in ILs, but more copious in the late IL units. Both lithologies showcase alternating appearances within some ILs (e.g. I4 and I5). Shocked quartz and hematite-coated quartz have mostly similar concentration patterns throughout the stratigraphic section, but also vary relatively to each other. The abundance of muscovite-biotite granite IRD is high in I5 and relative stable throughout units I1-I4, while its presence in HL units is equally high. As shown earlier, ooid-bearing dolomite is the dominant IRD lithology in all the HLs and appears in a considerable count in the ILs (Figures 11b and d).

2.6.4 Implications for Heinrich Event Chronology

The absolute IRD count logs of the three major IRD lithology groups and of the six major IRD lithologies showcase pronounced twin peaks near the top and bottom of each HL (H1 – H5) with the exception of H6 that only has a single peak. The twin peaks presented in this study concurs and affirms the prediction of Alley & MacAyeal (1994) in that all the HLs should have double-peak structures attributed to the freezing and incorporation of IRD into the glacial ice during HEs. Furthermore, the reports of Bond et al. (1992) and Hodell et al. (2017) suggest that the twin-peaks are manifestation of two stages of iceberg discharge from the Hudson Strait or alternatively, the discharges constitute two independent ice streams. Nevertheless, we infer that the double peaks are likely associated to the dual discharges of icebergs from the Hudson Basin owing to the similar and pronounced doubles peaks observed in the IRD counts of ooid-bearing dolomite that is dominantly found in the Hudson region.

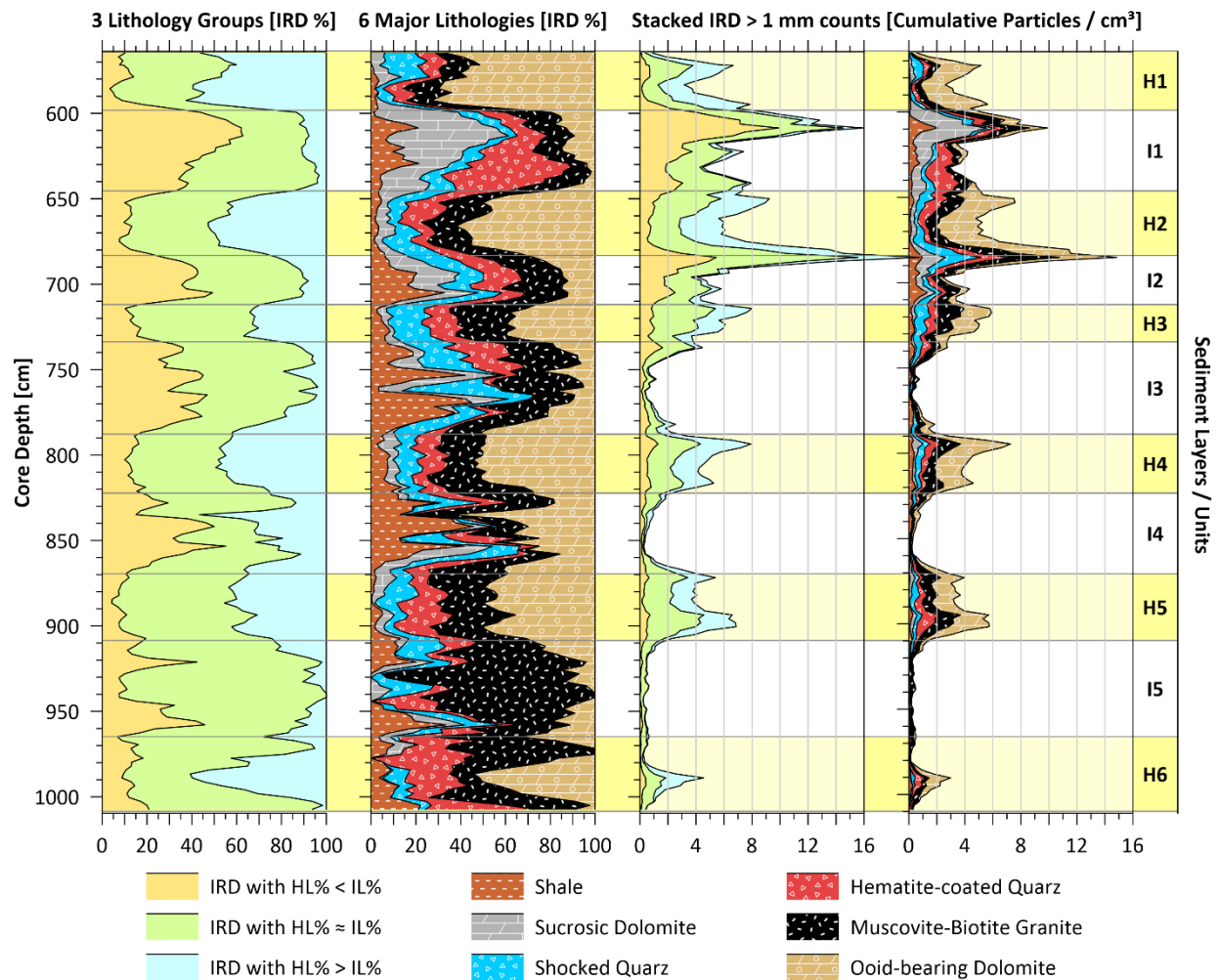


Figure 11: Stacked (a, b) relative and (c, d) absolute abundances of IRD > 1 mm for the (a, c) 3 lithological groups defined in Figure 9c and (b, d) 6 most common lithologies. All shown records were previously smoothed using a weighed (1-2-5-2-1) five-point running mean to remove high-frequency noise. Note that the stacked cumulative IRD counts of the (c) three lithological groups and (d) six major lithologies depict a pattern of increased accumulation near the top and bottom of each HL.

2.7 Conclusions

In Part I of our IRD study, we present the to our knowledge the first detailed petrographic documentation and petrological classification of the coarse grained (>1 mm) IRD in North Atlantic Late Pleistocene sediments. We are aware, that this classification scheme, based on a high-resolution analysis (216 samples) of just one sediment core (GeoB 18530-1) from the SE Grand Banks margin of Newfoundland carries the specific sink characteristics of this site. Therefore further studies from other North Atlantic regions will be necessary to validate and extend this study in the aim to establish a universally applicable scheme for IRD identification.

From a total of 8658 investigated IRD particles (including dropstones), 8243 (> 95%) could be clearly petrologically identified, while 415 (< 5%) were not unequivocally attributable by the available light microscopic means. The therefrom derived grouping scheme comprises 22 IRD lithologies that were defined under the premises, that IRD >1 mm particles must be identifiable only by their physical features under binoculars. This sets limits e.g. to the

distinction of both, microcrystalline or single-crystal IRD particles. For comparability, we provide four color plates with high-quality 3D and thin section micrographs of one typical representative of each class.

In order to establish a more explicit IRD nomenclature, carefully prepared thin sections of several larger specimens from each feature-based IRD class were analyzed by polarized light microscopy. This allowed us to revise the more descriptive nomenclature commonly used in literature with petrological terminology. For example, 'black-and-white granite' has been termed 'muscovite-biotite granite', 'tanned dolomite' is 'oid-bearing dolomite', and 'grey dolomite' is 'sucrosic dolomite'. This measure should be helpful in the search and identification of source rocks in subsequent IRD provenance studies.

The studied gravity core section (550 – 1050 cm) delivers a 5 m long, apparently continuous and undisturbed record the more recent Heinrich Event layers H6 – H1 and their interlayers (I5 – I1) and therefore lends itself to comparative lithostratigraphic purposes. The absolute and relative abundances of the observed IRD lithologies vary substantially and systematically as well within event and interim layers as on the long-term trend over the entire 60 – 15 ka time series. Compositionally, the lithologies of the Heinrich Layers are more similar to each other than their respective interlayers, albeit H3 and H6 were found to distinguish from the petrologically relatively similar Heinrich units H1, H2, H4 and H5. While our study confirms the dominance of the iconic oid-bearing dolomite for the mid-phase of LIS collapses, we could clearly establish the prevalence of muscovite-biotite granite in their early and late phases.

An important outcome of our IRD particle counts is the statistically derived placement of the 22 lithology classes into three well-defined groups based on whether their concentration is higher in event layers, higher in interlayers, or similar in both. This allows us to distinguish IRD lithologies preferentially released by LIS collapses from the 'background IRD' sourced from permanently or more frequently calving Late Wisconsinan ice streams. The abundance of the ten 'background' IRD lithologies decreases by ~50% in Heinrich Layers, which clearly points at their dilution by the Heinrich-related IRD, given that the bulk sedimentation rates from interim to Heinrich Event periods increased from 6 – 8 cm/kyr to 11 – 25 cm/kyr.

With the limitation to (by size and number) petrologically identifiable particles > 1 mm, this first part of our study covered only the very coarse end of the IRD grain-size distribution curve, which can at best be regarded as an estimate for the composition of the entire IRD fraction. In the second part, we will employ, rock magnetic, geochemical, and sedimentological methods to extend the above achieved results to the bulk sediment composition by means of diverse statistical analyses.

The remaining final and most complex aim of this research would be to establish well-supported source-to-sink linkages for all identified IRD lithologies. This task can only be solved in a community effort as it requires similarly detailed IRD studies for complementary sites in the Labrador Sea and greater North Atlantic region, together with a systematic comparison with collections of potential IRD source rocks of the Canadian Shield, the Labrador and West Greenland coasts and possibly even parts of the Canadian Arctic Archipelago.

2.8 Acknowledgements

SB wishes to gratefully acknowledge the financial support enabling his thesis project, composed of a promotion stipend from the Petroleum Technology Development Fund (PTDF), Nigeria, and complementary research funding by the DFG International Research Training Group “Process and impact of climate change in the North Atlantic Ocean and the Canadian Arctic” (ArcTrain, Germany) for travel, consumables and instrument time. We thank the crew and scientific team of RV Maria S. Merian cruise MSM39 for their support during sample acquisition. We owe special thanks to Anne Hübner for making the petrographic thin sections. We also appreciate laboratory assistance rendered by Liane Brück, Christian Hilgenfeldt, Thomas Frederichs and Heike Piero.

2.9 References

- Alley, R. B., & MacAyeal, D. R. (1994). Ice-rafted debris associated with binge/purge oscillations of the Laurentide Ice Sheet. *Paleoceanography*, *9*(4), 503–511. <https://doi.org/10.1029/94PA01008>
- Andersen, K. K., Svensson, A., Johnsen, S. J., Rasmussen, S. O., Bigler, M., Röthlisberger, R., et al. (2006). The Greenland Ice Core Chronology 2005, 15–42ka. Part 1: constructing the time scale. *Quaternary Science Reviews*, *25*(23–24), 3246–3257. <https://doi.org/10.1016/j.quascirev.2006.08.002>
- Andrews, J. T., & Tedesco, K. (1992). Detrital carbonate-rich sediments, northwestern Labrador Sea: Implications for ice-sheet dynamics and iceberg rafting (Heinrich) events in the North Atlantic. *Geology*, *20*(12), 1087. [https://doi.org/10.1130/0091-7613\(1992\)020<1087:DCRSNL>2.3.CO;2](https://doi.org/10.1130/0091-7613(1992)020<1087:DCRSNL>2.3.CO;2)
- Bond, G., Heinrich, H., Broecker, W., Labeyrie, L., McManus, J., Andrews, J., et al. (1992). Evidence for massive discharges of icebergs into the North Atlantic ocean during the last glacial period. *Nature*, *360*(6401), 245–249. <https://doi.org/10.1038/360245a0>
- Bond, G. C., & Lotti, R. (1995). Iceberg Discharges into the North Atlantic on Millennial Time Scales During the Last Glaciation. *Science*, *267*(5200), 1005–1010. <https://doi.org/10.1126/science.267.5200.1005>
- Broecker, W., Bond, G., Klas, M., Clark, E., & McManus, J. (1992). Origin of the northern Atlantic’s Heinrich events. *Climate Dynamics*, *6*(3), 265–273. <https://doi.org/10.1007/BF00193540>
- Channell, J. E. T., & Hodell, D. A. (2013). Magnetic signatures of Heinrich-like detrital layers in the Quaternary of the North Atlantic. *Earth and Planetary Science Letters*, *369–370*, 260–270. <https://doi.org/10.1016/j.epsl.2013.03.034>
- Dalrymple, R. W., LeGresley, E. M., Fader, G. B. J., & Petrie, B. D. (1992). The western Grand Banks of Newfoundland: Transgressive Holocene sedimentation under the combined influence of waves and currents. *Marine Geology*, *105*(1), 95–118. [https://doi.org/10.1016/0025-3227\(92\)90184-J](https://doi.org/10.1016/0025-3227(92)90184-J)
- Dalton, A. S., Margold, M., Stokes, C. R., Tarasov, L., Dyke, A. S., Adams, R. S., et al. (2020). An updated radiocarbon-based ice margin chronology for the last deglaciation of the North

- American Ice Sheet Complex. *Quaternary Science Reviews*, 234, 106223.
<https://doi.org/10.1016/j.quascirev.2020.106223>
- Dott, R. H. (1964). Wacke, graywacke and matrix; what approach to immature sandstone classification? *Journal of Sedimentary Research*, 34(3), 625–632.
<https://doi.org/10.1306/74D71109-2B21-11D7-8648000102C1865D>
- Dowdeswell, J. A., Elverhøi, A., Andrews, J. T., & Hebbeln, D. (1999). Asynchronous deposition of ice-rafted layers in the Nordic seas and North Atlantic Ocean. *Nature*, 400(6742), 348–351. <https://doi.org/10.1038/22510>
- Dunham, R. J. (1962). Classification of Carbonate Rocks According to Depositional Textures, 38, 108–121.
- Dyke, A. S. (2004). An outline of North American deglaciation with emphasis on central and northern Canada. In J. Ehlers & P. L. Gibbard (Eds.), *Developments in Quaternary Sciences* (Vol. 2, pp. 373–424). Elsevier. [https://doi.org/10.1016/S1571-0866\(04\)80209-4](https://doi.org/10.1016/S1571-0866(04)80209-4)
- Folk, R. L. (1959). Practical Petrographic Classification of Limestones1. *AAPG Bulletin*, 43(1), 1–38. <https://doi.org/10.1306/0BDA5C36-16BD-11D7-8645000102C1865D>
- Folk, R. L. (1962). Spectral Subdivision of Limestone Types, 38, 62–84.
- Fulton, R. J., & Prest, V. K. (1987). Introduction: The Laurentide Ice Sheet and its Significance. *Géographie Physique et Quaternaire*, 41(2), 181. <https://doi.org/10.7202/032676ar>
- Grousset, F. E., Pujol, C., Labeyrie, L., Auffret, G., & Boelaert, A. (2000). Were the North Atlantic Heinrich events triggered by the behavior of the European ice sheets?
- Grousset, F. E., Cortijo, E., Huon, S., Hervé, L., Richter, T., Burdloff, D., et al. (2001). Zooming in on Heinrich layers. *Paleoceanography*, 16(3), 240–259.
<https://doi.org/10.1029/2000PA000559>
- Heinrich, H. (1988). Origin and Consequences of Cyclic Ice Rafting in the Northeast Atlantic Ocean During the Past 130,000 Years. *Quaternary Research*, 29(2), 142–152.
[https://doi.org/10.1016/0033-5894\(88\)90057-9](https://doi.org/10.1016/0033-5894(88)90057-9)
- Hemming, S. R. (2004). Heinrich events: Massive late Pleistocene detritus layers of the North Atlantic and their global climate imprint. *Reviews of Geophysics*, 42(1).
<https://doi.org/10.1029/2003RG000128>
- Hesse, R., & Khodabakhsh, S. (2016). Anatomy of Labrador Sea Heinrich layers. *Marine Geology*, 380, 44–66. <https://doi.org/10.1016/j.margeo.2016.05.019>
- Hodell, D. A., Nicholl, J. A., Bontognali, T. R. R., Danino, S., Dorador, J., Dowdeswell, J. A., et al. (2017). Anatomy of Heinrich Layer 1 and its role in the last deglaciation: Heinrich Event 1. *Paleoceanography*, 32(3), 284–303. <https://doi.org/10.1002/2016PA003028>
- Lajeunesse, P., & St-Onge, G. (2008). The subglacial origin of the Lake Agassiz–Ojibway final outburst flood. *Nature Geoscience*, 1(3), 184–188. <https://doi.org/10.1038/ngeo130>
- Leng, W., von Dobeneck, T., Bergmann, F., Just, J., Mulitza, S., Chiessi, C. M., et al. (2018). Sedimentary and rock magnetic signatures and event scenarios of deglacial outburst floods from the Laurentian Channel Ice Stream. *Quaternary Science Reviews*, 186, 27–46.
<https://doi.org/10.1016/j.quascirev.2018.01.016>
- Leng, W., von Dobeneck, T., Just, J., Govin, A., St-Onge, G., & Piper, D. J. W. (2019). Compositional changes in deglacial red mud event beds off the Laurentian Channel reveal

- source mixing, grain-size partitioning and ice retreat. *Quaternary Science Reviews*, 215, 98–115. <https://doi.org/10.1016/j.quascirev.2019.04.031>
- Max, L., Nürnberg, D., Chiessi, C. M., Lenz, M. M., & Mulitza, S. (2022). Subsurface ocean warming preceded Heinrich Events. *Nature Communications*, 13(1), 4217. <https://doi.org/10.1038/s41467-022-31754-x>
- Mosher, D. C., Campbell, D. C., Gardner, J. V., Piper, D. J. W., Chaytor, J. D., & Rebesco, M. (2017). The role of deep-water sedimentary processes in shaping a continental margin: The Northwest Atlantic. *Marine Geology*, 393, 245–259. <https://doi.org/10.1016/j.margeo.2017.08.018>
- Mulitza, S., Bergmann, F., Brück, L., Chiessi, C. M., Govin, A., Klann, M., et al. (2015). *Cruise No. MSM39 - June 07-June 25, 2014 - St. John's (Canada) - St. John's (Canada)*. MARIA S. MERIAN-Berichte (p. 89 pages). DFG-Senatskommission für Ozeanographie, Germany. https://doi.org/10.2312/CR_MSM39
- Naafs, B. D. A., Hefter, J., & Stein, R. (2013). Millennial-scale ice rafting events and Hudson Strait Heinrich(-like) Events during the late Pliocene and Pleistocene: a review. *Quaternary Science Reviews*, 80, 1–28. <https://doi.org/10.1016/j.quascirev.2013.08.014>
- Piper, D. J. W., & DeWolfe, M. (2003). Petrographic evidence from the eastern Canadian margin of shelf-crossing glaciations. *Quaternary International*, 99–100, 99–113. [https://doi.org/10.1016/S1040-6182\(02\)00115-5](https://doi.org/10.1016/S1040-6182(02)00115-5)
- Piper, D. J. W., & Skene, K. I. (1998). Latest Pleistocene ice-rafting events on the Scotian Margin (eastern Canada) and their relationship to Heinrich events. *Paleoceanography*, 13(2), 205–214. <https://doi.org/10.1029/97PA03641>
- Piper, D. J. W., Deptuck, M. E., Mosher, D. C., Clarke, J. E. H., & Migeon, S. (2012). Erosional and Depositional Features of Glacial Meltwater Discharges on the Eastern Canadian Continental Margin. In B. E. Prather, M. E. Deptuck, D. Mohrig, B. V. Hoorn, & R. B. Wynn (Eds.), *Application of the Principles of Seismic Geomorphology to Continental Slope and Base-of-Slope Systems: Case Studies from Sea Floor and Near-Sea Floor Analogues* (Vol. 99, p. 0). SEPM Society for Sedimentary Geology. <https://doi.org/10.2110/pec.12.99.0061>
- Rashid, H., Piper, D. J. W., MacKillop, K., Ouellette, D., Vermooten, M., Muñoz, A., & Jiménez, P. (2019). Dynamics of sediments on a glacially influenced, sediment starved, current-swept continental margin: The SE Grand Banks Slope off Newfoundland. *Marine Geology*, 408, 67–86. <https://doi.org/10.1016/j.margeo.2018.11.012>
- Rashid, H., & Grosjean, E. (2006). Detecting the source of Heinrich layers: An organic geochemical study. *Paleoceanography*, 21(3). <https://doi.org/10.1029/2005PA001240>
- Rashid, H., & Piper, D. J. (2007). The extent of ice on the continental shelf off Hudson Strait during Heinrich events 1-3. *Canadian Journal of Earth Sciences*, 44(11), 1537–1549. <https://doi.org/10.1139/e07-051>
- Rashid, H., Hesse, R., & Piper, D. J. W. (2003). Evidence for an additional Heinrich event between H5 and H6 in the Labrador Sea. *Paleoceanography*, 18(4), n/a-n/a. <https://doi.org/10.1029/2003PA000913>
- Robinson, S. G. (1986). The late Pleistocene palaeoclimatic record of North Atlantic deep-sea sediments revealed by mineral-magnetic measurements. *Physics of the Earth and Planetary Interiors*, 42(1), 22–47. [https://doi.org/10.1016/S0031-9201\(86\)80006-1](https://doi.org/10.1016/S0031-9201(86)80006-1)

- Robinson, S. G. (1993). Lithostratigraphic applications for magnetic susceptibility logging of deep-sea sediment cores: examples from ODP Leg 115. *Geological Society, London, Special Publications*, 70(1), 65–98. <https://doi.org/10.1144/GSL.SP.1993.070.01.06>
- Robinson, S. G., Maslin, M. A., & McCave, I. N. (1995). Magnetic susceptibility variations in Upper Pleistocene deep-sea sediments of the NE Atlantic: Implications for ice rafting and paleocirculation at the Last Glacial Maximum. *Paleoceanography*, 10(2), 221–250. <https://doi.org/10.1029/94PA02683>
- Ruddiman, W. F. (1977). Late Quaternary deposition of ice-rafted sand in the subpolar North Atlantic (lat 40° to 65°N). *GSA Bulletin*, 88(12), 1813–1827. [https://doi.org/10.1130/0016-7606\(1977\)88<1813:LQDOIS>2.0.CO;2](https://doi.org/10.1130/0016-7606(1977)88<1813:LQDOIS>2.0.CO;2)
- Sammon, J. W. (1969). A Nonlinear Mapping for Data Structure Analysis. *IEEE Transactions on Computers*, C-18(5), 401–409. <https://doi.org/10.1109/T-C.1969.222678>
- Shaw, J., Piper, D. J. W., Fader, G. B. J., King, E. L., Todd, B. J., Bell, T., et al. (2006). A conceptual model of the deglaciation of Atlantic Canada. *Quaternary Science Reviews*, 25(17), 2059–2081. <https://doi.org/10.1016/j.quascirev.2006.03.002>
- Simon, Q., Hillaire-Marcel, C., St-Onge, G., & Andrews, J. T. (2014). North-eastern Laurentide, western Greenland and southern Inuitian ice stream dynamics during the last glacial cycle: Ice stream dynamics in Baffin Bay. *Journal of Quaternary Science*, 29(1), 14–26. <https://doi.org/10.1002/jqs.2648>
- Stoner, J. S., Channell, J. E. T., Hillaire-Marcel, C., & Mareschal, J.-C. (1994). High-resolution rock magnetic study of a Late Pleistocene core from the Labrador Sea. *Canadian Journal of Earth Sciences*, 31(1), 104–114. <https://doi.org/10.1139/e94-009>
- Stoner, J. S., Channell, J. E. T., & Hillaire-Marcel, C. (1996). The magnetic signature of rapidly deposited detrital layers from the Deep Labrador Sea: Relationship to North Atlantic Heinrich layers. *Paleoceanography*, 11(3), 309–325. <https://doi.org/10.1029/96PA00583>
- Tucholke, B. E., & Sibuet, J.-C. (2006). Leg 210 synthesis: Tectonic, magmatic, and sedimentary evolution of the Newfoundland-Iberia rift. *Proceedings of the Ocean Drilling Program: Scientific Results*, 210p.
- Warr, L. N. (2021). IMA–CNMNC approved mineral symbols. *Mineralogical Magazine*, 85(3), 291–320. <https://doi.org/10.1180/mgm.2021.43>

Chapter 3: Ice-Rafted Detritus (IRD) of the SE Grand Banks Slope, Newfoundland, Throughout Heinrich Layers 1 to 6 - Part II: Magnetic Properties

S. Bukar^{1*}, T. von Dobeneck^{1,2}, Y. Wang¹, L. Max¹, T. Frederichs¹, E. Dallanave¹, G. St-Onge³

¹ Faculty of Geosciences, University of Bremen, Bremen, Germany

² MARUM-Center for Marine Environmental Sciences

³ Institut Sciences de la mer de Rimouski ISMER, Canada Research Chair in Marine Geology, Université du Québec à Rimouski and GEOTOP, Canada

Abstract

A prominent signature of episodic late Pleistocene Laurentide Ice Sheet collapses are ocean-wide ‘Heinrich Event’ layers of dolomitic (and hence low-magnetic) ice-rafted detritus (IRD) of the Hudson Bay area. Counterintuitively, most Heinrich Layers are magnetically enhanced and identified as maxima in magnetic susceptibility (MS) logs. Building on the IRD petrology and count statistics at Newfoundland’s SE Grand Banks Slope of Part I, Part II now presents bulk rock magnetic, element and sedimentological data of core GeoB 18530-1 and mineral magnetic analyses of 22 classified IRD species. By stratigraphically and statistically comparing bulk sediment properties, IRD counts and IRD magnetic property data, we investigate, how ferri- and diamagnetic components of IRD and of glaciomarine background sedimentation jointly control the MS record. A critical issue in this quest is, how to infer from the relatively minor effect of the identifiable coarse IRD fractions to the larger impact of the unquantifiable, unclassifiable and magnetically enriched fine IRD fraction. High correlations and conforming signal patterns of IRM_{20mT} and MS evince, that magnetically soft MD magnetite originating from plutonic Canadian Shield rocks, mostly muscovite-biotite granite, dominate MS records. As indicators of dolomitic and granitic influx, the element ratios Ca/Sr and K/Fe delineate that the MS enhancement by the very magnetic granitic detritus was diluted and partly compensated by co-deposited dolomitic detritus. The misfit of the MS record with IRD-count based models suggests, that glaciomarine detritus reached the core site not just as rain-out from icebergs, but also by advective or gravitational suspension transport.

Key Points:

- Magnetic susceptibility maxima of ice-rafted detritus (IRD) rich layers in the NW Atlantic sediments are engendered by coarse magnetite of granitic origin
- Weakly magnetic dolomite IRD dilutes the concentration of highly magnetic granite IRD, partially diminishing its susceptibility.
- Low correlation of IRD counts with rock magnetic records suggest that the latter is equally sensitive to ice-rafted as to advective detrital fluxes.

3.1 Introduction

Episodic massive glacial surges of sediment-laden icebergs from the Laurentide Ice Sheet (LIS) into the North Atlantic Ocean (NAO), so-called 'Heinrich Events' (HEs; Broecker et al., 1992), formed ocean-wide ice-rafted detritus (IRD) rich marker horizons termed 'Heinrich Layers' (HLs; Heinrich, 1988; Bond et al., 1992) within the 46°-50°N latitude range ('Ruddiman Belt'; (Ruddiman, 1977)). The most abundant and emblematic IRD lithology associated with HLs is ooid-bearing dolomite from the North Canadian Hudson Bay region (Andrews & Tedesco, 1992; Piper & DeWolfe, 2003; Stoner et al., 1996) and Chapter 2). However, as detailed e.g. by Piper & DeWolfe (2003) and Chapter 2, the petrology of North Atlantic IRD is extremely diverse and varies between and across individual HLs, resulting from the specific course and geographical reach of each LIS collapse.

The preceding Part I study of Bukar et al. (Chapter 2) was based on a high-accumulation sediment record from the Newfoundland Southeast Grand Banks Slope (Core GeoB18530-1, Mülitz et al., 2015) where 22 distinct IRD lithologies were identified and described microscopically including the determination of their specific abundance (count record) and association throughout the six HLs (H1-H6) and all of their enclosing sediment interlayers (ILs) from 57 to 14 ka, i.e. during Marine Isotope Stages MIS 3 and MIS 2. The high-resolution counts of IRD particles >1 mm revealed that certain IRD lithologies accumulated primarily during the early, mid or late phases of HE. In contrast, others are associated with glaciomarine background sedimentation in the north-western North Atlantic, to which not just the inner LIS provenances, but also sea-calving glaciers of Western Greenland, the Canadian Arctic, the Labrador Coast and the Gulf of St. Lawrence may have contributed. To facilitate IRD-based reconstructions of past ice-sheet dynamics, automated IRD particle fingerprinting based on e.g. geochemical, rock magnetic, crystallographic, spectrometric and radiometric methods would be desirable.

For several decades, rock magnetic analyses have been successfully employed to identify and stratigraphically correlate IRD-rich layers in North Atlantic sediments (Peters et al., 2008; Robinson, 1986; Robinson et al., 1995; Stoner et al., 1996, Rashid et al., 2003, 2012). Many studies on HLs use records of magnetic susceptibility (MS), the most integral and also most easily and rapidly measurable rock magnetic parameter. More selective magnetic parameters such as isothermal remanent magnetization (IRM) and anhysteretic remanent magnetization (ARM) were also frequently measured to identify the magnetic minerals and their grain sizes in HL sediments (Bond & Lotti, 1995; Peters et al., 2008; Robinson et al., 1995; Stoner et al., 1996). Limitations of these approaches arise from the magnetic similarity of many rock types and the predominance of magmatic IRD lithologies over the magnetic signal of sedimentary lithologies due to their orders of magnitude higher magnetic moments (Bond & Lotti, 1995; Channell & Hodell, 2013; Stoner et al., 1996).

Peters et al. (2008) combined a wide range of rock magnetic measurements to assess potential IRD sources of Core MD95-2006 from the Hebridian continental slope, the eastern terminus of the Ruddiman Belt. During past glacial periods, IRD deposited at this study site came not just from the distal LIS, but also from the closer British (BIS), Icelandic (IIS), Fennoscandian (FIS) and Greenland (GIS) ice sheets, greatly complicating its identification and interpretation.

In a similar environmental magnetic study of four sediment cores from the SW Grand Banks Slope, (Leng et al., 2018, 2019) investigated the magnetic properties and major elements of silt-sized plumite sediments formed by subglacial outburst floods emerging from the LIS through the proximal Laurentian Channel. Three geological provinces of Eastern Canada (Appalachian red beds, Anticosti carbonates, Canadian Shield granites) were identified as the main source areas of the five plumite beds by numerical mixing of terrestrial reference data.

All previously mentioned studies agree that North Atlantic IRD-rich layers are associated with MS maxima (e.g. Grousset et al., 1993). Marine sediments at these latitudes are largely composed of terrigenous, siliciclastic materials and thus have rather high background MS. An addition of ice-rafted detrital carbonate and quartz, both low- and diamagnetic materials, should have therefore reduced rather than increased bulk MS. Since this is not observed, the undeniable magnetic dilution effect by the diamagnetic IRD fractions must be overcompensated by one or several highly ferrimagnetic IRD lithologies, whose magnetic mineral content exceeds that of all other IRD and background sediment components. As obvious as this explanation may seem, it has, to our knowledge, not yet been analytically investigated and validated.

Unlike the more difficult inverse problem of identifying and quantifying IRD components from bulk rock magnetic properties (), forward modeling the cumulative MS of petrologically classified IRD mixtures with lithology-specific rock magnetic property data seems to be mathematically straight-forward at first glance: The composite mass susceptibility χ of a mixture of n distinguishable uniform rock, mineral or even fluid components i ($1 \leq i \leq n$) with known mass fractions c_i ($0 \leq c_i \leq 1$; $\sum c_i = 1$) and specific susceptibilities χ_i is given by

$$\chi = \sum_{i=1}^n c_i * \chi_i \quad (\text{Equation 1})$$

Analog linear mixing equations apply for concentration-dependent remanent magnetization parameters as long as magnetic particle contents are low and their interactions negligible.

In practice, this approach bears uncertainties: the magnetic iron minerals of most parent rocks have very fine crystal sizes (0.01-10 μm) and only appear in the >1 mm IRD sieve fraction as tiny enclosures in mono- and polymineralic lithic particles. Like glaciomarine diamictos (Domack & Powell, 2018), ice-rafted glaciogenic particles cover a wide grain-size range spanning from gravel and sand down to silt and even clay size. The finer IRD particles overlap inseparably with the gradation of (hemi-)pelagic background sediment. IRD particles in the 125 μm -1 mm range are often monocrystalline or too small to be petrologically classified and also too numerous for individual particle counting (Chapter 2). Statistical or budgetary estimates may permit extrapolating the count or weight data of the IRD >1 mm sieve fraction to the associated and probably magnetically far more relevant finer IRD fractions.

Further uncertainty arises from the wide petromagnetic variability of virtually every magmatic, metamorphic and sedimentary rock type. The magnetic properties of most rocks depend critically on their specific formation conditions and alteration state. Tabulated MS values of rocks (e.g. Telford et al., 1990) often span 2-3 orders of magnitude for a specific lithology. Site-specific magnetic property data of extracted and petrologically classified IRD particles are therefore needed to create valid magnetic IRD mixing models, but are so far unavailable.

With these issues to solve, this second part of our IRD study investigate the rock magnetic, geochemical and sedimentological properties of glacial SE Grand Banks sediments and magnetically characterizes all observed IRD components. Building on the petrological IRD classification and counts of the first part (Chapter 2), we address the following questions:

1. How do observed IRD lithologies compare in terms of their magnetic properties?
2. Which IRD lithologies exert a significant, positive or negative impact on bulk magnetic properties of the glaciomarine sediment, in particular their MS record?
3. Which other, non-magnetic bulk sediment properties assess IRD content and lithology and how can these help to explain the MS signal
4. How well can bulk magnetic properties be modelled from bulk sediment parameters and classified IRD counts and what does this tell us about IRD grain-size distribution?

3.2 Materials and Methods

3.2.1 Materials

The data and rock magnetic investigation presented here were conducted on the gravity core GeoB18530-1 (42° 50.37' N, 49° 14.09' W, 1888 m water depth) sediment, retrieved from the foot of the Southeast Grand Banks Slope of Newfoundland during the RV Maria S. Merian cruise MSM39 (Mulitza et al., 2015). Part I of our study (Chapter 2) describes the geology of the study area, potential IRD source areas, the stratigraphy and age model of core GeoB18530-1, and the abundance and petrology of IRD granules >1 mm.

Parallel syringe and cube sample series, each counting 216 specimens, were collected at identical positions in 2.3 cm steps throughout the 550 - 1050 cm core section corresponding to MIS 3 and 2. The 10 cm³ syringe sample set was used to extract the >125 µm fraction (foraminifera and fine IRD) and >1 mm fraction (coarse IRD for petrological and rock magnetic classification). Oriented 6.2 cm³ cube samples were taken for non-destructive paleo- and rock magnetic measurements. We additionally collected and pooled five adjacent syringe samples from each of the layers HL1, IL1 and HL2 for wet-sieve fractionation.

3.2.2 Methods

3.2.2.1 Magnetic Susceptibility

The shipboard whole-core volume susceptibility κ log presented in Part I is now accompanied by a high-resolution sample-based MS record measured with a *Bartington* MS3 susceptometer with a MS2B bulk sample sensor (κ_f : 440). Dry bulk mass susceptibility χ was acquired by converting κ_f with the known dry weight of each sample cube. The more sensitive *Agico KLY-2 KappaBridge* susceptometer with 920 Hz operating frequency, always set to the most sensitive applicable range, was used to determine mass susceptibility χ of the 216 unclassified coarse (>1 mm) IRD sieve fractions and 22 classified IRD lithologies (see Chapter 2).

To ensure proper representation and precise values for some very weakly magnetic IRD lithologies, we measured either a single large IRD granule ('dropstone') or combined several classified and picked IRD particles of identical lithology, if necessary merging particles from

several syringe samples. Depending on material availability, these classified IRD particle samples had masses from 26 mg (obsidian) to 2700 mg (muscovite-biotite granite) and bulk particle volumes from ~ 10 to 1000 mm^3 . Pooled particles were jointly weighed, placed into non-magnetic thin-walled pharmaceutical capsules and inserted into the MS sensor space inside a plastic drinking straw. With multiple measurements, sample holder correction and sample mass normalization, these IRD measurements have an estimated accuracy of $\sim 1 \cdot 10^{-9} \text{ m}^3/\text{kg}$.

3.2.2.2 *Remanent Magnetization*

The automated *2G Enterprises 755R* DC-SQUID magnetometer of the Bremen Paleomagnetic Laboratory (Mullender et al., 2016) was used to measure anhysteretic remanent magnetization (ARM) and stepwise acquisition of isothermal remanent magnetization (IRM). All samples were first demagnetized in alternating fields (AF) of 180 mT along their X-, Y-, and Z-axes to remove pre-existing remanent magnetizations. ARM was acquired in a 100 mT alternating field (AF) and 40 μT bias field. IRM was imparted in 28 pulse field steps from 10 mT to 2700 mT (internal pulser up to 700 mT, external pulser up to 2700 mT). The preset pulse field values were replaced by the true peak field obtained from a built-in induction sense coil. Mass-specific IRM curves were measured for all bulk sediment cube samples, corresponding $>1 \text{ mm}$ IRD fractions, and all 22 classified IRD lithologies. As ARM of some IRD samples would have been too weak to be correctly measured, ARM values were only obtained for the bulk samples.

To stabilize the loose IRD particles during measurements, they were attached to polypropylene-based sticky tape and inserted into tiny 3D-printed cup-like holders, which could be positioned in the center of the sample cubes. Larger IRD fractions were split into two or more cups and measured separately after which their magnetizations were added. For IRM acquisition curves fitting the online software MAX UnMix (Maxbauer et al., 2016), which is based on skewed generalized Gaussian functions (Egli, 2003).

3.3 Magnetic, Geochemical and Sedimentological Bulk Sediment Properties

We also compiled and reanalyzed some already existing unpublished bulk sediment data of core GeoB18530-1 and compare them here in their stratigraphic context. Rock magnetic parameter records were measured by Wang (2016) to detect the impact of HEs on the magnetic mineral assemblage. With 2.3 cm sample spacing throughout the lower section of the core (550 – 1050 cm), these records resolve short-range variability and reflect HE chronology as well as the stochastic spatial distribution of larger IRD particles. All mathematically related bulk rock magnetic data are from the same cube sample set; hence the randomness of IRD distribution will not affect bivariate statistics as much as with separate sample volumes. When we relate magnetic data to XRF core-scan data (Max et al., 2022) and to lithology-specific IRD counts (Chapter 2), whose core depths conform, but sample volumes diverge, random IRD content is bound to introduce further uncertainty.

3.3.1 *Rock Magnetic Bulk Sediment Records*

Geological interpretation of MS is not nearly as simple as its measurement, since practically all sediment components, whether ferri-, para- or diamagnetic, contribute to this integrative induced magnetization parameter. To find out, which magnetic minerals and particle sizes

control MS variability, we compared the MS to selective remanent magnetizations that were obtained in different laboratory magnetic fields (Figure 1). The chosen parameters IRM_{20mT} , $IRM_{100mT} - IRM_{20mT}$ and ARM_{100mT} (where subscript numbers indicate the acquisition fields) aim at grain-size dependent ferrimagnetic domain states; IRM_{300mT} and $HIRM_{2700mT-300mT}$ distinguish ferri- and antiferromagnetic mineral fractions. The latter are termed as magnetite and hematite (*in sensu lato*) in the following as these are the two most common magnetic mineral candidates under oxic marine sediment conditions, and thus the most likely minerals.

The cube sample-based susceptibility χ record (orange curve in Figure 1a) is overlaid by the full-core log of volume susceptibility κ (blue), where the sensor volume of $\sim 1000 \text{ cm}^3$ acts as low-pass filter. The sample-based MS record is therefore much spikier than the full-core record, but both patterns largely conform. In both records, MS is discernably higher in HLs (mean: $8.9 \times 10^{-7} \text{ m}^3/\text{kg}$) than in ILs (mean: $7.7 \times 10^{-7} \text{ m}^3/\text{kg}$). Our introductory remarks on ‘HE peaks’ therefore holds for this record. The highest MS peak values of 12 and $14 \times 10^{-7} \text{ m}^3/\text{kg}$ are observed in H4 and H5. As pure magnetite has a MS of $\chi_{Mag} = 5 \times 10^{-4} \text{ m}^3/\text{kg}$, such apparently small numbers imply relatively high sedimentary magnetite contents of 0.1-0.3 wt%.

Given that IRM_{20mT} (Figure 1b) is a measure of magnetically soft ‘multi-domain’ (MD) magnetite content, the high similarity with MS, including single-sample spikes, signalizes, that a rather coarse ($>10 \mu\text{m}$) magnetite fraction, commonly found in igneous and metamorphic rocks, is a first-rank MS driver. The scatterplot of χ vs. IRM_{20mT} (Figure 1h) indicates a highly significant signal correlation, where Pearson’s r for HLs (0.82) exceeds that for ILs (0.61). The regression line for HLs intercepts the ordinate near the origin of the scatterplot underlining the dominant role of this magnetic fraction. The magnetogranulometric parameter $SIRM/\chi$ (Figures 1f,m) evidences that every MS increase is paralleled by magnetite coarsening, within ILs even more than within HLs, where the magnetite fraction is altogether coarser.

Magnetite of finer crystal size (and thus fewer magnetic domains) requires higher fields to be remagnetized; the $IRM_{100mT} - IRM_{20mT}$ record (Figure 1c) thus quantifies submicron magnetite crystals ($\sim 0.15 - 10 \mu\text{m}$) commonly observed in microcrystalline volcanic rocks. These were formerly termed ‘pseudo-single-domain’ (PSD) and more recently ‘vortex-state’ (VS) particles (Roberts et al., 2017). Their magnetic properties have similarities with the even smaller and magnetically ‘harder’ single-domain (SD) particles ($\sim 0.03 - 0.15 \mu\text{m}$) that ARM_{100mT} quantifies (Figure 1d). SD-sized magnetite often originates from bacterial iron biomineralization or from nepheloid-transported ultrafine detritus. Comparing both records, we find an enhancement of fine magnetite particles in ILs I0, I1 and I2, according to ARM / IRM (not shown) also in I4. The MS maxima in H1, H2 and H3 are not discernible in these records; H4-H6 are recognizable in Figure 1c, but not in Figure 1d. The two scatterplots in Figures 1i and k express this decoupling as large data scatter, broad confidence ranges and low (HLs: $r = 0.75$, ILs: $r = 0.30$) or practically absent (HLs: $r = 0.14$, ILs: $r = 0.15$) correlation. We can state that ‘medium-sized’ PSD magnetite is less and not consistently linked to HLs, while SD magnetite content is uncorrelated to HLs and even more abundant in ILs, hinting at its dilution by HEs.

Stepping from ferrimagnetic to antiferromagnetic mineral content, the signal patterns reverse: The HIRM record (Figure 1e), delineating mainly hematite content, shows minima in HLs where MS has maxima. It follows, that IRD deposited during HEs must have higher magnetite, but considerably lower hematite content so that its admixture to the background

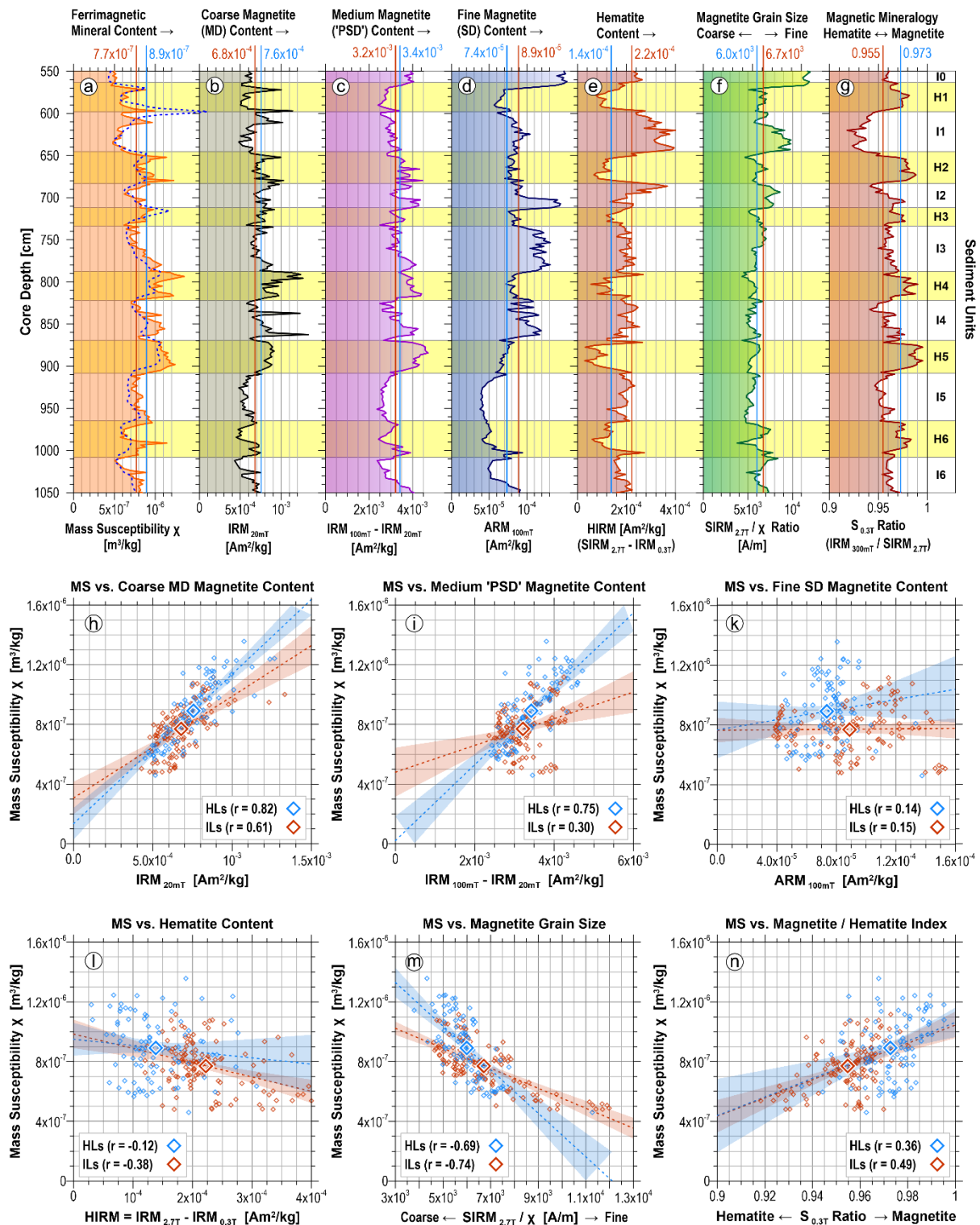


Figure 1: (a) - (g) Standard bulk rock magnetic parameter records of core GeoB 18530-1 based on cube sample measurements adapted from Wang (2016) and arranged following the chrono- and lithostratigraphy of Chapter 2. The two vertical lines and attached values in each plot delineate the respective parameter means for HLs (blue) and ILs (red). The blue dotted line in (a) represents the scale-adjusted magnetic volume susceptibility from a full-core loop-sensor measurement. (h) - (n) Scatterplots of all rock magnetic parameters (b) – (g) against mass susceptibility. The large blue and red symbols mark HL and IL arithmetic means. The figure legends note Pearson’s correlation coefficient r separately for HL and IL data subgroups. The dotted linear regression lines with 95% confidence ranges were also independently calculated for HLs (blue) and ILs (red).

sediment enhances the low-coercivity magnetite fraction and thus dilutes and reduces the high-coercivity hematite fraction. The $S_{0.3T}$ ratio (Figure 1g) shows a shift in the magnetite/hematite proportion at every unit boundary. The HIRM means nearly double from 1.4×10^{-4} Am²/kg in the HLs to 2.2×10^{-4} Am²/kg in the ILs, while the total HIRM ranges from 0.4×10^{-4} to 4.0×10^{-4} Am²/kg. If such large variations in hematite content were only caused by IRD dilution of hematite-rich background sediment, IRD content would have to amount to as much as 90 wt% of the total sediment, which is unlikely. Figures 1l and n suggest that the hematite content can also vary by a factor of ~ 4 within ILs, while its dilution within HLs corresponds to a factor of only ~ 2 . Both factors obviously multiply in order to obtain the large observed hematite variation.

We keep as an interim result that IRD delivered by HEs bears abundant coarse, highly magnetic magnetite, possibly of granitic origin, but lacks hematite, which is associated to the background sediment. Fine and very fine magnetite is equally or even preferentially deposited in ILs. These rock magnetic data could not establish magnetic dilution by diamagnetic calcite and dolomite. To discriminate the interfering magnetic impact of calcareous and plutonic IRD, we first need to involve suitable element ratios derived from XRF core scans.

3.3.2 Geochemical Bulk Sediment Records

The interfering magnetic impact of calcareous and plutonic IRD on MS is better demonstrated by lithology-specific element ratios. Count records for 29 elements were extracted from XRF scans at 50, 30 and 10 kV acceleration voltage (Max et al., 2022). Those of Ca, Sr, Si, K, and Fe were identified as the most indicative for this IRD study. These XRF data are so far only available in units of counts per second (cps) and represent relative element content. In order to eliminate a potential porosity and grain-size biasness (Tjallingii et al., 2007) we only present element ratios (Figure 2). These ratios have been normalized to their own IL mean, so that their values express the relative HL enhancement or reduction relative to background sedimentation.

The Ca/Sr record (Figure 2b) has been key in defining the stratigraphic boundaries of HLs and ILs (Max et al., 2022; Chapter 2) because of its known association with detrital carbonate IRD and its mostly steep, step-like transitions from a constant IL plateau value (here ≈ 1) to a likewise rather stable, two to four times higher HL level. Lower peak values during H6 and H3 conform with previous observations (Grousset et al., 2001). However, the Ca/Si and Sr/Si records in Figure 2c,d reveal that the Ca/Sr ratio is not linear with dolomite content: The ratio's numerator Ca, the predominant cation of low-Mg dolomite, increases two- to eightfold from its stable IL level, while the denominator Sr also doubles, in particular in the younger HLs. The Ca/Si vs. Sr/Si scatterplot (Figure 2h) clarifies that Ca and Sr correlate well both within ILs and within HLs, while the Ca/Sr ratio of HLs is about four times higher. The characteristic angular, i.e. two-endmember data scatter suggests two different calcareous parent materials. We assume Paleozoic limestone and dolostone from Hudson Bay and Hudson Strait for the low-Sr endmember, (Broecker et al., 1992). The high-Sr endmember could be coeval marine carbonate and/or redeposited old carbonate sourced from the Paleozoic and Cretaceous-Tertiary calcareous and siliciclastic bedrocks of the Grand Banks Shelf (Wheeler et al., 1996; Piper and DeWolfe, 2003). Despite high IRD fluxes in the LGM (Chapter 2), the corresponding interlayer I1 stands out by very low Ca and Sr content, which could point to extremely low carbonate production, supporting our first assumption.

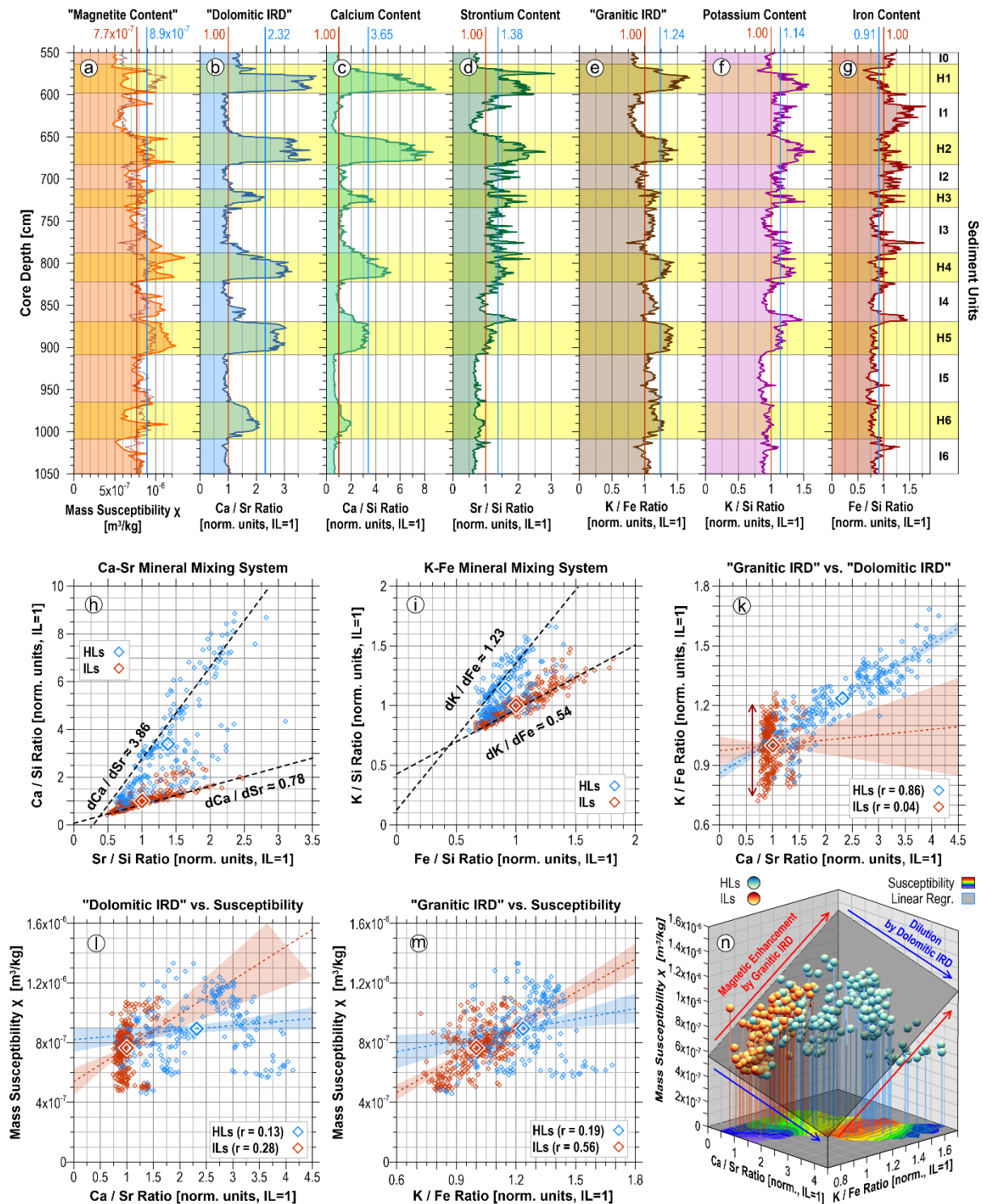


Figure 2: (a) Discrete sample magnetic mass susceptibility χ of Figure 1a. The additional red line represents the MS estimate χ_{est} derived from the regression plane equation of Figure 2n. (b - g) IRD-specific element ratios of core GeoB 18530-1 obtained by high-resolution XRF half-core scanning (Max et al., 2022). These uncalibrated XRF count data are normalized to their IL mean for easier comparability. The two vertical lines and attached values in each plot delineate the respective parameter means of HLs (blue) and ILs (brown). (h - m) Large symbols mark HL and IL means. The dotted linear regression lines are presented with 95% confidence ranges. (h, i) Scatterplots of IL-normalized Ca/Sr vs. Si/Sr and K/Si vs. Fe/Si ratios each delineate two predominant IRD endmembers and their (normalized, i.e. relative) element ratios. (k) Ca/Sr vs. K/Fe scatterplots illustrate the coupling of granite IRD fluxes and to dolomite IRD flux exclusively during HEs ($r = 0.86$). (l, m) Scatterplots illustrating the low bivariate correlation of Ca/Sr and K/Fe to (interpolated) MS particularly in HLs. (n) The 3D scatter plot of MS vs. Ca/Sr and K/Fe demonstrates, that magnetic enhancement by granite and dilution by dolomite partially compensate. The gray linear regression plane and the colored moving average contour plot represent all MS data above.

While literature usually emphasizes dolomitic IRD as HE marker, the widespread abundance and glacial exhumation of Canadian Shield granites counteract such notion as they contribute significantly to IRD in HLs. Coarse biotite-muscovite granite fragments and quartz grains are highly abundant in HLs as well as ILs (Chapter 2). Here we use the K/Fe ratio (Figure 2e) as proxy for granite and similar leucocratic rocks. The K/Fe record shows less prominence, but is still systematically enhanced by 25-50% within HLs (H1, H2, H4 and H5), by a 15-50% K/Si increase and a ~10% Fe/Si decrease (Figure 2 f, g). As evidenced by Figure 2i, the K/Si vs. Fe/Si data scatter also outlines two divergent trends for HLs and ILs, so that the petrology of silicate IRD also changes during HEs. The normalized K/Fe ratio of the HL end-member (1.23) is more than twice that of the IL end-member (0.54). Since the trend line of the ILs does not point towards the origin of the scatterplot, a K-rich background sediment with varying IRD contributions from low-K (ILs) and high-K (HLs) silicate parent rocks has to be assumed.

As Figure 2k demonstrates, 'granitic' and 'dolomitic' IRD fractions are deposited proportionally within HLs ($r = 0.86$), while the granitic IRD fraction varies independently ($r = 0.04$) within ILs (red double arrow) at a low, nearly constant Ca/Sr level. Understandably, the K/Fe pattern (Figure 2e) closely resembles the mineral magnetic $S_{0.3T}$ record (Figure 1g) and muscovite-biotite granite IRD count (Figure 11c, d in Chapter 2). Granitic IRD deposition commonly precedes and succeeds that of dolomitic IRD during HEs. Since the stratigraphic boundaries for HE layers were defined on basis of Ca/Sr shifts, the (dolomite-free) initial and terminal phases of HE-related IRD layers now partly fall into the adjacent late and early ILs.

Figures 2l,m depict the consequences of this situation: Within ILs, the correlation of MS with the variable K/Fe ratio ($r = 0.56$) is much higher than with the nearly constant Ca/Sr ratio ($r = 0.28$). The concurrent, but not strictly proportional admixture of high- χ and low- χ IRD in HLs is mirrored by a large vertical data scatter in these two plots. The magnetic enhancement effect of high granitic IRD input must be partly or fully compensated by high input of low-magnetic dolomitic IRD. The highest χ values observed in the sediment record stem from high granite and lower dolomite content. The relation of Ca/Sr to χ is overall weak however, the correlation coefficient is positive ($r = 0.13$) in HLs and the coeval deposition of dolomitic and granitic IRD also showcased a positive correlation (Figure 2k). It is thus advisable to separate the magnetic influences of both fractions by multivariate linear regression. The resulting 3D scatterplot (Figure 2n) nicely reveals the hypothesized magnetic compensation of both major lithic fractions: The tilt of the regression plane (with $r = 0.58$) illustrates, that the magnetic enhancement by high-magnetic granitic IRD exceeds the magnetic dilution by low-magnetic dolomitic IRD for major parts of their joint mixing space. However, a relative MS decline at high Ca/Sr contents is also clearly evidenced by this plot.

The mutual balance of MS enhancement by granitic IRD and diminution by dolomitic IRD obviously varies between and within HEs. This is probably why HLs H1-H6 are not associated with well-defined MS highs, but instead with successions of MS spikes and troughs (Figure 2a). The equation for the least-square-fitted 3D regression plane in Figure 2n is given by

$$\chi_{\text{est}} = 8.7 \cdot 10^{-7} (\text{K/Fe})_{\text{norm}} - 7.1 \cdot 10^{-8} (\text{Ca/Sr})_{\text{norm}} - 0.44 \cdot 10^{-7} [\text{m}^3/\text{kg}] \quad (\text{Equation 2})$$

which can be used to estimate the MS signal from the K/Fe and Ca/Sr ratios (red line in Figure 2a). The resulting χ_{est} record has indeed many commonalities with the original χ record,

particularly within I1, I4 and I5, though with considerable deviation in pattern. These ‘model deficiencies’ might result from the oversimplified assumption and quantification of only two IRD end-members in addition to the grain-size biasness of XRF scan data. However, before we can engage into more realistic and complex MS models, it is necessary to understand how coarse (>1 mm) IRD counts compare to total IRD content, primarily a question of IRD grain-size distribution.

3.3.3 Sedimentological Bulk Sediment Records

Available bulk sedimentological data obtained by Wang (2016) comprises of wet and dry weights of the sieved 10 cm³ syringe samples (from which porosity Φ and particle density ρ_{part} were derived), the weights of the ‘fine’ IRD >125 μm fraction (with microfossils removed) and the ‘coarse’ IRD >1 mm fraction, (Figure 3b-g). We therefrom add a simple IRD coarseness ratio (IRD >1 mm counts per IRD >125 μm wt%; Figure 3e). Despite their limitations, these few sedimentological bulk records permit valid conclusions on total IRD content, IRD grain-size distribution, and their impact MS. The calculated particle densities ρ_{part} (Figure 3g) of HLs (2.81 g/cm³) and ILs (2.74 g/cm³) nearly match and agree with known IRD lithologies such as dolomite (2.84 g/cm³) or granite (2.65-2.75 g/cm³).

Enhanced IRD content is observed in all HLs and in the ILs I1 and I2 corresponding to the Last Glacial Maximum (LGM). Fine IRD content and coarse IRD counts (Figures 3b, c) peak in particular at the top and bottom of HL sections. These double peaks are congruent with findings of previous HE studies (Bond et al., 1992; Rashid et al., 2003; Hodell et al., 2017). The weight percentage of IRD >125 μm correlates well with that of IRD >1 mm (HLs: $r = 0.71$, ILs: $r = 0.82$, Figure 3h) and with IRD counts (HLs: $r = 0.70$, ILs: $r = 0.87$; Figure 3i). Both scatterplots show considerable vertical spread, hence variability in IRD grain-size. The large and systematic change of IRD coarseness at each HL/II boundary (Figure 3e) implies, that IRD fining and coarsening is by no means accidental, but a specific trait of every HE cycle.

It can be inferred from the linear regression functions of the three IRD content that about 15% of the IRD particles >125 μm are >1 mm therefore, each IRD >1 mm particle in 1 cm³ of sediment roughly represent ~ 3 wt% of IRD >125 μm . As grain sizes of IRD and (hemi-)pelagic sedimentation overlap below 125 μm , quantifying fine IRD fractions by sedimentological methods is difficult. However, the age model of core Geob 18530-1 infers that sedimentation rates approximately doubled during HEs. If this doubling were caused by IRD only, IRD weight percentages of HLs would be some 50% higher than those of ILs. Despite that some IRD > 125 μm wt% peak values reach 40-50 wt%, the mean values suggest an increase from 9.2 wt% in ILs to 15.0 wt% in HLs (Figure 3b), which is far less than the before hypothesized 50 wt% rise. Consequently, the sedimentation rate doubling in HLs could either result from higher background sedimentation or from a large proportion of unrecognized and hence underestimated silt-sized IRD.

A notable clue is the close affinity of porosity variations to HEs (Figure 3f): On average, porosity Φ decreases by 1/10 from ILs (51.4%) to HLs (46.2%) and features highly significant ($p < 0.0001$) negative correlations to IRD >125 μm content and MS (Figures 3k,n). As IRD particles are mostly non-porous (Chapter 2) and coarser than the background sediment, they counteract sediment sorting and reduce porosity by minimally contributing to porosity themselves. According to the ‘all samples’ regression function

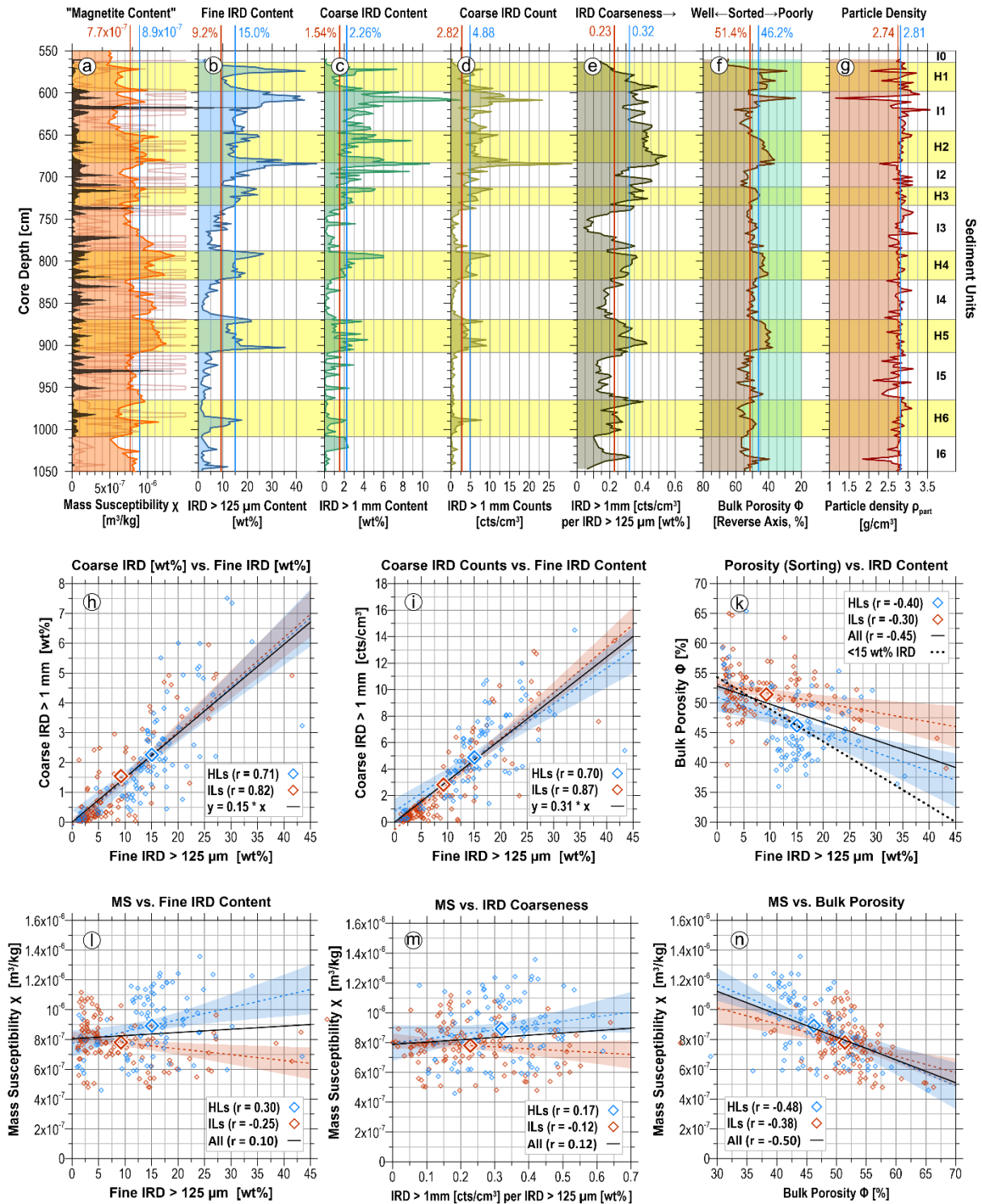


Figure 3: (a) Magnetic mass susceptibility χ of core GeoB 18530-1. The orange curve represents the cube sample bulk MS, the red and black curves mark the MS of the IRD >1 mm fraction (red curve: clipped to axis maximum, black curve: rescaled by a factor of 0.1). (b - g) Sedimentological parameters were determined by weighing (wet, dry) and sieving (>125 μm fraction without foraminifera, >1 mm fraction) of 10 cm³ syringe samples (Wang, 2016). The two vertical lines and attached values in each plot delineate the respective parameter means for HLs (blue) and ILs (red). All records have been depicted and analyzed on basis of the chrono- and lithostratigraphy of Chapter 2 (h - n) Scatterplots illustrating the interrelations of the records above. Symbol and confidence range colors likewise refer to HLs (blue) and ILs (red), large symbols mark HL and IL means. The dotted linear regression lines are presented with 95% confidence ranges. Black regression lines represent merged (HL and IL) data. Numbers in figure legends correspond to Pearson's correlation coefficients or to linear regression equations. Only the black regression lines in (h, i) were forced to pass through $y = 0$; all other regression lines intercept elsewhere.

$$\Phi = -0.30 \text{ IRD}_{>125 \mu\text{m}} + 52.8\% \text{ (based on 0-45 wt\% IRD}_{>125 \mu\text{m}}), \quad \text{(Equation 3a)}$$

an addition of 25 wt% IRD $>125 \mu\text{m}$ entails a porosity reduction of $\sim 7.5\%$, about $1/6 - 1/8$ of the porosity (45-60%) of the low-IRD IL samples (Figure 3k). If samples above 15 wt% IRD $>125 \mu\text{m}$ content are excluded from the above linear regression fit, arguing that high IRD contents could structurally inhibit compaction and dewatering, Equation 3 modifies to

$$\Phi = -0.54 \text{ IRD}_{>125 \mu\text{m}} + 54.3\% \text{ (based on 0-15 wt\% IRD}_{>125 \mu\text{m}}) \text{ (Equation 3b)}$$

An addition of 10% IRD $>125 \mu\text{m}$ fraction thus results in 5.4% porosity loss, which makes sense, since $1/10$ of fine, porous background sediment, and therefore also $1/10$ of its 54% porosity, are being replaced by much larger, mostly pore-free IRD granules.

When comparing the MS values of the bulk sediment to that of the extracted IRD $>1 \text{ mm}$, we observe an enormous sample-to-sample variability of the latter (red/black lines in Figure 3a). The MS of the coarse IRD fraction frequently deviates from the bulk sample MS by an order of magnitude in both directions. The relatively low number of IRD $>1 \text{ mm}$ granules, on average 4.88 per cm^3 in HLs and 2.82 per cm^3 in ILs, leave considerable space for random. The very spiky MS record of the few large IRD particles is obviously neither magnetically representative for the total IRD $<1 \text{ mm}$ fraction, nor is it quantitatively relevant for bulk MS.

In consideration of the recognizable similarities of the MS and IRD patterns (Figure 3a-d), their mutual correlation (Figure 3l) is surprisingly low: While for the merged data, the correlation ($r = 0.1$) is insignificant, the correlations within HLs ($r = 0.30$) and ILs ($r = -0.25$) reach a 99% significance level, but have opposite signs. This antagonism signalizes, that the lithological balance between magnetic enhancement and dilution is delicate. Depending on its composition, IRD may raise or lower the MS of the background sediment: In ILs I3 and I4, an increase in IRD goes along with a decrease in MS, while IRD content closely follows MS in H4 and H5. Similar statements can be made regarding the linkage of MS and IRD coarseness (Figure 3m), where both parameters are not linearly correlated despite shifting to higher values in HLs.

From all tested bulk sediment impact factors of MS, porosity Φ (Figure 3n) peaks out with the highest, yet negative correlation ($r = -0.50$). This is notable as we deal with mass susceptibility, where pore space a priori plays no role. Consequently, we have to envisage bulk porosity here as a proxy for IRD and/or background sediment lithology, since IRD content itself is not nearly correlated as highly with MS (Figure 3l). IRD porosity could play a role in the sense that more porous IRD lithologies (e.g. sand- and claystone, scoria) may be associated with lower MS. Alternatively or additionally, porosity changes could be caused by the fine end of the grain-size spectrum, i.e. the silt- and clay-fraction components, that may be terrigenous or biogenic. Furthermore, the distinct grain morphology of high-MS magmatic or low-MS calcareous IRD may have a textural impact on the sediment that is reflected in porosity.

3.4 Magnetic Properties of Classified IRD Lithologies

How (and how well) each of the $k = 22$ IRD lithologies classified by Bukar et al. (Chapter 2) impact the dry bulk MS record χ_{db} , depends on its respective mass-specific concentration c_i as well as on its MS contrast $\Delta\chi_i = \chi_i - \chi_0$ to an assumed 'background sediment susceptibility' χ_0 :

$$\chi_{\text{db}} = \sum_{i=0}^k c_i \chi_i = (1 - \sum_{i=1}^k c_i) \chi_0 + \sum_{i=1}^k c_i \chi_i = \chi_0 + \sum_{i=1}^k c_i (\chi_i - \chi_0) \quad (\text{Eq. 4})$$

The mass-specific susceptibilities χ_i of the distinguishable IRD lithologies differ largely in function of their composition and ferrimagnetic mineral contents. Equation 4 can be formulated analogously for all ‘linear’, i.e. concentration-dependent rock magnetic parameters like IRM, ARM and HIRM. We provide here – to our understanding for the first time – lithology-specific rock magnetic parameter values and IRM coercivity spectra of IRD particles. These numeric help to assess the impact of individual IRD species on established bulk rock magnetic records. Furthermore, rock magnetic fingerprinting of individual IRD species may be useful for a later comparison with potential parent rock formations.

3.4.1 Magnetic Susceptibility and Remanence-based Rock-Magnetic Properties

The compilation of magnetic concentration (Figure 4), mineralogy and grain-size parameters of individual IRD species revealed a very large (except for $S_{0.3T}$) logarithmically scaled data spread. Equivalent magnetite content (Figure 4a) ranges over four order magnitude i.e. from less than 1 ppm to more than 1% likewise the hematite content (Figure 4c) also spreads equally. The magnetogranulometric SIRM/ χ ratio (Figure 4e) varies by a factor of 500 i.e. from coarse MD (e.g. granite) to stable SD (e.g. quartz) characteristics. Averaged IRD counts (Figure 4d), provided separately for HL and IL units, highlight the relative abundance and stratigraphic affinity of each IRD species; these differ from nearly equal abundance in ILs and HLs to a tenfold increase (gabbro) or reduction (mudstone) in HLs relative to ILs.

IRD lithologies (Figure 4a) have been arranged in ascending MS rank order from nearly pure diamagnetic quartz ($-2 \cdot 10^{-9} \text{ m}^3/\text{kg}$) to magnetite-rich amphibolite ($7.6 \cdot 10^{-6} \text{ m}^3/\text{kg}$). In each plot, the mean of all ILs and HLs of bulk sample data was used as a baseline (vertical blue and red lines). The MS values presented here fall into the typically broad value ranges found in literature (e.g. Telford et al., 1990). Interestingly, only six IRD lithologies (hornblende granite, scoria, muscovite-biotite granite, obsidian, tonalite and amphibolite) exceeded the ‘background’ MS and may contribute to an MS increase in HLs. Considering their preferential deposition during HLs or ILs (blue and brown bars Figure 4d) only three of candidates remained predominant during HLs (muscovite-biotite granite, obsidian, tonalite). Taking also into account, that content and HE-related increase of muscovite-biotite granite exceeds that of obsidian and tonalite by a factor of ten (Figure 4d). It appears that only this singular IRD lithology may have the impact to decisively enhance bulk MS in HLs.

Given that the MS of muscovite-biotite granite ($28 \cdot 10^{-7} \text{ m}^3/\text{kg}$) exceeds the background MS ($7.7 \cdot 10^{-7} \text{ m}^3/\text{kg}$) by a factor of ~ 4 , a 10% admixture of granitic IRD (following Equation 4) would raise bulk MS by $\sim 25\%$ to $9.7 \cdot 10^{-7} \text{ m}^3/\text{kg}$. Principally, a net bulk MS enhancement could also result from an absence of low-magnetic, IL-affine IRD (mudstone, biotite granite, sucrosic dolomite) in HLs, but their low counts and weak MS contrasts do not permit them to influence the signal positively. The only significant reduction of bulk MS arises from ooidal dolomite in HLs, where a 20% admixture would lower the background MS by $\sim 15\%$ to $6.6 \cdot 10^{-7} \text{ m}^3/\text{kg}$. These still rough, but now data-based mixing calculations point out, that our previous proxy-based interpretation (Figure 2n) is already heading towards the proposed understanding.

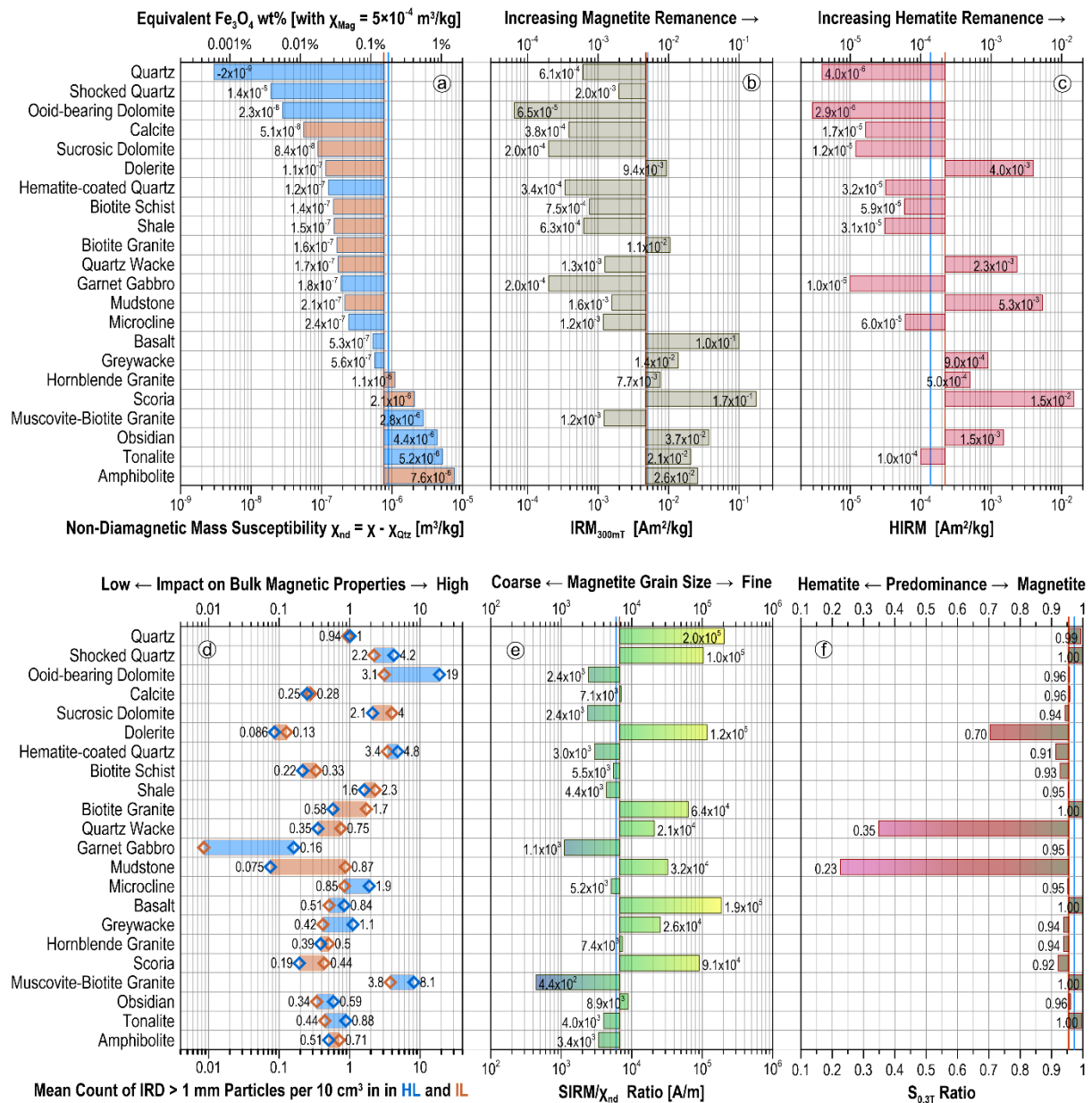


Figure 4: Rock-magnetic properties of all 22 IRD lithologies of core Geob 18530-1 identified and classified in Chapter 2. (a) IRD lithologies are vertically ranked and plotted according to their ‘non-diamagnetic’ mass susceptibility $\chi_{nd} = \chi + 5 \cdot 10^{-9} m^3/kg$. Reducing MS by the small diamagnetic MS of pure quartz avoids negative MS values and thus enables a joint logarithmic depiction. The MS values specified at the horizontal bars ends are uncorrected. All bars originate from the IL bulk MS average of $7.7 \cdot 10^{-7}$ to signalize the negative or positive impact of each IRD species on bulk MS. Blue (brown) bars symbolize higher IRD abundance in HLs (ILs). The top axis provides a fictive magnetite (Fe_3O_4) concentration equivalent. (b) IRM_{300mT} is also proportional to magnetite content, but additionally influenced by the domain state of the magnetite particles and thus considerably differing from (a). (c) HIRM represents high-coercivity minerals such as (predominantly) hematite and (eventually) goethite. (d) The averaged IRD > 1 mm particle counts in HLs (blue) and ILs (brown) indicate, how much individual IRD lithologies contribute to the bulk MS record in terms of absolute content (signal shift) and HL-IL variability (signal pattern). Ooid-bearing dolomite and muscovite-biotite granite clearly excel. (e) The $SIRM/\chi_{nd}$ ratio is a grain-size proxy for ferrimagnetic minerals such as magnetite, where plutonic rocks such as granite and gabbro score low and volcanic rocks such as basalt and dolerite score high. It explains the differences between (a) and (b). (f) The $S_{0.3T}$ ratio signalizes, if higher-coercive antiferromagnetic IRD ($S_{0.3T} < 1$) such as mudstone, quartz wacke and dolerite, or by lower-coercive ferrimagnetic IRD ($S_{0.3T} \approx 1$) prevail.

Muscovite-biotite granite IRD contains coarse magnetite crystals with typical MD properties: high MS (Figure 4a), but low IRM_{300mT} (Figure 4b, e) and coercivity (Figure 4f). It is therefore very effective in upshifting the MS especially within HLs as revealed in IRM_{20mT} and $S_{0.3T}$ records (Figure 1, b, g) and downshifting the SIRM/ χ record (Figure 1f) while not affecting ARM or HIRM much (Figure 1d, e). Ice-rafted tonalite and gabbro are also more abundant in HLs (Figure 4d) and have similar MD-type magnetic characteristics. As minor components, they are irrelevant for bulk magnetism, but of interest for IRD provenance and transport studies.

The impact of plutonic IRD on all magnetic IRD records signal would even be larger, if the concurrent deposition of dolomitic IRD would not act as low-magnetic dilutants (Figure 4a, b) of all concentration-dependent magnetic records. This effect could be experimentally validated by decalcifying the sediment. Shocked quartz IRD is a further, relatively common and HE-affine low-magnetic dilutant whose impact is counter-balanced by sucrosic dolomite, which has similar low-magnetic properties and is more abundant in ILs (Figure 4d).

Volcanic IRD species (basalt, scoria, dolerite, obsidian) have much smaller (titano-) magnetite grains with SD/PSD character and very high IRM_{300mT} (Figure 4b) and SIRM/ χ values (Figure 4e). Their occurrence seems to be episodic and uncorrelated to HEs (Figure 4d) thus creating signal spikes and scatter in SIRM and ARM records. Given that the nearest volcanic formation, of Neoproterozoic age, is at Newfoundland's Avalon Peninsula, while other potential volcanic sources are in Central Western Greenland (Disko Island) and of Late Cretaceous and Paleocene ages (Figure 2 in Chapter 2). The volcanic IRD granules must have originated from ice-rafting due to the severe level of weathering of the IRD as observed in the thin sections (Figure 6 of Chapter 2) and not from recent volcanic ejections. Scoria may be an exception to that, since far-distance floating of scoria and pumice has been observed.

One of the most prominent and significant bulk magnetic features of HLs is a lower hematite content (Figure 1e, g), which may be due to changing background sedimentation, e.g. a reduced or diluted input from the proximal Appalachian Red Bed formations, that should be associated with also lower input of hematite-rich IRD. Very high HIRM values and very low $S_{0.3T}$ ratios (Figure 4c, f) are observed for bright-red mudstone and quartz wacke IRD that prevail in ILs (Figure 4d). Highly oxidized volcanic IRD species such as dolerite and scoria are also very rich in hematite, but bear magnetite as well, so that their $S_{0.3T}$ ratio is not as low as of the aforementioned sedimentary rocks (Figure 4c, f). Bukar et al. (Chapter 2) describe some volcanic IRD as reddish and Leng et al. (2019) also list Newfoundland's red Neoproterozoic Avalon volcanics as foremost hematite-rich lithology in the Laurentian Channel Ice Stream catchment; their source-based HIRM/IRM ratio of 0.28 is not far from our dolomite value of 0.42.

Combining rock magnetic properties and specific abundances of individual IRD lithologies now permits to identify lithology specific candidates that can most likely contribute to the observed HE-specific signals in the various bulk magnetic records. Less than half of the 22 classified IRD lithologies are of sufficient abundance and magnetic contrast to have noticeable impact on bulk magnetic records. Even fewer IRD species are so closely associated to HLs or ILs to be considered relevant for HE-specific signal pattern formation.

Using the above introduced 'rule of thumb' relation (Figure 3i) of 1 IRD >1 mm count per cm^3 for 3 IRM >125 μm wt%, and inserting the respective HL and IL counts of Figure 4d into the

partial susceptibility sum for total IRD ($\sum_{i=1}^{22} c_i \chi_i$), we get partial MS values of $0.71 \cdot 10^{-7} \text{ m}^3/\text{kg}$ for ILs and of $1.13 \cdot 10^{-7} \text{ m}^3/\text{kg}$ for HLs. These amount to $\sim 9\%$ of bulk IL MS ($7.69 \cdot 10^{-7} \text{ m}^3/\text{kg}$) and $\sim 13\%$ of bulk HL MS ($8.92 \cdot 10^{-7} \text{ m}^3/\text{kg}$). The IRD $>125 \mu\text{m}$ contributions to MS conform also to the averaged IRM $>125 \mu\text{m}$ contents of 10 wt% (ILs) and 15 wt% (HLs) (Figure 3b). These rather similar total IRD MS values feed the assumption that the magnetic enhancement and dilution effects by IRD species of higher and lower than background MS largely cancel each other out. By summing up the effective partial susceptibilities $\Delta\chi_i$ of 'lower and higher than background MS' IRD groups, one reaches a puzzling result: the MS of the background sediment and of the cumulative IRD differ barely! An obvious conclusion might be that both may have geologically similar origins.

3.4.2 IRM Acquisition Curve Analyses of Bulk Sediment and Classified IRD

Magnetic fingerprinting based on the coercivity spectra of IRM acquisition curves or first-order reversal curves (FORCs) is a common enviro-magnetic unmixing approach used to determine and quantify separate magnetic mineral or source components of clastic sediment (Heslop, 2015, Robertson & France, 1994). The 22 classified IRD lithologies (Chapter 2) have a hugely varying magnetic mineral content (Figure 4a) and mostly just minor contributions to the magnetic mineral assemblage of the bulk sediment, an unfavorable setup for IRD species quantification by inverse magnetic modelling. Presenting, classifying and analyzing the coercivity spectra of the identified IRD species could nevertheless have diagnostic value for parent rock identification and may help to interpret extracted, but unclassified IRD.

To identify and distinguish the remanent-carrying magnetic minerals in IRD particles by their magnetic coercivity distributions, IRM acquisition curves from 10 to 2700 mT were recorded and analyzed. In Figures 5 and 5 cont., we present stacked SIRM-normalized IRM acquisition curves for all bulk unclassified $>1 \text{ mm}$ IRD (216 samples) and separate, mass-calibrated IRM curves for all 22 classified IRM lithologies (Chapter 2). As can be noted, most IRM acquisition curves do not start from zero, since all extracted IRD particles had experienced high magnetic fields for bulk IRD magnetization and their alternating field (AF) demagnetization was not fully effective. The first IRM acquisition (pulse) field step of 10 mT was also often too large in consideration of the low IRM coercivity of plutonic IRD. Future rock magnetic IRD studies are advised to start IRM acquisition curves from 1 mT onward which our inline 2G pulse magnetizer unfortunately does not technically allow.

To determine the main magnetic mineral components of each IRD lithology and compare these with bulk IRD fractions, we used the skewed generalized Gaussian (SGG) distribution analysis of IRM acquisition curves proposed by Egli (2003) and implemented in the R-Studio-based MAX UnMix online app by Maxbauer et al. (2016). IRM coercivity spectra of natural samples can be approximated by mixing an arbitrary number of skewed log Gaussian functions where each is described by four parameters: (1) *SIRM* determines the height of the cumulative log Gaussian, i.e. its contribution to the IRM curve model, (2) the half-field $B_{1/2}$ denotes the applied magnetic field that generates half of the saturation IRM; these apparent coercivities have been denoted as C1 and C2 in our plots. The (3) dispersion parameter *DP* and (4) skew factor *s* finally control the width and asymmetry of each model curve (Kruiver et al., 2001; Egli, 2003).

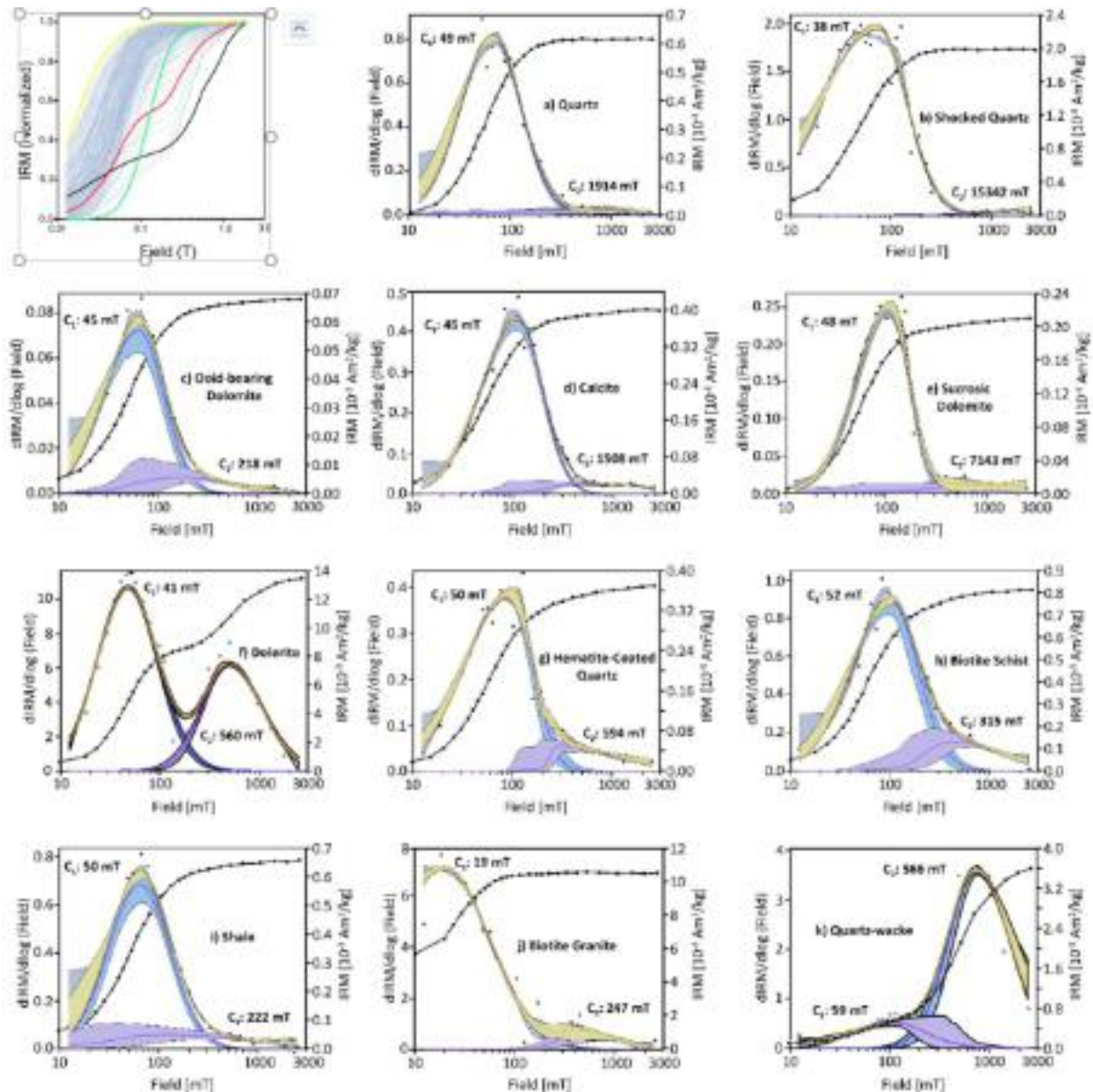


Figure 5: top left: Normalized composite IRM acquisition curves of all 216 unclassified IRM > 1 mm sieve samples with four magnetically distinct curves colored in yellow, green, red and black. (a-k) Mass calibrated IRM acquisition curves (black lines) of individual IRD lithologies sorted with low to medium MS (see Figure 4a). The dotted black curve depicts the derivative curve and the yellow band the respective SGG model, usually composed of two (blue and purple) model curves C1 and C2.

For mutual comparability, all 216 normalized bulk IRM acquisition curves have been shown in both parts of the two-paged Figure 5. The four (4) bolded curves in hues of yellow, green, red and black represent contrasting individual IRM acquisition curves that highlight the dominance of certain remanence-carrying magnetic minerals (magnetite or hematite). The yellow and green curves saturate at low applied fields showcasing two distinct cases of prevailing ferrimagnetism; these bracket all magnetite dominated IRD samples. The yellow curve is characteristic of coarse multi-domain magnetite whereas the green curve has features of fine single-domain magnetite inclusions as in quartz, obsidian or greywacke. The red and black curves denote samples with predominance of antiferromagnetism that is saturated at higher fields. These curves conform to a few lithology-specific samples acquisition curves, for

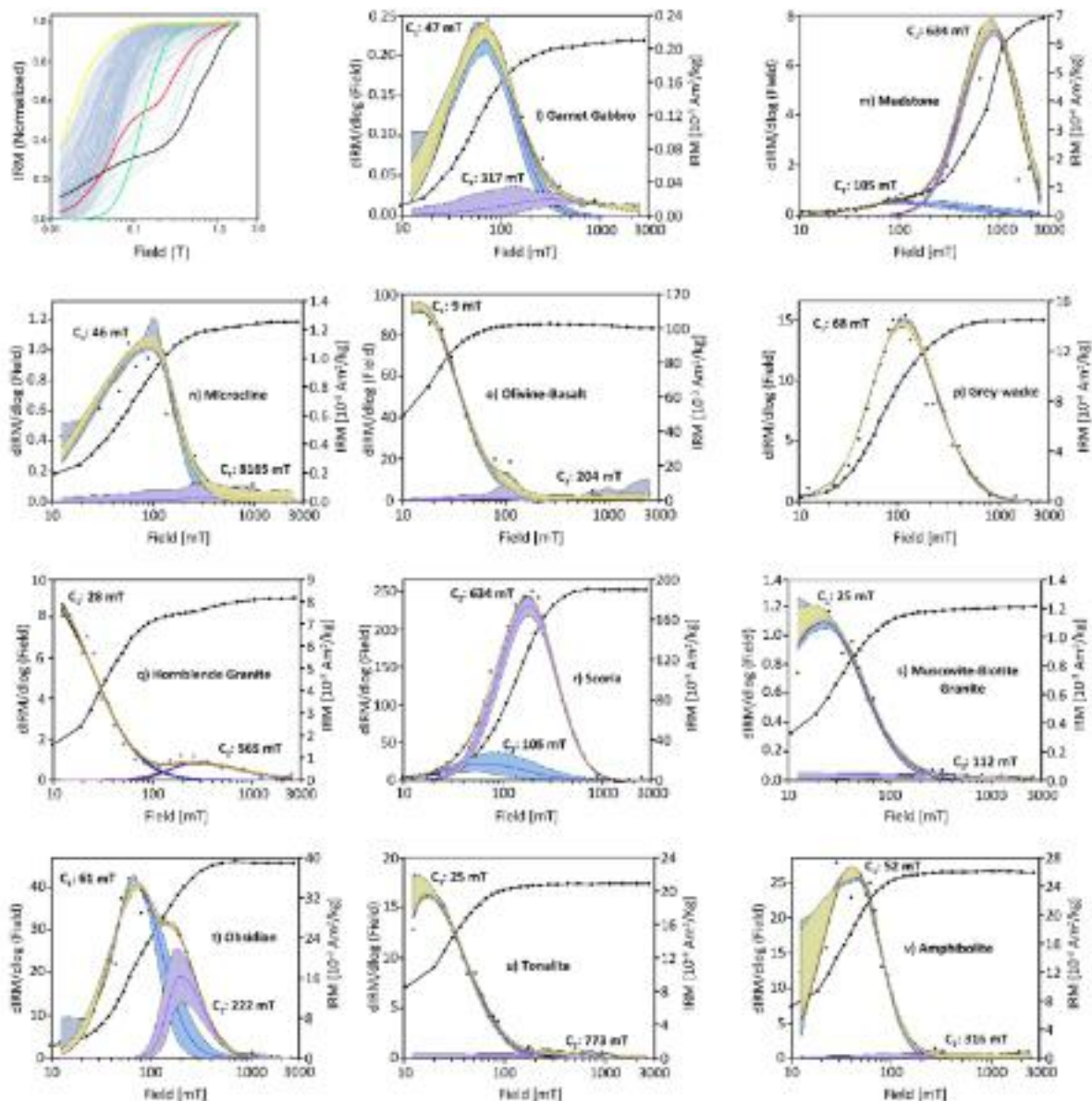


Figure 5 cont.: (l-v) Mass calibrated IRM acquisition curves (black lines) of individual IRD lithologies sorted with medium to high MS (see Figure 4a). The dotted black curve depicts the derivative curve and the yellow band the respective SGG model, usually composed of two (blue and purple) model curves C1 and C2.

instance the red-colored acquisition curve is similar to that of dolerite and the black-bolded curve is nearly indistinguishable from the quartz-wacke curve. Such entails that IRD samples with few particles can be predominantly composed by just one single and mostly antiferromagnetic IRD lithology (like dolerite or quartz-wacke). About 50% of the IRD lithologies are typified by $B_{1/2}$ values < 50 mT which by implies that their saturation magnetizations were attained at applied fields 100 – 300 mT. All these IRD assemblages show dominance of MD to PSD magnetite, a characteristic of plutonic rocks.

Texturally, most intrusive rocks are composed of medium to coarse grained crystals as larger magnetite crystals can form during their slow cooling. All coercivity spectra of plutonic IRD lithologies (biotite-granite, tonalite, muscovite-biotite-granite, hornblende-granite and garnet-gabbro) showcase $B_{1/2}$ fields of less than 50 mT indicating MD- to PSD-type magnetite crystals. As proposed by Robertson & France (1994), their dispersion parameter DP of ~ 0.3 is also typical

for MD magnetite. The coercivity spectra of these IRD lithologies are either composed of one or two magnetic components, where the higher coercivity denote the presence of hematite (i.e. $B_{1/2}$ of 479 mT in hornblende-granite and 306 mT in garnet-gabbro).

The petrographic settings of extrusive rocks results in finer magnetite crystals due to the much shorter magma solidification phase. However, it is also common to find basaltic rocks with large phenocrysts enlaced by fine crystals (e.g. olivine crystals within fine needle-shaped plagioclase crystals). In the description of olivine-basalt reported by Bukar et al. (Chapter 2), a considerable number of dark 'blobs' within tiny crystal slabs of plagioclase were identified. Though, no effort was made in ascertaining whether these large opaque minerals were actually magnetite, this assumption is buttressed by the coercivity spectrum. The coercivity spectrum of the olivine-basalt reveals magnetically soft MD magnetite properties with the lowest $B_{1/2}$ (12.5 mT) of all IRD lithologies. Petrographically, scoria and obsidian are both made up of very fine to glassy crystal that can hardly be seen under petrographic microscope. Their coercivity spectra reveal much higher $B_{1/2}$ values (56 mT and 66 mT) which typifies pseudo-single to single domain magnetite, i.e. fine- to medium-sized crystals); both lithologies also show two components.

Rocks that form as sub-volcanic intrusions usually have fine to medium grain textures as their cooling processes is gentler compared to rocks formed through fissure eruptions. Dolerites occur as dykes and sills and hence have fine to medium crystals as described in Chapter 2. As the coercivity spectrum shows, the dark-reddish dolomite consist of a medium-coercive (41 mT) magnetite and high-coercive (560 mT) hematite component. Depending on the degree of metamorphism, some protoliths tend to retain characteristic primary properties in addition to forming metamorphic secondary crystals. Amphibolite IRD ($B_{1/2}$: 32.5 mT) has a softer, hence likely coarser magnetite component than biotite-schist ($B_{1/2}$: 50 mT).

IRD particles consisting of a singular rock-forming mineral are fragments of intrusive rocks that have been reworked by sedimentary processes. This group encompasses shocked-quartz, quartz, hematite-coated quartz and microcline; they all seem to have fine magnetite inclusions with respective $B_{1/2}$ values of 45 mT, 50 mT, 53 mT and 54 mT. In pink, hematite-coated quartz and microcline a substantial presence of hematite is shown by secondary high-coercive components.

Siliciclastic sedimentary processes on continents often involve the oxidation of iron-oxides that gives red or pink hues to sedimentary materials. As described in Chapter 2, quartz-wacke and mudstone shows reddish and pinkish coloration which signalize the presence of hematite. This is substantiated by their coercivity spectra, where hematite with high $B_{1/2}$ values of 569 mT and 637 mT dominates over magnetite. Grey-wacke shows just one magnetite component with a relatively high $B_{1/2}$ of 74 mT. The petrology of shale is primarily composed of fine clayey materials mixed with quartz and some carbonate; its IRD showcases a coercivity spectrum of two component with a predominant magnetite $B_{1/2}$ value 50 mT. The calcite and the two dolomite IRD lithologies have similar magnetite-like $B_{1/2}$ values of ~45 mT and some minor high-coercive mineral components.

3.5 Empirical and Conceptual MS Models of Glaciomarine Sediment

3.5.1 Grain-Size Dependence of MS and Grain-Size Distribution of IRD

As IRD was initially detached from the parent rock by the thrust of the overriding ice-sheet and milled down further in the slip layer creating poorly sorted IRD grain-size distributions, IRD grain size gradations vary with the crystallinity, hardness and shear resistance of the parent rock type as well as with the provenance-specific under-ice transport distance and conditions. Since magnetite is uncommonly hard ($5\frac{1}{2}$ - $6\frac{1}{2}$) and dense (5.18 g/cm^3) and highly resistant to physical weathering, it is often found enriched as residual mineral component in sediments and soils. Isolated, monocrystalline magnetite crystals of plutonic and metamorphic rocks should fall into the silt-sized IRD fraction, while the medium- and coarse-grained IRD fraction is mostly polycrystalline and polymineralic. Rock magnetic analyses of sieved fractions from riverine, coastal and eolian sediments (Badesab et al., 2017; Razik et al., 2014) revealed, that the magnetite content of the 30-125 μm fraction exceeded that of the 125-1000 μm fraction by far, where instead low-magnetic minerals with larger crystal like quartz and feldspar prevail. The very coarse IRD particles $>1 \text{ mm}$ are mostly polycrystalline lithic fragments and therefore represent the parent rock petrology and their MS much better than the finer IRD fractions.

The lithology-specific IRD weight percentages c_i and mass susceptibilities χ_i of Equation 4 are so far theoretical numbers, that are not equivalent with the counts n_i and MS values χ'_i of classified IRD $>1 \text{ mm}$ particles. Both these experimentally obtainable numbers should be much smaller than and are possibly not even proportional to total sediment content and effective MS of a given respective IRD species. To transform Equation 4 into a forward MS model based on classified IRD particle counts, one would have to introduce additional 'proportionality' factors w_i and v_i to respectively accommodate for (1) expanding IRD granule count to total weight percentage, and (2) expanding granule MS to grain-size-averaged MS.

$$\chi_{\text{db}} = c_0\chi_0 + \sum_{i=1}^k w_i n_i v_i \chi'_i = \chi_0 + \sum_{i=1}^k w_i n_i (v_i \chi'_i - \chi_0) \quad (\text{Equation 5})$$

Both factors, w_i and v_i , could vary from sample to sample; similarly, the non-IRD background MS χ_0 could also be non-uniform throughout the sedimentary record (which is very likely). It is therefore not to be expected that this numerical approach could lead to a good deterministic petrological model for glaciomarine sediments. However, it appears useful to examine the idea further and to determine the dimension of w_i , and of the coarse-to-cumulative IRD factor v_i .

In order to substantiate the above considerations and encompass a rough estimate for w , we performed a magnetic analysis on a sieved sediments similar to the above mentioned studies (Badesab et al., 2017; (Razik et al., 2014). Three sets of 7 - 8 syringe samples, totaling 65 - 75 cm^3 of each layer, were collected in depth steps of 2 cm from core GeoB18530-1 at depths of 576 - 590 cm (HL1), 631 - 643 cm (IL1) and 655 - 667 cm (HL2). These intervals have large IRD $>125 \mu\text{m}$ contents of 15 - 40 wt% (Figure 3b). After ultrasonic suspension in distilled water, a motor-driven wet-sieve apparatus was used to stepwise fractionate this suspension into 17 grain-size fractions from $>2 \text{ mm}$ down to $>5 \mu\text{m}$ in mesh steps of approximately 0.5 Φ units ($\times 0.7071$). The inseparable clay-size fraction (here $< 5 \mu\text{m}$) was discarded. All sieved fractions were dried and weighed (4.3 - 12.3 g) and subsequently their bulk MS was measured.

Figure 6 displays the obtained sieve analysis data in six diagnostic histogram styles providing clues for the above depicted problem. Median and main mode of the grain-size distribution are in the 40 - 60 μm range; a minor second mode with $\sim 5\%$ total contribution is recognizable at the coarse end ($>1 \text{ mm}$) of the histogram. The interquartile range reaches from 20 μm to $\sim 125 \mu\text{m}$, attesting very poor particle sorting (Figures 7a, b). MS shows systematic grain-size dependence (Figure 7c), where the sortable silt $< 40 \mu\text{m}$, considered as background sediment

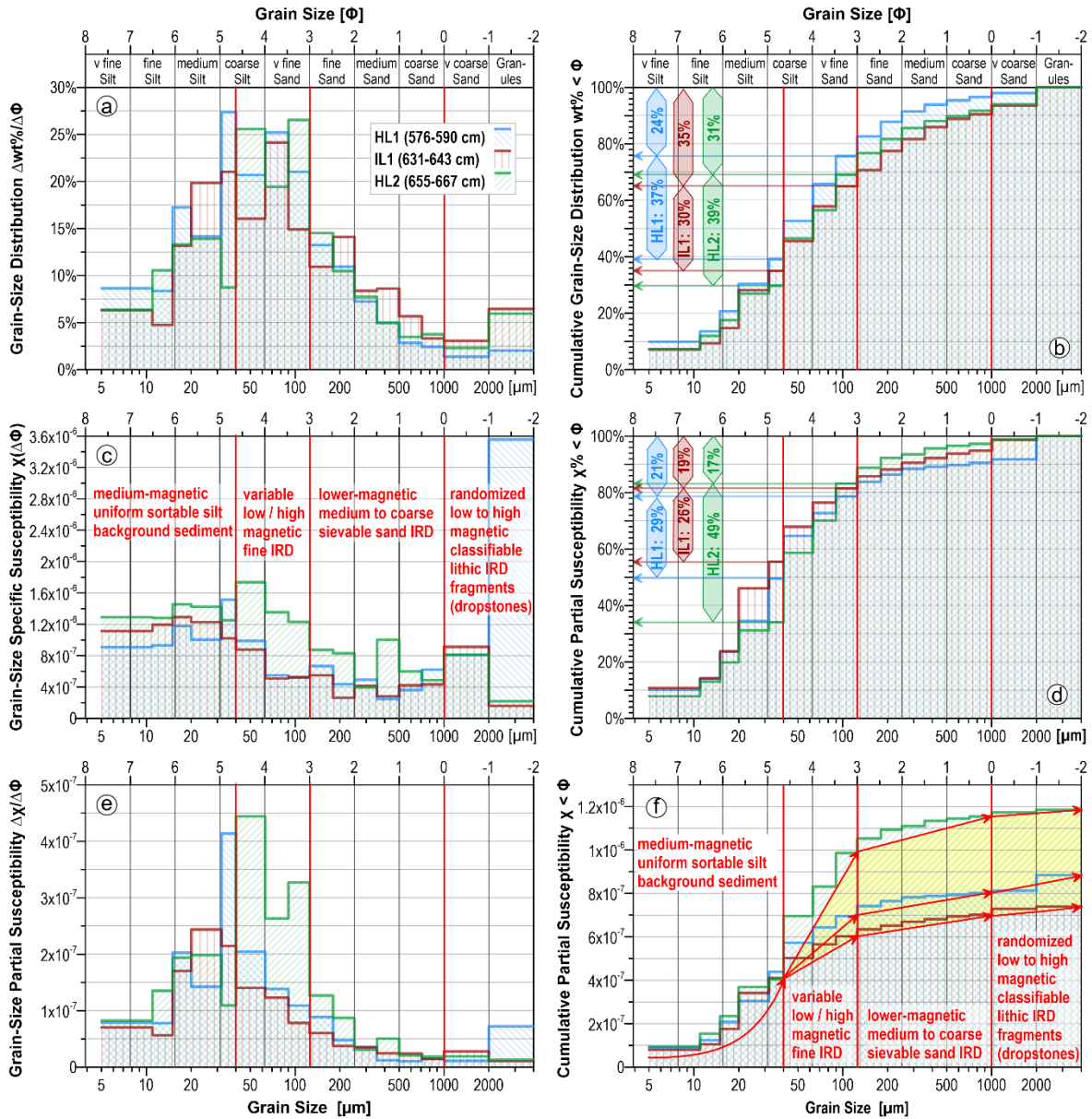


Figure 6: Grain-size frequency distribution and grain-size dependency of MS in three stratigraphic units (HL1, IL1, HL2) of core Geob18530-1. (a) Weight percentage of wet-sieve fraction normalized by their logarithmic mesh difference $\Delta\Phi$, which was constant (0.5) from 63 μm up to 2 mm, but varied between 5 μm and 63 μm . (b) Cumulative weight percentages of all sieve fractions. Arrows mark relative net contributions [%] of the three recognized IRD grain-size fraction derived from (f). (c) Mass-specific MS of all grain-size fractions. MS trends, levels and scatter change at the 40 μm , 125 μm and 1 mm divisions. (d) Cumulative partial MS curve in units of wt%. Arrow and labels denote the relative net contribution of grain-size fractions to bulk MS. (e) Partial susceptibilities in [m^3/kg] of the sieve fractions. Here MS measurements were not normalized by sieve fraction weight as in (c), but in logarithmic mesh difference. This curve corresponds to the product of corresponding values in (a) and (c) and is the derivative of (d). (f) Cumulative partial contributions of sieve-fractions to bulk MS in units of [m^3/kg].

(McCave et al., 1995), has a rather uniform MS of $\sim 9 - 13 \cdot 10^{-7} \text{ m}^3/\text{kg}$, slightly higher than the bulk sediment MS of $\sim 7 - 11 \cdot 10^{-7} \text{ m}^3/\text{kg}$ (Figure 7f). The magnetic uniformity and similar abundance of this sortable silt leads to a nearly congruent initial ascent of all three cumulative partial MS curves from 5 up to 40 μm (Figure 7f). This fraction represents 30 - 40 wt% of the sediment and 35 - 55% of the bulk MS; it contributes $\sim 4 \cdot 10^{-7} \text{ m}^3/\text{kg}$ to bulk MS (Figures 7b,d,f).

From 40 to 125 μm , the grain-size specific MS shows a high variability ($\sim 5 - 17 \cdot 10^{-7} \text{ m}^3/\text{kg}$). Due to the high abundance (30 - 39 wt%) of this fraction, its 'magnetic volatility' leads to large contrasts in the net bulk MS ($2 - 6 \cdot 10^{-7} \text{ m}^3/\text{kg}$ or 26-49%) of the three samples (Figures 7c-f). Under glacial conditions in the NW Atlantic, this grain-size fraction should be largely detrital and too coarse to be current-transported (Leng et al., 2018), hence probably ice-rafted. The coarser IRD fractions $>125 \mu\text{m}$ have lower specific MS ($\sim 3 - 9 \cdot 10^{-7} \text{ m}^3/\text{kg}$) and contribute also much less ($1.5 - 2 \cdot 10^{-7} \text{ m}^3/\text{kg}$) to bulk MS (Figures 7e,d,f). The few IRD particles $>1 \text{ mm}$ cause small random shifts ($0.2 - 1 \cdot 10^{-7} \text{ m}^3/\text{kg}$) at the tail end of the cumulative MS distribution (Figure 7f). In conclusion, the 'undetected', magnetically enhanced fine IRD is the most relevant IRD fraction for the IL/HL distinctions of bulk MS records. 'Classifiable', but randomized and magnetically diverse lithic IRD has only subordinate influence due to its low content $<5 \text{ wt}\%$.

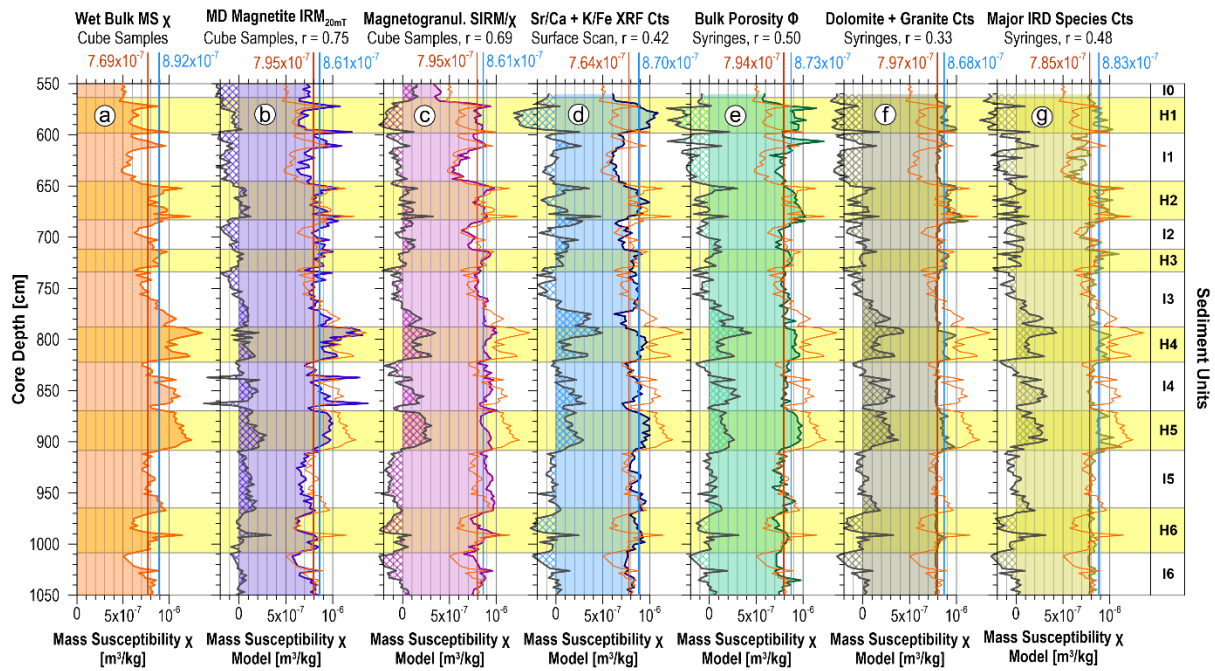
These three sieve analyses are not sufficient to cover the entire lithological variability of the studied core, but their commonalities and differences outline some typical trends and deliver a reasonable data-based value range for w_i . Similarly to the previous transform from IRD $>1 \text{ mm}$ counts to IRD $>125 \mu\text{m}$ wt% (1 ct/cm³ equals 3.1wt%; Figure 3i), Figure 7b now allows us to expand this factor to the fine IRD 40 – 125 μm fraction. This fraction is similarly large as the IRD $>125 \mu\text{m}$ fraction, which would approximately double the previous transform factor. For HL1, we obtain (37% + 24%) / 24% = 2.54, and equivalently 1.86 for IL1 and 2.26 for HL2. Multiplying this expansion factor with the above 3.1 IRD wt% per IRD count, we should expect a total of 6-8 IRD wt% per IRD $>1 \text{ mm}$ grain in 1 cm³; providing us with a guess for w_i .

3.5.2 Modelling Bulk MS from Sediment Properties and Classified IRD Counts

We conclude this data analysis with several linear regression models for the bulk MS record, using other sediment records as 'MS proxies'. This exercise has various aims: It first allows to compare the impact of various well-defined sedimentary properties on the MS signal in a systematic and consistent approach. Secondly, comparing MS model residuals stratigraphically shows best, which MS signal elements are predicted by these 'IRD markers' and which escape them. Thirdly, inconsistencies induced by the stochastic spatial distribution of coarse IRD over sample volumes emerge from comparing records derived from divergent sample volumes.

Browsing over the MS model records of Figure 7 from left (b) to right (g), we find that all MS models on average have higher susceptibilities for HLs that falls into the expected value range. The individual MS model records clearly differ in their ability to predict all signal features of the MS record, which may in parts be owing to random IRD content of the three compared sample series, but more so due to diverging parameter properties.

The two rock magnetic MS models based on IRM_{20mT} and SIRM/ χ (Figure 7b,c) have the highest observed Pearson's r of 0.75 and 0.69 (Figure 1b,f). IRM_{20mT} is a concentration-dependent and SIRM/ χ a concentration-independent parameter. Both delineate the deposition of large, magnetically soft ferrimagnetic particles typical for plutonic rocks of the Canadian Shield. As



all three compared records are from the same sample series, they share even small-scaled, possibly random signal spikes as during H1 and H2. In some sections, the MS models feature parallel offsets resulting in flat model residuals; soft magnetite content controls better the short-range than the long-range MS variability. Larger offsets of the SIRM/ χ model in H4, H5 and H6 show, that IRM_{20mT} recognizes magnetic dilution better than SIRM/ χ .

The two-component Sr/Ca - K/Fe model of Figure 7d is based on XRF-scan data and follows Equation 2. Except for H1 and H6, this model agrees and follows well ($r = 0.42$) the long-range MS pattern. Like the MS parameter itself, this model compromises between the HE-specific Ca/Sr record and the HE-sensitive, but not HE-exclusive K/Fe record (Figure 2a-g). For instance, the prominent MS peak in layer I4 is found neither in the Ca/Sr ratio nor in the IRD counts (Figure 3b-d), but the element model reproduces it. The input of detrital granitic detritus seems to continuously modulate the MS signal, irrespectively whether being delivered by ice-rafting, ocean currents or gravity transport. As element-based MS models are grain-size independent, they reproduce MS changes by fine IRD, plume and background sedimentation.

Admixing coarse, poorly sorted IRD to a well-sorted fine background sediment reduces bulk porosity (Figure 3k, n), which explains the decent correlation ($r = 0.50$) of the porosity MS model (Figure 7e); even spikes of H1 are reproduced. This MS model would perform even better if it could distinguish between dolomitic and granitic IRD as large residuals in H1, H4

and H5 signalize. Conversely to the two previous models, porosity does not show the MS peak of IL4 and underestimates MS minima in I1, I2, H6 and I6, where a pronounced and unusual magnetite fining (Figure 1f) suggests suspended transport. This signalizes, that considerable parts of glaciomarine sedimentation in early and late H6 did not rain out from overpassing icebergs, but instead from hyperpycnal plumes accompanying the ice sheet collapse or from boundary-current transported suspension clouds released from icebergs at higher latitudes.

The MS model based on IRD counts of ooid-bearing dolomite (OBD) and muscovite-biotite granite (MBG) of Figure 7f shows low correlation ($r = 0.33$) with MS and does not adequately reproduce MS minima. This problem may result from not including relevant low-magnetic IL-specific IRD lithologies such as sucrosic dolomite (Figure 4d). Including all major IRD species counts into the MS model (Figure 7g) indeed improves the model performance in IRD-rich IL periods such as I1 and I2, but still fails to predict the MS pattern in low-IRD strata such as I4, I5 and I6. It is insightful to analyze the coefficients in the linear regression equation of the two-component (OBD-MBG) IRD count-based model in comparison with Equation 5:

$$\chi_{db} = 4.08 \cdot 10^{-9} n_{OBD} + 1.65 \cdot 10^{-9} n_{MBG} + 7.78 \cdot 10^{-7} \text{ [m}^3\text{/kg]} \quad (\text{Eq. 6})$$

The regression constant $7.78 \cdot 10^{-7} \text{ m}^3\text{/kg}$ comes close to IL MS mean, the assumed background. However, the two positive IRD count factors make no sense in rock magnetic terms: If we divide them by the previously estimated count-to-weight% conversion factor w_i of $\sim 7\%$ and solve for $v_i \chi_i$ with Equation 5, we obtain $1.36 \cdot 10^{-6} \text{ m}^3\text{/kg}$ for χ_{OBD} and $1.01 \cdot 10^{-6} \text{ m}^3\text{/kg}$ for χ_{MBG} , way off the measured IRD-based MS of $2.30 \cdot 10^{-8} \text{ m}^3\text{/kg}$ for OBD and $2.78 \cdot 10^{-6} \text{ m}^3\text{/kg}$ for MBG. While extending the IRD count model to 13 more relevant IRD lithologies improves the model fit to $r = 0.48$, but the regression coefficients again reveal totally inadequate model assumptions on the specific MS of each IRD lithology. In other words: The classified IRD count records are not suited to create a statistically good and at the same time magnetically meaningful MS model. As we noted before (Figure 3l,m), MS correlates very poorly with IRM $> 125 \mu\text{m}$ content ($r = 0.10$) and IRD coarseness ($r = 0.12$). It seems that w_i and v_i are not time-invariant and the bad performance of IRD count MS models is just the consequence.

3.6 Conclusions

The first part of this study (Chapter 2) analyzed and revealed the petrological complexity of ice-rafted detritus at the Northwest Atlantic Grand Banks Slope, a relatively proximal site along the trajectory of the glacial iceberg armadas, that carried and spread the continental sediment load of episodic Laurentide Ice Sheet collapses all across the northern North Atlantic. As petrological IRD identification and classified counting is confined to coarse, mm-sized IRD particles, only this ‘tip of the IRD iceberg’ was investigated by this approach. While it is straightforward to extrapolate the under- from the overwater volume of an iceberg, this does not apply to IRD analysis, where abundances and magnetic properties of finer sand- and silt-sized IRD fractions not necessarily conform to the identifiable coarse IRD fraction. For an integral view at the magnetic signature of IRD sedimentation, this second study part investigated the same record by bulk magnetic, geochemical and sedimentological analytics.

We departed from the conundrum, that oceanic Heinrich Event Layers are commonly identified by their high contents in ice-rafted detrital dolomite and by their above-background

magnetic susceptibility. The obvious quest, how the addition of low-magnetic dolomitic IRD goes along with enhanced magnetizability of glaciomarine sediments, could be convincingly answered: That the magnetic susceptibility of HE records correlates with coarse magnetite, anticorrelates with hematite and is unrelated to fine magnetite, points at a plutonic IRD source rock. Combining the adverse magnetic effect of granitic (K/Fe) and dolomitic (Ca/Sr) detritus indeed leads to a much better prediction of the MS record, than each individual record. Coarse IRD > 1 mm counts and IRD > 125 μm content are instead poor MS predictors.

In the aim to magnetically characterize the 22 previously classified IRD species and to evaluate their individual impact on MS and other magnetic parameters, lithology-specific rock magnetic property data including IRM acquisition curves were derived from extracted, petrologically classified IRD dropstones and granules. Interestingly, 16 of the 22 IRD lithologies have lower and only 6 have higher MS than 'background sediment' (sediment with no or very little IRD). Of these few 'MS enhancers', only 'Canadian Shield' muscovite-biotite granite IRD with its fourfold above background MS, high coarse magnetite content ($B_{1/2} = 29 \text{ mT}$, $\text{SIRM}/\chi = 440$), and high abundance in HLs (second only to low-magnetic ooid-bearing dolomite) qualifies as the 'hidden champion' in the (magnetic) opposition of calcareous and magmatic IRD. Granite IRD counts and two 'total granite proxies', $\text{IRM}_{20\text{mT}}$ and K/Fe, attest that granitic material was also deposited during IRD-free periods between HEs, while ooid-bearing dolomite IRD, in contrast to sucrosic dolomite IRD (!), appears to be indeed highly specific of HE layers.

MS like other rock magnetic parameter records reacts to IRD input, but lack specificity for HE. The highs and lows of MS are multifactorial and defy simple unidirectional interpretations. Furthermore, MS signal spikes may reflect the randomness of coarse IRD distribution in the sediment column and are therefore of limited stratigraphic value. Given, that a major part of IRD particles is hidden in the unclassifiable silt and fine sand grain-size fractions, that various transport mechanisms for detrital fractions existed throughout the Late Pleistocene glaciation of northern North America, and that all of these transport chains were nourished by (at least geologically) similar subglacial provenance regions, there is little hope for an unequivocal quantitative interpretation of glaciomarine magnetic records, in particular with the limited perspective of a single core site. The sedimentological ambiguity of MS logs does not question their stratigraphic suitability for core-to-core correlations in the North Atlantic realm, but it bears high risks to base a HE stratigraphy exclusively on MS variations. The Ca/Sr ratio is safer as it distinguishes HE events from similarly large IRD releases during Last Glacial Maximum.

3.7 Acknowledgements

SB wishes to gratefully acknowledge the financial support enabling his thesis project, composed of a promotion stipend from the Petroleum Technology Development Fund (PTDF), Nigeria, and complementary research funding by the DFG International Research Training Group 'Process and impact of climate change in the North Atlantic Ocean and the Canadian Arctic' (ArcTrain, Germany) for travel, consumables and measurements. We thank the crew and scientific team of RV Maria S. Merian cruise MSM39 for their support during. We also appreciate laboratory assistance by Liane Brück, Thomas Frederichs and Christian Hilgenfeldt.

3.8 References

- Andrews, J. T., & Tedesco, K. (1992). Detrital carbonate-rich sediments, northwestern Labrador Sea: Implications for ice-sheet dynamics and iceberg rafting (Heinrich) events in the North Atlantic. *Geology*, 20(12), 1087. [https://doi.org/10.1130/0091-7613\(1992\)020<1087:DCRSNL>2.3.CO;2](https://doi.org/10.1130/0091-7613(1992)020<1087:DCRSNL>2.3.CO;2)
- Badesab, F., von Dobeneck, T., Briggs, R. M., Bryan, K. R., Just, J., & Müller, H. (2017). Sediment dynamics of an artificially deepened mesotidal coastal lagoon: An environmental magnetic investigation of Tauranga Harbour, New Zealand. *Estuarine, Coastal and Shelf Science*, 194, 240–251. <https://doi.org/10.1016/j.ecss.2017.06.017>
- Bond, G., Heinrich, H., Broecker, W., Labeyrie, L., McManus, J., Andrews, J., et al. (1992). Evidence for massive discharges of icebergs into the North Atlantic ocean during the last glacial period. *Nature*, 360(6401), 245–249. <https://doi.org/10.1038/360245a0>
- Bond, G. C., & Lotti, R. (1995). Iceberg Discharges into the North Atlantic on Millennial Time Scales During the Last Glaciation. *Science*, 267(5200), 1005–1010. <https://doi.org/10.1126/science.267.5200.1005>
- Broecker, W., Bond, G., Klas, M., Clark, E., & McManus, J. (1992). Origin of the northern Atlantic's Heinrich events. *Climate Dynamics*, 6(3), 265–273. <https://doi.org/10.1007/BF00193540>
- Domack, E. W., & Powell, R. (2018). Chapter 7 - Modern Glaciomarine Environments and Sediments: An Antarctic Perspective. In J. Menzies & J. J. M. van der Meer (Eds.), *Past Glacial Environments (Second Edition)* (pp. 181–272). Elsevier. <https://doi.org/10.1016/B978-0-08-100524-8.00030-0>
- Egli, R. (2003). Analysis of the field dependence of remanent magnetization curves. *Journal of Geophysical Research: Solid Earth*, 108(B2). <https://doi.org/10.1029/2002JB002023>
- Grousset, F. E., Labeyrie, L., Sinko, J. A., Cremer, M., Bond, G., Duprat, J., et al. (1993). Patterns of Ice-Rafted Detritus in the Glacial North Atlantic (40–55°N). *Paleoceanography*, 8(2), 175–192. <https://doi.org/10.1029/92PA02923>
- Grousset, Francis E., Cortijo, E., Huon, S., Hervé, L., Richter, T., Burdloff, D., et al. (2001). Zooming in on Heinrich layers. *Paleoceanography*, 16(3), 240–259. <https://doi.org/10.1029/2000PA000559>
- Heinrich, H. (1988). Origin and Consequences of Cyclic Ice Rafting in the Northeast Atlantic Ocean During the Past 130,000 Years. *Quaternary Research*, 29(2), 142–152. [https://doi.org/10.1016/0033-5894\(88\)90057-9](https://doi.org/10.1016/0033-5894(88)90057-9)
- Kruiver, P. P., Dekkers, M. J., & Heslop, D. (2001). Quantification of magnetic coercivity components by the analysis of acquisition curves of isothermal remanent magnetisation. *Earth and Planetary Science Letters*, 189(3), 269–276. [https://doi.org/10.1016/S0012-821X\(01\)00367-3](https://doi.org/10.1016/S0012-821X(01)00367-3)
- Leng, W., von Dobeneck, T., Bergmann, F., Just, J., Mulitza, S., Chiessi, C. M., et al. (2018). Sedimentary and rock magnetic signatures and event scenarios of deglacial outburst floods from the Laurentian Channel Ice Stream. *Quaternary Science Reviews*, 186, 27–46. <https://doi.org/10.1016/j.quascirev.2018.01.016>
- Leng, W., von Dobeneck, T., Just, J., Govin, A., St-Onge, G., & Piper, D. J. W. (2019). Compositional changes in deglacial red mud event beds off the Laurentian Channel reveal

- source mixing, grain-size partitioning and ice retreat. *Quaternary Science Reviews*, 215, 98–115. <https://doi.org/10.1016/j.quascirev.2019.04.031>
- Max, L., Nürnberg, D., Chiessi, C. M., Lenz, M. M., & Mulitza, S. (2022). Subsurface ocean warming preceded Heinrich Events. *Nature Communications*, 13(1), 4217. <https://doi.org/10.1038/s41467-022-31754-x>
- Maxbauer, D. P., Feinberg, J. M., & Fox, D. L. (2016). MAX UnMix: A web application for unmixing magnetic coercivity distributions. *Computers & Geosciences*, 95, 140–145. <https://doi.org/10.1016/j.cageo.2016.07.009>
- McCave, I. N., Manighetti, B., & Robinson, S. G. (1995). Sortable silt and fine sediment size/composition slicing: Parameters for palaeocurrent speed and palaeoceanography. *Paleoceanography*, 10(3), 593–610. <https://doi.org/10.1029/94PA03039>
- Mulitza, S., Bergmann, F., Brück, L., Chiessi, C. M., Govin, A., Klann, M., et al. (2015). Cruise No. MSM39 - June 07-June 25, 2014 - St. John's (Canada) - St. John's (Canada) (Version 1.0) [Application/pdf]. MARIA S. MERIAN-Berichte (p. 89 pages). DFG-Senatskommission für Ozeanographie. https://doi.org/10.2312/CR_MSM39
- Mullender, T. A. T., Frederichs, T., Hilgenfeldt, C., de Groot, L. V., Fabian, K., & Dekkers, M. J. (2016). Automated paleomagnetic and rock magnetic data acquisition with an in-line horizontal “2G” system. *Geochemistry, Geophysics, Geosystems*, 17(9), 3546–3559. <https://doi.org/10.1002/2016GC006436>
- Peters, C., Walden, J., & Austin, W. E. N. (2008). Magnetic signature of European margin sediments: Provenance of ice-rafted debris and the climatic response of the British ice sheet during Marine Isotope Stages 2 and 3. *Journal of Geophysical Research: Earth Surface*, 113(F3). <https://doi.org/10.1029/2007JF000836>
- Piper, D. J. W., & DeWolfe, M. (2003). Petrographic evidence from the eastern Canadian margin of shelf-crossing glaciations. *Quaternary International*, 99–100, 99–113. [https://doi.org/10.1016/S1040-6182\(02\)00115-5](https://doi.org/10.1016/S1040-6182(02)00115-5)
- Rashid, H., Saint-Ange, F., Barber, D. C., Smith, M. E., & Devalia, N. (2012). Fine scale sediment structure and geochemical signature between eastern and western North Atlantic during Heinrich events 1 and 2. *Quaternary Science Reviews*, 46, 136–150. <https://doi.org/10.1016/j.quascirev.2012.04.026>
- Rashid, Harunur, Hesse, R., & Piper, D. J. W. (2003). Evidence for an additional Heinrich event between H5 and H6 in the Labrador Sea: HEINRICH EVENT 5A IN THE LABRADOR SEA. *Paleoceanography*, 18(4), n/a-n/a. <https://doi.org/10.1029/2003PA000913>
- Razik, S., Dekkers, M. J., & von Dobeneck, T. (2014). How environmental magnetism can enhance the interpretational value of grain-size analysis: A time-slice study on sediment export to the NW African margin in Heinrich Stadial 1 and Mid Holocene. *Palaeogeography, Palaeoclimatology, Palaeoecology*, 406, 33–48. <https://doi.org/10.1016/j.palaeo.2014.04.009>
- Roberts, A., Almeida, T., Church, N., Harrison, R., Heslop, D., Li, Y., et al. (2017). Resolving the Origin of Pseudo-Single Domain Magnetic Behavior: Origin of PSD Behavior. *Journal of Geophysical Research: Solid Earth*, 122. <https://doi.org/10.1002/2017JB014860>
- Robertson, D. J., & France, D. E. (1994). Discrimination of remanence-carrying minerals in mixtures, using isothermal remanent magnetisation acquisition curves. *Physics of the*

- Earth and Planetary Interiors, 82(3–4), 223–234. [https://doi.org/10.1016/0031-9201\(94\)90074-4](https://doi.org/10.1016/0031-9201(94)90074-4)
- Robinson, S. G. (1986). The late Pleistocene palaeoclimatic record of North Atlantic deep-sea sediments revealed by mineral-magnetic measurements. *Physics of the Earth and Planetary Interiors*, 42(1), 22–47. [https://doi.org/10.1016/S0031-9201\(86\)80006-1](https://doi.org/10.1016/S0031-9201(86)80006-1)
- Robinson, S. G., Maslin, M. A., & McCave, I. N. (1995). Magnetic susceptibility variations in Upper Pleistocene deep-sea sediments of the NE Atlantic: Implications for ice rafting and paleocirculation at the Last Glacial Maximum. *Paleoceanography*, 10(2), 221–250. <https://doi.org/10.1029/94PA02683>
- Ruddiman, W. F. (1977). Late Quaternary deposition of ice-rafted sand in the subpolar North Atlantic (lat 40° to 65°N). *GSA Bulletin*, 88(12), 1813–1827. [https://doi.org/10.1130/0016-7606\(1977\)88<1813:LQDOIS>2.0.CO;2](https://doi.org/10.1130/0016-7606(1977)88<1813:LQDOIS>2.0.CO;2)
- Stoner, J. S., Channell, J. E. T., & Hillaire-Marcel, C. (1996). The magnetic signature of rapidly deposited detrital layers from the Deep Labrador Sea: Relationship to North Atlantic Heinrich layers. *Paleoceanography*, 11(3), 309–325. <https://doi.org/10.1029/96PA00583>
- Telford, W. M., Geldart, L. P., & Sheriff, R. E. (1990). *Applied Geophysics* (2nd ed.). Cambridge University Press. <https://doi.org/10.1017/CBO9781139167932>
- Tjallingii, R., Röhl, U., Kölling, M., & Bickert, T. (2007). Influence of the water content on X-ray fluorescence core-scanning measurements in soft marine sediments. *Geochemistry, Geophysics, Geosystems*, 8(2). <https://doi.org/10.1029/2006GC001393>
- Wang, Y. (2016). Magnetic characteristics of Newfoundland Margin sediments: Provenance of ice-rafted debris in Heinrich Event layers. Master Thesis, 81 p. Faculty of Geosciences, University of Bremen, Germany.
- Wheeler, J.O., Hoffman, P.F., Card, K.D., Davidson, A., Sanford, B.V., Okulitch, A.V., and Roest, W.R., 1996. Geological map of Canada / Carte géologique du Canada; Geological Survey of Canada, Map 1860A. doi:10.4095/208175

Chapter 4: Imprint and Assessment of Random Deposition and Lithological Variability of Ice-rafted Debris (IRD) in Magnetic Susceptibility Records

S. Bukar^{1*}, T. von Dobeneck^{1,2}, T. Frederichs¹, Y. Wang¹, G. St-Onge³

¹ Faculty of Geosciences, University of Bremen, Bremen, Germany

² MARUM-Center for Marine Environmental Sciences

³ Institut Sciences de la mer de Rimouski ISMER, Canada Research Chair in Marine Geology, Université du Québec à Rimouski and GEOTOP, Canada

Abstract

Magnetic susceptibility (MS) logs of Late Pleistocene North Atlantic glaciomarine sediments are usually pronounced and varied owing to the large manifold of ice-rafted detritus (IRD) of diverse lithologies with low to high magnetite concentration, that are deposited randomly in the stratigraphic sequence. The application of diverse MS techniques to whole core, split core, and discrete cube samples of a sedimentary core, retrieved at the foot of the Grand Banks slope of Newfoundland, revealed partly dissimilar MS signals, mirroring the stochastic nature of IRD deposition. While conventional techniques of MS logging allow only uniaxial MS logging, we demonstrate here a new non-destructive multi-track method of across core MS scanning, where a step motor moves a MS2E high-resolution spot-sensor in steps over the full split-core surface. This novel protocol permits the mapping and visualization of IRD distribution and lithological variability. It allows to quantify the lateral magnetic heterogeneity within sediment layers in terms of statistic deviation from a median value, which varies systematically with IRD content. The very different volume averaging defined by the susceptometer coil geometry plays a crucial role particularly with glaciomarine sediments: the large measuring volumes of whole core loop sensors underplay the randomized micro-scale IRD distribution in a glaciomarine sediment column. In contrast, single-sample MS records of discrete volumes bearing coarse-grained IRD overemphasize the spread of IRD due to the sparse nature of the sediment samples.

Key Points:

- IRD-enriched event layers in glaciomarine sediments can be efficiently detected by their typical spiky signal maxima in high-resolution magnetic susceptibility records.
- Full-core loop-sensor logging and discrete-sample bulk-sensor magnetic susceptibility measurements average, but do not recognize lateral sediment heterogeneity by IRD.
- The randomized distribution and lithological diversity of coarse-grained IRD can be detected and visualized by our new spot-sensor multi-track MS scanning approach.

4.1 Introduction

The studies of Radhakrishnamurty et al. (1968) and Kent (1982) established the method of correlating sediment series by rock magnetic signals, in particular magnetic susceptibility (MS). MS logging of whole or split cores is a non-destructive, fast, and simple technique, which, due to its efficacy, has been widely applied in past decades. Many studies (Bloemendal & deMenocal, 1989; Grousset et al., 1993; Robinson, 1986, 1993; Robinson et al., 1995) have used MS and other rock magnetic parameters to discern lithologic units and correlate stratigraphic sequences within Late Pleistocene glaciomarine sediments. As the MS signal is controlled by magnetic mineral content, terrigenous sediment sources, transport partitioning, dilution by low-magnetic biogenic components, and under certain conditions also diagenetic processes govern the intensity and character of the MS signal.

Throughout the colder Quaternary periods, subpolar and mid-North Atlantic sediments in the so-called „Ruddiman Belt“ received changing amounts of ice-rafted detritus (IRD) from calving or collapsing continental ice sheets (Broecker, 1994; Small et al., 2013). The most massive IRD deposition occurred during so-called Heinrich Events (HE), attributed to catastrophic collapses of the Laurentian Ice Sheet (LIS), which formed IRD-rich „Heinrich Layers“ (HL, Broecker et al., 1992; Heinrich, 1988) during the Late Wisconsinan period. IRD fragments cover a wide range of grain sizes from silt to gravel, where the finer fragments are quantitatively more abundant, but much harder to separate and petrologically identify than the coarse >1 mm „IRD fraction“ (Hemming, 2004; Bukar et al., Chapter 2). While the far more numerous silt-sized glaciomarine particles should be rather uniformly distributed in the sediment, the deposition of coarse sand- to gravel-sized IRD particles („dropstones“) becomes increasingly stochastic. Consequentially, the distribution of the coarser IRD particles in the sediment column is vertically and laterally heterogeneous as reflected by count statistics (Chapter 2) and bulk sediment radiographs.

The composition and the proportion of IRD deposition in a marine basin largely depend on past glacial dynamics, ocean currents and temperatures, as well as the spread of terrigenous geologic materials within the iceberg matrix. The uptake of terrigenous materials in ice is governed by bedrock relief and hardness as well as the thermal condition of the basal ice sheet (Alley & MacAyeal, 1994). Ice-entrained and -embedded detrital materials are usually concentrated in a 1 to 3 m thick „dirty ice“ layer at the bottom of an iceberg (Andrews, 2000). The ultimate deposition of the IRD is inherently random owing to varying iceberg trajectories and sediment loads (Andrews, 2000). This leads to the formation of detrital-rich layers that are typified by lateral variations in lithology. On top of that, IRD particles originate from rocks and rock-forming minerals of diverse petrology and provenance (Piper & DeWolfe 2003). The petrographic and petrological study of sand-sized (>1 mm) IRD (Chapter 2) classified 22 distinct lithologies throughout HLs H1 - H6 in a sediment core from the SE Grand Bank Slope of Newfoundland. This overtly gives a hint of the variability of the magnetic mineral composition in IRD-rich deposits. Based on the aforementioned, MS logging of high-latitude sediment core samples should not be expected to lead to highly consistent records. This raises the question, if and how MS logging techniques can account for lateral lithological variability in IRD-rich sediment cores.

Volume MS (κ) records of marine sediment cores can be alternatively acquired from whole cores (with loop sensors), split cores (with spot sensors), or discrete samples (with bulk sensors), creating κ logs of greatly disparate spatial resolution. Some past studies may have

had a lack of awareness that the desirable gain in stratigraphic (vertical) resolution obtained by reducing the sensing volume is traded in for enhanced signal noise due to lateral sediment inhomogeneity. For obvious reasons, whole-core and discrete sample MS logging methods can only produce a singular κ log without any possibility of statistical verification, since multiple coring of one coring site or multiple sampling of a single core is usually forbidden by scientific policies. Only the spot sensor method principally allows to obtain several distinct and (partly) independent κ logs from a single split core by logging along multiple parallel sensor tracks.

This approach can be automated and expanded into MS scanning (or imaging) of a complete split core surface, permitting to assess and quantify lateral MS variability as an expression of (stochastic/random) sediment heterogeneity. Quantifying the resulting stratigraphic uncertainty is particularly relevant for glaciomarine and hemipelagic sediment. Similarly, conventional MS logs of glaciomarine sediments are usually presented without explicitly accounting for the volume-averaging effect of the MS sensors. MS signal amplitudes and patterns are treated more as expressions of sediment history than of random IRD distribution and MS logging techniques (Grousset et al., 1993; Robinson et al., 1995).

In this study, we intend to elucidate and highlight the discrepancies between the three main MS logging methods and show how lateral variability in sediment lithology can be assessed by spot-sensor MS scanning. Such will be achieved by addressing the following questions:

1. How do MS records of glaciomarine sediments differ in dependence of MS sensor types and in which ways are they affected by IRD content and distribution?
2. Can multi-track spot-sensor MS scanning of split cores depict, quantify and reduce the stochasticity of IRD distribution while preserving high vertical resolution?
3. How do MS logs and scans relate to the MS of the extracted coarse IRD fraction and to sedimentological IRD and HE records such as IRD counts and Ca/Sr logs?

4.2 Materials and Methods

4.2.1 Materials

All data presented here are from gravity core GeoB18530-1, acquired in 2014 at the southeastern Grand Banks slope of Newfoundland by RV Maria S. Merian expedition MSM39 (Mulitza et al., 2015). Over a total length of 10.7 m, this core provides a continuous and complete stratigraphic record of the latest six HLs H1-H6 followed by deglacial and Holocene successions (Mulitza et al., 2015; Chapter 2). Detailed chronostratigraphy, petrological analysis, rock magnetic and geochemical investigations of this IRD-rich core have been undertaken by Bukar et al. (Chapter 2), where protocols of discrete cube sample analyses as well as some granulometric analyses relevant for the present study can be found. The herein newly introduced MS spot-sensor scanning method has not just been applied to GeoB18530-1, but also to five other proximal cores, namely GeoB18531-1, 18534-1, 18554-1, 18556-1, and 18558-1. Since similar results were obtained for all six cores, only the records of GeoB18530-1 are shown here, as this core was better pre-investigated with other methods and all the other records would not substantially add to the aims of this methodological study.

4.2.2 Methods

Whole-core MS logging of core GeoB18530-1 was conducted onboard during the MSM39 cruise (Mullitz et al., 2015), while discrete sample MS data were acquired in the magnetic laboratory of the marine geophysics group at the University of Bremen as presented in Chapter 2. The respective records will be shown here for comparison with MS spot sensor imaging. We will once again specify the instrumental setup and experimental protocol in greater detail than previously published for better documentation of methodical differences and outcomes. The impact of MS sensor response functions is further explained in Chapter 3. We refer to the methods sections of both these chapters for experimental procedures used to create the herein reproduced data, i.e. color scans, element logs, and IRD counts,

4.2.2.1 Whole-Core MS Logging

Whole-core MS was logged onboard with an automated *GEOTEK* multi-sensor core logger (MSCL). Logging of the 120 mm wide, segmented, yet unopened gravity core was performed in 2 cm steps with a *Bartington MS2C* 140 mm loop sensor. Due to the sensor's large diameter, its sensitive volume extends sideways with a half-width of about 8 cm. Sharp, pronounced changes in MS signature hence appear smoothed and thin, magnetically contrasting layers or particles are not individually resolved. For segment end correction and temperature drift compensation, void, non-magnetic spacer were placed between segments during the *GEOTEK*-style logging, in which segments are being advanced by the push of the follow-up segment. Linear instrumental temperature drift correction was performed using the value taken at the center of the spacer cylinder. In the post-processing, the spacer sections were removed and the systematic MS signal decrease at the core segment boundaries was reclaimed by summing up the two overlapping tail data, while the core top and bottom were mirror-corrected. This non-standard logging procedure efficiently eliminates drift error under unstable temperature conditions aboard and avoids data loss or deterioration over the segment boundaries.

4.2.2.2 Split-Core MS Scanning

Split-core scanning was realized with a custom-built stationary laboratory split-core logger at the University of Bremen magnetism lab. This table-top logger was optimized for high-resolution, high-precision MS logging of archive halves, e.g. for cyclostratigraphy, time series, and facies analysis. Three separate stepper motor drives make it possible to automatically move the core half longitudinally, and to lower and raise as well as transversely move the *Bartington* point sensors in a distance-controlled manner. The fixation of the spot sensor on the lever arm has been constructed as a gimbal to allow the sensor bottom to adjust its angle within $\sim 10^\circ$ to the possibly not perfectly level core surface. The (optional) MS2F and MS2E sensors therefore always measure in tight contact with the flat and smooth sediment surface, thereby achieving much higher spatial resolution than the loop sensors of MSCL systems. The half-widths of MS2F and MS2E sensor characteristics are ~ 3 cm and 1.5 cm, respectively; their vertical reach is even lower. Every single measurement at the core surface is supplemented by a subsequent air measurement to dynamically correct the rather high-temperature drift of spot sensors. It takes 20 minutes to log a 1 m long core segment along a single track in 1 cm steps. Operating the system in the scanning mode with nine parallel sensor tracks over a 12 cm wide half-core (avoiding the more critical edge tracks) will accordingly require 3 hours per segment.

The well-preserved and largely intact archive halves of sediment core GeoB18530-1 were taken from the cold core repository and allowed to warm up to room temperature overnight to avoid excessive temperature drift. The sediment surfaces were carefully stripped with a clean, non-magnetic scrapper to ascertain direct contact between sediment and sensor and to avoid air gaps. The still slightly moist sediment surfaces were clad with transparent, ~0.02 mm thick saran wrap to exclude sensor contamination. The negligible thickness of this film does not affect the sensor's scale factor, while for thicker films, signal reduction must be considered. MS imaging was performed by measuring successive along-core tracks in 1 cm increments and with 1 cm track distance, so that an equidistant 1 cm x 1 cm MS data grid over the central 98 cm x 8 cm of each 100 cm x 12 cm segment surface was obtained.

4.2.2.3 Discrete Sample MS Measurement

Discrete sample MS records of core GeoB18530-1 have been collected for two sample series, "paleomagnetic" wet-bulk cube samples of 6.2cm³ volume, and IRD >1 mm sieve fractions from 10 ml syringe samples. Both samples series were collected in parallel every 2 cm along the lower 550 – 1050 cm core section corresponding to MIS 3 and 2. The cube samples were measured with a *Bartington* MS2B bulk sensor and MS3 control unit in the low-frequency (0.465 kHz) mode and are volume- and sample-holder corrected. The coarser sieve fractions were measured in small, non-magnetic pharmaceutical capsules with the more sensitive *Agico KappaBridge KLY-2* susceptometer, operating at a frequency of 920 Hz, using predominantly the most sensitive range 1 (0.05·10⁻⁶ SI). Great care was taken to correct for all magnetic influences of sample containers and holders before mass-normalization.

4.3 Instrumental Implications and Improvements of MS Data Acquisition

4.3.1 MS Sensor Response Functions

MS signal variations of sedimentary sequences depend on the concentration variations of iron-bearing ferrimagnetic minerals, especially magnetite and other minerals of the iron-titanium solid solution series (Zolitschka et al., 2002). The MS signals engendered by the three MS logging techniques described here are of different quality and relevance in various phases of sediment core investigation (Nowaczyk, 2002; Zolitschka et al., 2002). The distinction of the alternative MS logs results from the disparate geometric sensor attributes, where each sensor type averages and integrates over the sediment's complex microscale susceptibility distribution with a sensor-specific and non-linear sensitivity-distance decline. This sometimes imprecisely named "sensitive volume" can be mathematically described and numerically simulated by each sensor's spatial response function.

The uniaxial loop and spot sensor response function measurement conducted by Nowaczyk (2002) used a thin, circular disc (in size corresponding to core diameter) covered by magnetite. As the round or half-disc is moved into (or out of) the sensor sensitivity region, it reveals the weighting function of both core logging techniques assuming a laterally homogenous sediment. The broad bell-shaped response function of the loop sensor (Figure 1) demonstrates that a large volume of the core is being magnetized by the sensor's alternating magnetizing field, which also contributes to the measured MS signal (or physically speaking, the resulting inductivity change of the coil) with axially declining impact. By extension, a whole core can be considered as being

composed of a succession of discs with different magnetic susceptibilities. The axial response function thus provides the weighting coefficient for each disc (a function of its distance from the sensor plane) within the integral MS signal. In other words, the recorded MS signal κ_m at point x_p (Fig. 1) is the integral over the core's entire susceptibility distribution $\kappa(x)$ multiplied by the sensor response function $s(x - x_p)$ over its (reasonably) sensitive range x_a to x_b , which can be mathematically expressed as a convolution

$$\kappa_m(x_p) = \int_{x=x_a}^{x=x_b} \kappa(x) s(x - x_p) dx \quad (\text{Eq. 1})$$

This expression can be regarded as a weighted running mean of the real susceptibility along the core axis, where the whole-core loop sensor acts as a low-pass filter (Nowaczyk, 2002).

The along-core response function of spot-sensor logging is nearly identical to the loop sensor's, but narrower (figure 1b) in width. In addition, the vertical reach of the spot sensor is also more limited so that material, that is closer to the sensor foot, has much larger influence for the measurement (MS2F sensor: 100% at sensor bottom, 10% at 6 mm distance; MS2E1 sensor: 100% at 0 mm, 50% at 1 mm, 10% at 3.5 mm, see *Bartington* manual). Spot sensors hence neglect the material at depth and only represent the MS distribution of the shallow subsurface.

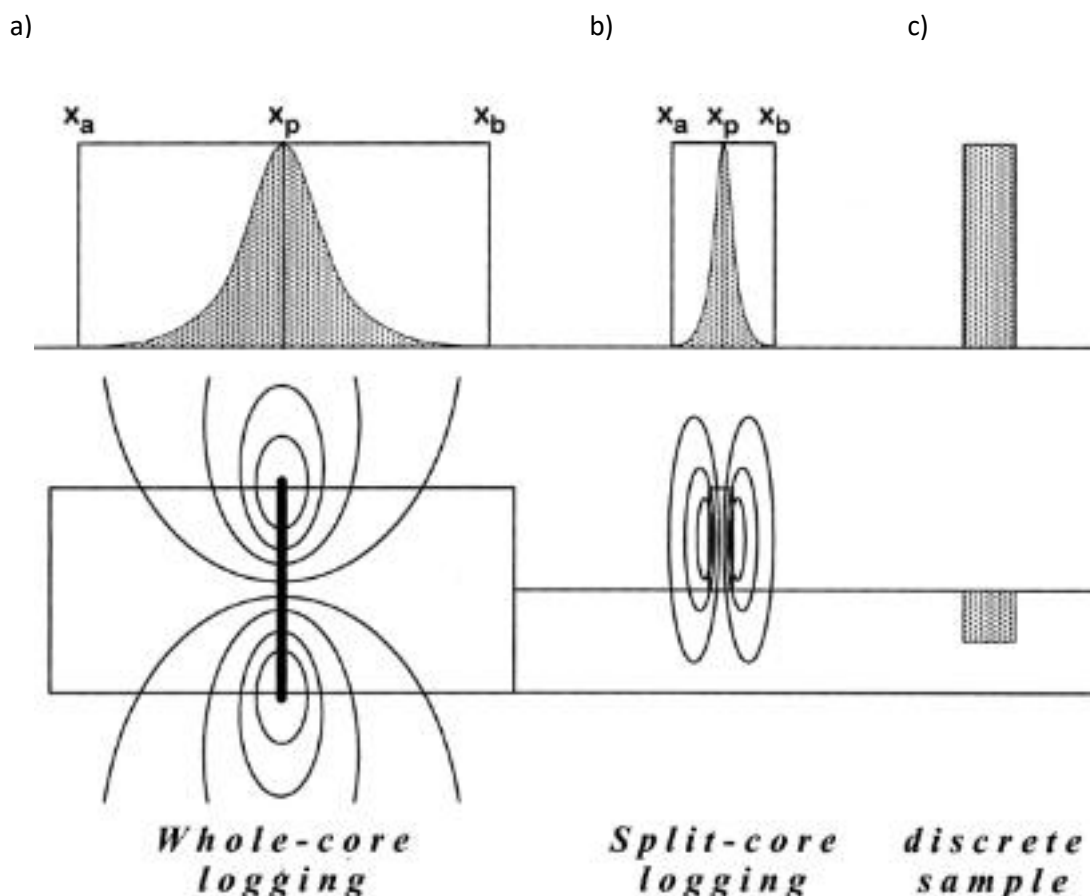


Figure 1: A schematic view of material volume (half-disc covered with magnetite) influenced by the magnetic field of different sensor characteristics (Nowaczyk, 2002). The sensitivity of the uniaxial whole and split core weighting function tapers gradually from an initial bell-shaped characteristic to zero (from x_p to either x_a or x_b) as the range distance of material logged and instrument sensor is increased. The geometry of the discrete sample response function is mainly rectangular.

Laterally heterogeneous (e.g. glaciomarine) sediments cannot be mathematically represented by the idealized (half-) disc of (Nowaczyk, 2002). For such materials, it would be necessary to establish triaxial response functions, that take the shape of a 3D-matrix $s(x - x_s, y - y_s, z - z_s)$, where (x, y, z) denotes the discrete location of each (infinitesimal) sediment volume element and (x_s, y_s, z_s) the position of the sensor bottom center. For a surface measurement ($z = 0$) over a split-core of radius r (i.e. $\kappa(y^2 + z^2 > r^2) = 0$), we would then get the volume integral

$$\kappa_m(x_s, y_s, 0) = \int_{x=x_a}^{x=x_b} \int_{y=-r}^{y=r} \int_{z=-r}^{z=0} \kappa(x, y, z) s(x - x_s, y - y_s, z) dx dy dz \quad (\text{Eq. 2})$$

For the radially symmetrical MS2F spot sensor, experimental mapping of this point response function should be simpler, as it would be sufficient to map the MS signal of a discrete magnetic particle that is being systematically moved over the central half-plane below the sensor. As the coil of the MS2E spot sensor is elliptical, it would be necessary to map the entire half-space below the sensor in equally high resolution. Such point response function have not been made digitally available by the producer of the sensors. It would be useful to acquire these data to numerically simulate MS measurement of digitally created IRD particle distributions, but the technical effort to reach sufficient experimental precision and resolution has been keeping us so far away from engaging into this exercise.

However, it directly follows from equation 2, that a spot sensor MS record acquired along a random ship track line over a likewise randomly determined core position yields just one out of a nearly infinite number of diverging MS logs if sediment exhibits lateral compositional inhomogeneity. Mapping the MS over a split core surface is better than a single measurement, but still covers only a small part of the entity of potentially obtainable curves around a given core location. Nevertheless, the statistical variance within parallel MS tracks should at least scale with the statistical variance of the population of all the other hypothetical MS tracks and appears therefore as the only feasible approach to an otherwise unfeasible task.

4.3.2 Comparison of MS Records by Different Logging Techniques

The color line-scan image (Figure 2) of the lower section (550 – 1050cm) of core GeoB18530-1 is composed of six distinct HL units denoted as H1-H6. These vary in thickness and are sandwiched between hemipelagic interlayer units with sharp to gradual mutual contacts. The interlayer units are typified by clayey dark-olive-grey facies units (I1-I5 with abridged I6) that dominate when HE processes are in quiescence phases. The light pigmentation of the HL facies is attributed to detrital carbonate and other light-colored IRD originating from Paleozoic limestone and dolostone of Hudson Bay and Hudson Strait (Broecker et al., 1992).

For stratigraphic correlation, all studied cores were tied onto the same lithological scaling based on high-resolution XRF-scan-based Ca/Sr ratios. The Ca/Sr ratio has been repeatedly used as an HL marker as the detrital carbonate has a much higher Ca/Sr ratio than modern marine carbonate so that values alternate between well separable levels (Chapter 2). As the adjacent IRD > 1mm count records evidences, an enhanced HE-related IRD deposition began before and ended after the Ca/Sr-based layer limits. Continuously high IRD contents over interlayers I1 and I2 imply a higher influx of detrital material during LGM times. The IRD >1 mm content of the HLs showcases an increase toward the later event layers (H1 and H2). The earlier HLs H4 – H6 are instead more distinct relative to the interlayers than the later.

Figure 2 also highlights, that the IRD deposition history as documented by the IRD >1 mm counts bears more resemblance to the three different MS signals at its right than to the Ca/Sr HE proxy at its left. As explained by Bukar et al. (Chapter 2), dolomitic IRD seems to be characteristic only for the mid-phase of a HE, while granitic IRD prevails in early and late HE phases. The cumulative MS signal hence reflects the compensatory balance of low-magnetic dolomite and high-magnetic granite (Chapter 2). One can clearly recognize, that the MS record obtained from the IRD > 1 mm sieve fraction in Figure 2 (far right) is highly randomized and shows little similarity with the bulk sediment MS records; its statistical correlation with any of these records is minute.

Obviously, the 10 cm³ syringe sample series, from which the IRD was extracted, is much too small to quantitatively represent the magnetic diversity and distribution of the IRD > 1 mm population. We must therefore assume, that the resemblance of the IRD counts and the bulk MS records results mostly from associated IRD <1 mm particles which are far more numerous and hence more homogeneously distributed, at least at mm-scales. This interesting observation adverts us to the statistical relevance of adequate sample sizes, which Bukar et al. (Chapter 2) already note, but without presenting a MS spot sensor record.

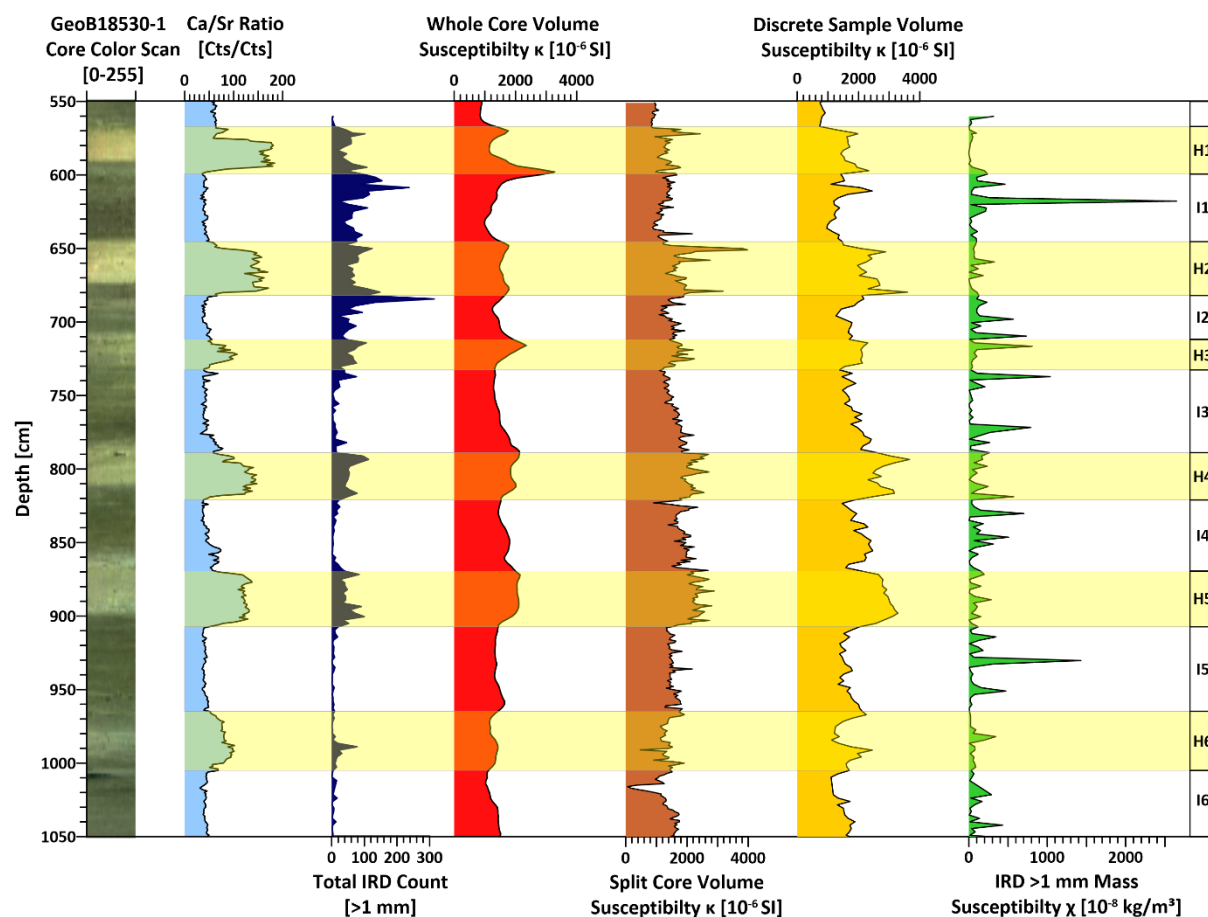


Figure 2: MS records of core GeoB18530-1 obtained from various susceptometric measurements showcasing their different sensitivity to the randomness of IRD particles distribution and magnetic mineral concentration. The IRD-rich layer (H1 – H6) boundaries are marked based on the XRF data of the Ca/Sr ratio (yellow bars) while the sandwiched interlayers I1 and I2 represent the Last Glacial Maximum (LGM) and interlayers I3–I6 periods of low IRD deposition. The split-core color scan at left depicts the lighter coloration by fine dolomitic IRD, while the IRD count record only recognizes coarse IRD particles of > 1 mm size.

The three bulk MS records of core GeoB18530-1 obtained by the bulk MS sensors (Figure 2) manifest primarily enhanced MS values in all the HLs. The whole-core signal is comparatively smoother than the discrete sample and surface records as the loop-sensor logging integrates over a much larger sediment volume sample thereby eliminating most of the IRD dispersion random. Nonetheless, even the loop-sensor approach can resolve the characteristic twin-peak MS signal fairly well, i.e. increased MS values at the bottom and top of each HL (Fig. 2) as also reported in literature (e.g. Hodell et al., 2017; Chapter 2). The signature of the spot-sensor is much spikier due to the sensor's higher spatial resolution results in a better spatial discretization and lesser volume averaging. Therefore, Bartington's MS2E1 sensor is the best available technique to capture the randomness of IRD distribution.

The various MS logging signals described above can delineate IRD variability in a stratigraphic column to a certain extent however, much potential detail of MS signals is lost due to the response characteristics of the sensor devices. While being more receptive to random effects, the split-core spot-sensor logging technique can register a great level of detail with considerable ease through high-resolution lateral or horizontal logging of multiple lines. Thus, systematic and random components of IRD distribution can be discriminated to a remarkable extent.

4.3.3 IRD Mapping by Split-Core MS Scanning

The commonly practiced and largely published (in literature) single-line MS logging methods do not account for the horizontal inhomogeneity of the core material. With response function half-widths of ~3 cm and 1.5 cm of the aforementioned MS2F and MS2E spot sensors the horizontal variability should be detectable at the cm-scale. Such heterogeneity could result from coarse and hence randomly distributed IRD particles of diverse lithology, but also from other singularities (dropstones, macrofossils, reduction zones around organic material), from vertical sediment redistribution by burrowing organisms, or from sediments deformation by the coring process itself. Using available MS sensors and core logging systems, parallel line MS logging appears the most viable means of detecting lateral MS variability at the cm-scale.

While even unmodified standard MSCL systems with MS spot sensors should allow to perform such measurements with repetitive manual displacement of the sensor holder, an automated approach is more comfortable, precise, and time-saving. We technically realized across-core measurements by mounting a third motor drive to our existing spot sensor core logger, which laterally displaces the foot of the vertical sensor drive. Together with the longitudinal drive, which moves the split core carrier, all three drive motors have been programmed such that the MS spot sensor now successively tracks parallel lines with selectable lateral offset without any necessity of manual interference. After each single surface measurement, the sensor is uplifted by ~5 cm to reposition the core or sensor base while performing a void measurement for the dynamic temperature drift correction.

Figure 3 depicts all eight spliced MS2E1 sensor track records of core GeoB18530-1 as parallel line plots and derived contour plot. Other than the previous figure, this compilation comprises also the upper core section (0 – 550 cm) representing Bølling-Allerød to Holocene sediments facies. Apart from occasional signal spikes, the separate track records of the IRD-poor upper section are largely similar. In contrast, considerable MS pattern differences can be recognized in the IRD-rich lower section (550 – 1050 cm).

There are gradual differences between them and some signals have pronounced peak amplitudes (up to a factor ~ 4) at certain core depths, while others have reduced values or maintain the same signal (e.g. topmost part of H5 in MS line 1 and 5, Fig. 3). This can be attributed to the inhomogeneity of the glaciomarine sediment, where IRD of different petrology and grain sizes (including large dropstone) were randomly deposited. Enhanced or reduced amplitude signatures indicate the presence or absence of IRD of different magnetic mineral content and grain size in the shallow subsurface.

Since the spot sensor integrates over more than one track width, the resulting gradual track-to-track changes are better recognized by representing the MS data point matrix as a contour plot (Figure 3, right). The contour plot is marked by a color spectrum indicating high (red) and low (blue) MS values by discrete IRD lithologies. This provides an insight into the variability of MS within the sediment instead of the single-line logging configuration where only peaks can be observed. The causes for MS signal highs and lows by averaging whole core MS logging methods should therefore likewise be understood as being at least partially of a random nature. The highly variable magnetic mineral content of various IRD lithologies and grain sizes (Bukar et al., Chapter3) thereby amplifies the effect of the stochastic spatial distribution within the background sediment matrix.

A statistical analysis of the eight parallel spot-sensor tracks is depicted in Figure 4. Here, the data were again reduced to the lower core half (550–1050 cm) to facilitate the comparison of statistical parameters and logging data. Minima and maxima (as depicted by the red and green

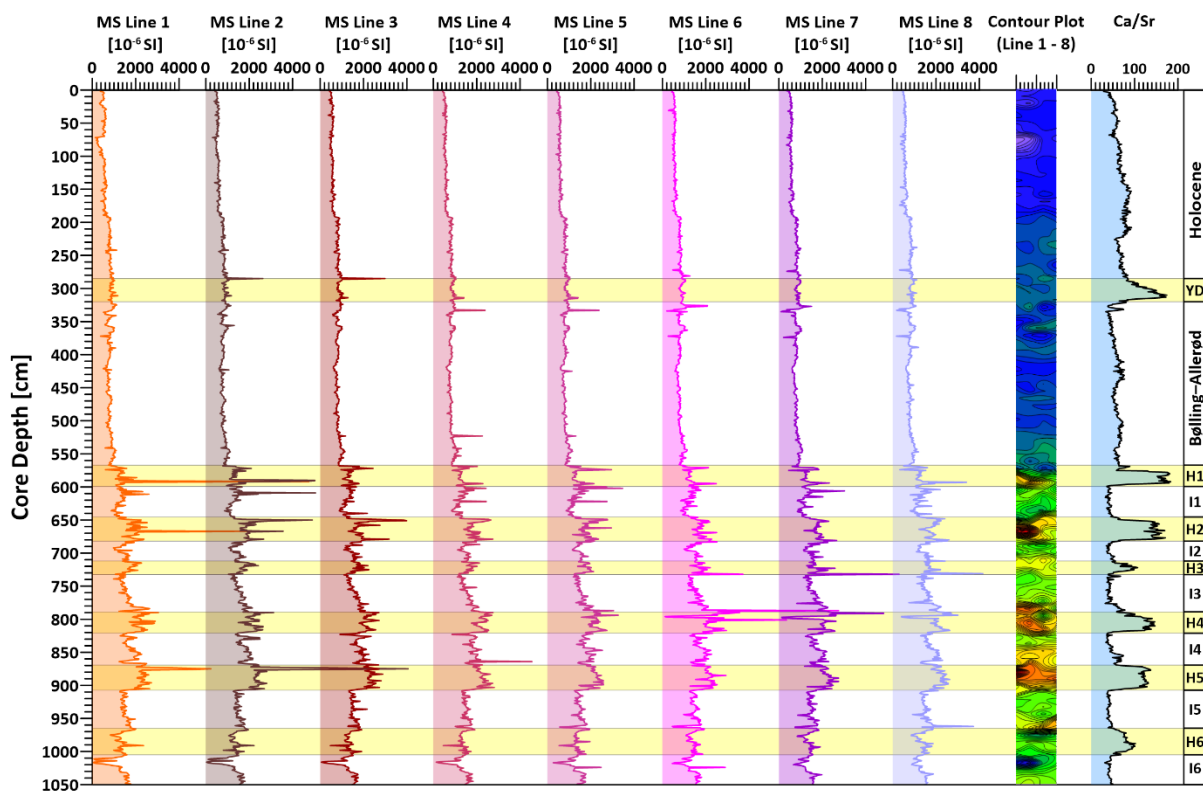
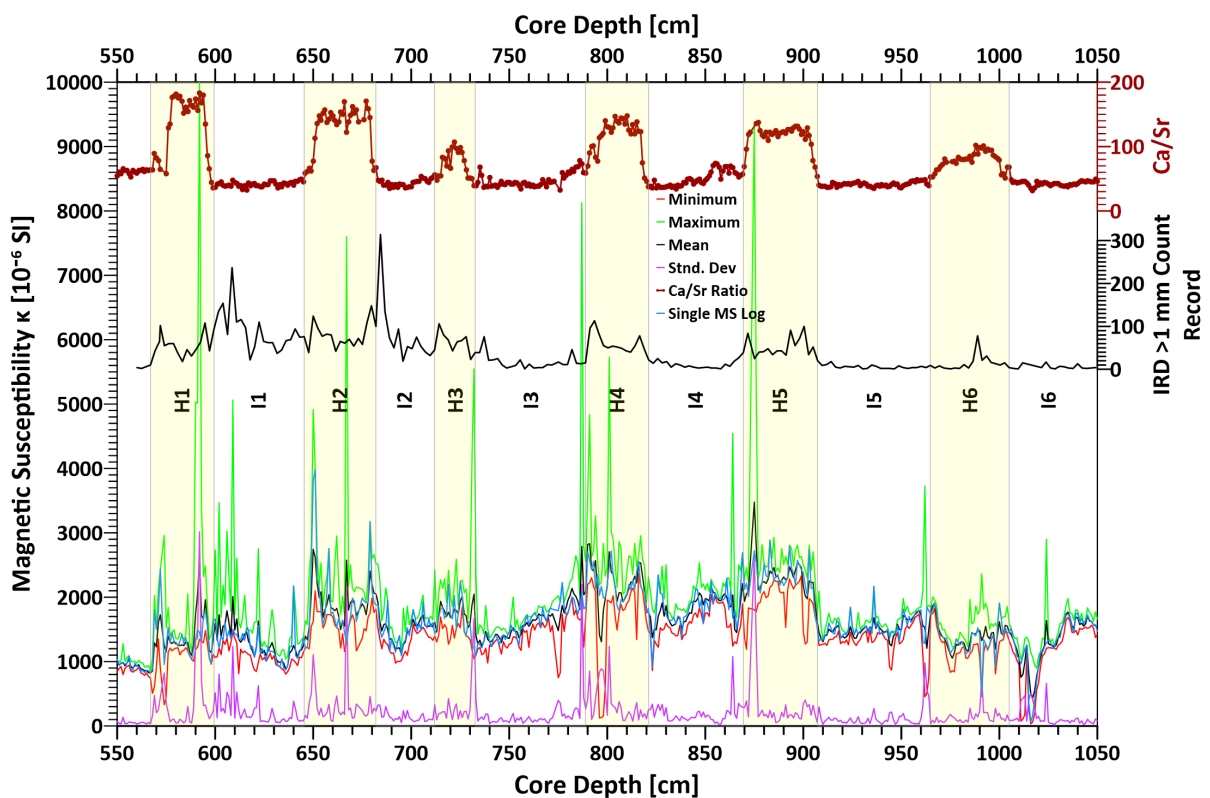


Figure 3: Eight MS track data of core Geob18530-1 displaced in 10 mm steps across the split core diameter; each line was logged with 10 mm increments. The contour plot was generated by using the MS of all the lines acquired. The colors (blue, green, yellow, etc.) reveal the MS concentration of the sediments where the highest MS intensity is depicted in red hue and the lowest is in blue.

lines) of each crossline over eight MS tracts diverge considerably, up to a factor of ~ 7 . The distribution randomness of lithic fragments (IRD) with high or low magnetic mineral content is indicated by high peaks with concurrent low troughs. The mean value record (black line) is not too different from the previously measured single-track record, but being an average, it has a smoother, less spiky appearance; the peak amplitude spread is by a factor of ~ 2 lower. Since any of the eight parallel tracks could have been the initially chosen single-track log, averaging multiple tracks also reduces the “sedimentary” and instrumental noise of the MS record.

Despite individual log discrepancies, the across-core standard deviation of all eight MS values (Figure 4, violet line) remains relatively low throughout the core record. However, due to the lithological and spatial variability in IRD distribution, there are instances, particularly at the granitic IRD-rich boundaries of HE layers, where the standard deviation rises by up to $3 \cdot 10^{-3}$, i.e. to near the values of the cross-core mean. While cross-core variance does not follow the steplike Ca/Sr HL proxy signal (brown line), enhanced MS noise is clearly associated with higher IRD content. In that respect, the statistical scatter of cross-core MS data can account for the presence of IRD, but also for any other possible reason of lateral MS data scatter.



4.4 Conclusions

The signal character of magnetic susceptibility logs and records crucially depends on the sensor characteristics; these determine which sedimentary information and features are accounted for within a stratigraphic sequence. Each MS sensor type resolves the locally stochastic distribution of IRD in a sediment cores in varying detail. Uniaxial whole-core are considerably smoother than the discrete bulk-cube and split-core signal, while none of these resemble the MS record of the extracted IRD > 1 mm. This stems from the averaging design of the loop-sensor and the scarce and randomized presence of IRD particles, respectively. Filtering and smoothing by MS loop sensors resolves long-term changes, but overlooks the random dispersion of IRD by averaging over the micro-scale MS variability. The highly irregular signal of IRM > 1 mm reflects the IRD random spread and variability of IRD lithology and grain size most prominently. MS logs of the split-core surface are similar to discrete bulk-cube sample records, but also depict cm-scale details of IRD distribution as showcased by high frequency spikes.

The MS scans generated from multiple across-core spot-sensor tracks scanning can be transformed into contour plots revealing a detailed IRD distribution and MS intensity map. All the detrital-rich layers (HLs) are typified by more randomized IRD deposition with higher magnetic mineral concentrations as displayed by color contour plots. Multi-track MS scanning also allows to statistically resolve and sensibly average lateral inhomogeneity of a sediment core while preserving high along-core resolution.

4.5 Acknowledgements

SB wishes to extend his deepest gratitude and acknowledge the financial support from the Petroleum Technology Development Fund (PTDF), Nigeria, which made his PhD undertaking and integral research possible. SB appreciates and commends the complementary research funding by the DFG International Research Training Group “Process and impact of climate change in the North Atlantic Ocean and the Canadian Arctic” (ArcTrain) for consumables, instrument time, and travel. Many thanks go to the crew and scientific teams of RV Maria S. Merian cruise MSM39 (2014) for their support. We owe a special thanks and appreciation to the laboratory assistants, namely Liane Brück, Christian Hilgenfeldt, and Heike Piero, at the Marine Geophysics Group, University of Bremen for rendering services whenever needed.

4.6 References

- Alley, R. B., & MacAyeal, D. R. (1994). Ice-rafted debris associated with binge/purge oscillations of the Laurentide Ice Sheet. *Paleoceanography*, 9(4), 503–511.
<https://doi.org/10.1029/94PA01008>
- Andrews, J. T. (2000). Icebergs and iceberg rafted detritus (IRD) in the North Atlantic: facts and assumptions. *Oceanography*, 13(3), 100–108.
- Bloemendal, J., & deMenocal, P. (1989). Evidence for a change in the periodicity of tropical climate cycles at 2.4 Myr from whole-core magnetic susceptibility measurements. *Nature*, 342(6252), 897–900. <https://doi.org/10.1038/342897a0>
- Broecker, W., Bond, G., Klas, M., Clark, E., & McManus, J. (1992). Origin of the northern Atlantic's Heinrich events. *Climate Dynamics*, 6(3), 265–273.
<https://doi.org/10.1007/BF00193540>

- Broecker, W. S. (1994). Massive iceberg discharges as triggers for global climate change. *Nature*, 372(6505), 421–424. <https://doi.org/10.1038/372421a0>
- Grousset, F. E., Labeyrie, L., Sinko, J. A., Cremer, M., Bond, G., Duprat, J., et al. (1993). Patterns of Ice-Rafted Detritus in the Glacial North Atlantic (40–55°N). *Paleoceanography*, 8(2), 175–192. <https://doi.org/10.1029/92PA02923>
- Heinrich, H. (1988). Origin and Consequences of Cyclic Ice Rafting in the Northeast Atlantic Ocean During the Past 130,000 Years. *Quaternary Research*, 29(2), 142–152. [https://doi.org/10.1016/0033-5894\(88\)90057-9](https://doi.org/10.1016/0033-5894(88)90057-9)
- Hemming, S. R. (2004). Heinrich events: Massive late Pleistocene detritus layers of the North Atlantic and their global climate imprint. *Reviews of Geophysics*, 42(1), 2003RG000128. <https://doi.org/10.1029/2003RG000128>
- Hodell, D. A., Nicholl, J. A., Bontognali, T. R. R., Danino, S., Dorador, J., Dowdeswell, J. A., et al. (2017). Anatomy of Heinrich Layer 1 and its role in the last deglaciation: HEINRICH EVENT 1. *Paleoceanography*, 32(3), 284–303. <https://doi.org/10.1002/2016PA003028>
- Kent, D. V. (1982). Apparent correlation of palaeomagnetic intensity and climatic records in deep-sea sediments, 299(2883), 538–539. <https://doi.org/10.7916/D8CG00NS>
- Mulitza, S., Bergmann, F., Brück, L., Chiessi, C. M., Govin, A., Klann, M., et al. (2015). Cruise No. MSM39 - June 07-June 25, 2014 - St. John's (Canada) - St. John's (Canada) (Version 1.0) [Application/pdf]. MARIA S. MERIAN-Berichte (p. 89 pages). DFG-Senatskommission für Ozeanographie. https://doi.org/10.2312/CR_MSM39
- Nowaczyk, N. R. (2002). Logging of Magnetic Susceptibility. In W. M. Last & J. P. Smol (Eds.), *Tracking Environmental Change Using Lake Sediments* (Vol. 1, pp. 155–170). Dordrecht: Kluwer Academic Publishers. https://doi.org/10.1007/0-306-47669-X_8
- Piper, D. J. W., & DeWolfe, M. (2003). Petrographic evidence from the eastern Canadian margin of shelf-crossing glaciations. *Quaternary International*, 99–100, 99–113. [https://doi.org/10.1016/S1040-6182\(02\)00115-5](https://doi.org/10.1016/S1040-6182(02)00115-5)
- Robinson, S. G. (1986). The late Pleistocene palaeoclimatic record of North Atlantic deep-sea sediments revealed by mineral-magnetic measurements. *Physics of the Earth and Planetary Interiors*, 42(1), 22–47. [https://doi.org/10.1016/S0031-9201\(86\)80006-1](https://doi.org/10.1016/S0031-9201(86)80006-1)
- Robinson, S. G. (1993). Lithostratigraphic applications for magnetic susceptibility logging of deep-sea sediment cores: examples from ODP Leg 115. *Geological Society, London, Special Publications*, 70(1), 65–98. <https://doi.org/10.1144/GSL.SP.1993.070.01.06>
- Robinson, S. G., Maslin, M. A., & McCave, I. N. (1995). Magnetic susceptibility variations in Upper Pleistocene deep-sea sediments of the NE Atlantic: Implications for ice rafting and paleocirculation at the Last Glacial Maximum. *Paleoceanography*, 10(2), 221–250. <https://doi.org/10.1029/94PA02683>
- Small, D., Parrish, R. R., Austin, W. E. N., Cawood, P. A., & Rinterknecht, V. (2013). Provenance of North Atlantic ice-rafted debris during the last deglaciation—A new application of U-Pb rutile and zircon geochronology. *Geology*, 41(2), 155–158. <https://doi.org/10.1130/G33594.1>
- Zolitschka, B., Mingram, J., Van Der Gaast, S., Jansen, J. H. F., & Naumann, R. (2002). Sediment Logging Techniques. In W. M. Last & J. P. Smol (Eds.), *Tracking Environmental Change Using Lake Sediments* (Vol. 1, pp. 137–153). Dordrecht: Springer Netherlands. https://doi.org/10.1007/0-306-47669-X_7

Chapter 5: Synthesis and Outlook

Primary aims of this PhD thesis were to provide a fundamental petrological and rock magnetic understanding of ice-rafted detritus in the Northwest Atlantic, whose distribution in sediment records is used as paleoclimatological archive of the dynamics of the calving and episodic collapse of the North American ice-sheet complex. Some principal questions, which could be largely resolved by this thesis, addressed the lithological control of magnetic susceptibility records of Heinrich Event layers, the concurrence of ice-rafting and other modes of glaciomarine sediment transport, and the influence of stochastic IRD particle distribution in the sediment column. Sedimentological, petrological, petrographical, geochemical, and magnetic properties of a Late Pleistocene glaciomarine sediment core acquired at the foot of the southeastern Grand Banks Slope, Newfoundland, were stratigraphically and statistically compared. The aims mentioned above were achieved in steps where the thesis chapters are interlinked: Chapter 3 was developed upon the knowledge gained from Chapter 2, and Chapter 4 sheds light on (and sets limits to) the stratigraphic expression of magnetic records shown in both previous chapters.

The initial focus of the investigation was to elucidate the collapse chronology of the Laurentide ice sheet during MIS 2 and MIS 3 based on available geological imprint of coarse-grained IRD fractions (>1 mm) that were entrained in the calved icebergs and deposited within the ocean basin as detailed in Chapter 2. All IRD particles sized > 1 mm were petrologically identified under binoculars and divided into 22 micro-optically discernable lithologies. Their abundances were determined at a high resolution of 2 cm steps throughout the continuous stratigraphic sequence of HLs (H1 – H6). This study revealed that ooid-bearing dolomitic IRD dominated the mid-part of all HLs. In contrast, while muscovite-biotite granite was found in higher abundance at the top and bottom of the event layers. Furthermore, the statistical analysis of the count records of 22 IRD lithologies identified three well-defined IRD groups based on whether their deposition was higher or lower during Heinrich Events than during interim periods, or similar in both. Compositionally, the HLs H1, H2, H4, and H5 were found to be kindred while H3 and H6 were both distinct.

Microscopically classifiable coarse-grained IRD particles represent just a minute fraction in relation to the silt to fine sand IRD sizes that constitute the larger portion of the total IRD. These are virtually undiscernible and inseparable from the background sediment and hence neither quantifiable nor petrographically recognizable and petrologically classifiable. In order to determine, classify and evaluate the magnetic influences of the petrologically classified IRD, use was made of the coarse-grained IRD fractions. Interestingly, the magnetic susceptibility of HLs is usually enhanced due to response to higher IRD composition in contrast to interlayer units that have somewhat lesser IRD. However, it is intriguing to note that out of the 22 IRD >1 mm lithologies, as many as 16 have relatively lower magnetic susceptibilities than the background while only 6 are higher out of which the muscovite-biotite granite is four-fold higher than the background. The muscovite-biotite granite which is second only to the weakly magnetic dolomite in dominance is characterized by multi-domain coarse magnetite and counterbalances the magnetic dilution posed by the mostly diamagnetic IRD fractions (i.e. carbonate IRD and quartz minerals). This is showcased by XRF data where the magnetic enhancement linked to the K/Fe element ratio was just partly compensated by the Ca/Sr

record. In modeling the magnetic susceptibility of the glaciomarine sediment based on the scarce IRD count, the misfit of the model suggests that IRD sedimentation does not only occur through detritus rain-out from icebergs but rather through other transport processes like advection or gravitational flow, at least for the later part of the transport route.

Magnetic susceptibility records obviously depend on the investigated sediment core material, but are also greatly influenced by the sensor type and characteristics of the susceptometer. This is evidenced by comparison of the records produced for an individual core by different logging techniques, i.e. whole-core measurements with coil sensor, split-core measurements with spot sensor, and discrete sample measurements with bulk sensor. Conventionally, susceptibility logging is carried out in an uniaxial format where the heterogeneity of the sediment is either underrepresented or exaggerated. The underrepresentation is due to the sensor characteristic that averages signals over a large volume, integrating the microscale susceptibility distribution over a large core volume. For split-core measurements spot, sensors are placed in direct contact with the sediment surface thereby generating signals of high resolution. Due to the randomness of IRD distribution in the sediment column and core, this high-resolution signal is in parts stochastic and therefore not interpretable in every detail. The stochasticity of IRD particle distribution is even more critical for susceptibility records of sieved IRD fractions, which, due to the low number of IRD particles and their wide lithological and size diversity, appear very noisy and share no pattern similarity with all forms of bulk sample measurements. To delineate and average the randomized lateral distribution of IRD in glaciomarine sediment, a novel technique of spot sensor logging was adopted where the split core was scanned by multi-tract logging to obtain a statistical representation of the IRD. The obtained areal data was transposed to create a contour plot showing the distribution of the IRD as well as to statistical uncertainty diagnostics such as value range and standard deviation.

In closing, the research questions presented in each subproject are briefly stated below:

1. How can the micro-optically highly varied IRD particles be petrologically classified? Does the deposition of different IRD lithologies adapt to a systematic fashion or trend in the HLs? Which of the IRD lithologies show preferred deposition in HLs or ILs?

The IRD lithologies were petrologically and petrographically identified and classified into 22 newly defined optically distinct lithologies using the most appealing coarse IRD fragments. The deposition of ooid-bearing dolomite IRD mainly occurs at the mid-part of the HLs whereas the muscovite-biotite granite predominates at the bottom and top of the HLs. Some IRD lithologies show preference in deposition within Heinrich Layers or within interlayers. The initial group shows higher deposition in HLs while the second group has increased occurrence in the interlayer and the last group is equally occurring in both HLs and interlayers.

2. What are the magnetic properties of each IRD lithology? How do these differ and possibly allow distinction? Which IRD lithologies have decisive influence on the magnetic susceptibility of HLs? How well can the overall magnetic susceptibility of HLs be explained and modeled from bulk sediment properties or IRD counts?

The magnetic properties of the 22 identified IRD lithologies revealed that 16 out of the 22 distinct lithologies are characterized by lower magnetic susceptibility than the background sediment, while only 6 lithologies have higher susceptibilities, in case of muscovite-biotite

granite even four-fold higher than background. Due to its high abundance, muscovite-biotite granite has the highest influence on the magnetic susceptibility of HLs. Our IRD models suggest that HL sedimentation does not only occur by detritus rain-out from icebergs but likewise through other transport processes like suspension and gravitational flow.

3. How does randomness govern the stratigraphic distribution of IRD in sediments and how does this randomization affect the different types of magnetic susceptibility records? Are there technical ways to quantify stochastic lateral sediment inhomogeneity?

The distribution of IRD is generally random due to varying iceberg transport pathways and differences in iceberg sediment load and grain size distribution. The randomness of IRD in a glaciomarine sediment makes the magnetic susceptibility signal spikier, in particular in IRD-rich sections, where the signal randomly fluctuates at high frequency and amplitude change. The inhomogeneity of sediment can be visualized and quantified by scanning across a split core surface using a susceptibility spot sensor on multiple tracts.

This PhD research involved a large body of microscopic work where IRD particles of varied grain sizes were investigated at very high resolution. Though, the study focused on just a single core (GeoB 18530-1) that stratigraphically extends from MIS 3 to Holocene, studying more cores in the same vein from different locations within the Ruddiman Belt would add more credence to this undertaking. Preferably, the acquisition of such cores should be spread across both distal and proximal regions and perhaps, at all four north, south, east and west cardinals of the IRD rich belt. This would provide a broader picture of all the IRD lithologies that have been deposited during the glacial activities of the Laurentide Ice Sheet. As the cornerstone of IRD lithology has been set, the next step would be to narrow down to a particular perhaps smaller study area to conduct provenance study. This has been one of the goal that was envisage at the early stage of this project however, due to time constraint this could not be realized. The inclination was to travel to Canada and obtain rock samples from existing rock collections or from outcrops in accessible regions with the aid of ArcTrain Canadian partners. The acquired samples would then be analyzed petrologically and petrographically as well as geochemically. Additionally, acquiring the radioactive ages of both outcrop and IRD particles would be of great significance to infer the provenance of individual IRD particles. Such robust investigation can help in understanding the locations of ice sheet margins and bolstering the delineation of Laurentide Ice Sheet dynamics and extent.

As the explored IRD are largely granule sizes that underrepresent the greater portion of total of IRD in a core, it would also be momentous to conduct a high resolution (2 cm steps) sieve analysis of the studied core GeoB 18530-1 to expound further on which grain size fractions majorly contribute to the enhanced magnetic susceptibility signals in HLs throughout the stratigraphic column.

Acknowledgements

The pursuit of a PhD project is an interesting endeavor filled with joy, anxiety, daunting feelings, and scientific search for the unknown. This journey would not have been successful without the support and advice from my supervisor, colleagues, friends, family and loved ones.

Foremost, I would like to express my sincere appreciation and gratitude to my supervisor, Prof. Dr. Tilo von Dobeneck, who believed in me and gave me the opportunity to work with him at Marine Geophysics group of University of Bremen, Germany. He continuously supported me throughout this undertaking by incessantly motivating, advising, teaching, and guiding. When I first landed in Bremen, he picked me up at the airport and accepted me to stay in his family house just like a father would do to his son. I lived in his house for a period of over two months and his wife Maliya Gu always cooks delicious Chinese meals for us. Also, I have on many occasions spent weekends at his house working on manuscripts and his wife repeatedly keeps providing lunch or dinner all the time.

I would like to extend my unfeigned gratitude to Marine Geophysics group that is full with wonderful and sweet people that are always ready to assist in whatever way they can, I genuinely appreciate you all. Many thanks to Dr. Thomas Frederichs, Dr. Yang Zhang, Dr. Jana Just, Adrian Höfken, Wanzhang Wang, Martina Braun, Liane Brück, Christian Hilgenfeldt and Heike Piero who supported me in virtually solving all kinds of issues related to laboratory, IT/computer, administration etc. I would like to also express my appreciation Dr. Edoardo Dallanave who has been a wonderful office mate and a person that I usually throw random question at whenever I get stuck in rock magnetic related stuffs.

I also acknowledge the opportunity given to me by Prof. Dr. Michal Kucera to be part of the International Research Training Group (ArcTrain) which gave me the opportunity to go on Cruise and travel for annual meetings. My special thanks goes to Dr. Frank Lisker, who advised and provided me with a good petrographic microscope to carry out analyses effortlessly. Also, I would like to thank Dr. Guillaume St-Onge, Dr. Stefan Mülitz and David Piper for revising the first manuscript. Many thanks to Anne Hübner for preparing the thin sections slide for the ice-rafted detritus.

Notwithstanding, I would like acknowledge and thank and the management of Petroleum Technology Development Fund, Nigeria (PTDF) for awarding me a four years scholarship to pursue my PhD, I am very grateful.

Lastly, though my parent Alhaji Abubakar Jatobe and Hajiya Zara Ibrahim are late but, I cannot end without mentioning them and expressing my gratitude, love and appreciation for raising me right and instilling in me good morals and in believing in myself. I will be forever grateful and I miss you both and continue to resting in peace. Amen.